UNIVERSITÀ DEGLI STUDI DI PADOVA

SCUOLA DI SCIENZE

Dipartimento di Geoscienze

Direttore Prof. Nicola Surian

TESI DI LAUREA MAGISTRALE IN GEOLOGIA E GEOLOGIA TECNICA

Mineralogical, geochemical and microstructural characterization of fault rocks from the Koyna deep drilling project (India)

Relatore: Prof. Giulio Di Toro

Laureando: Alessio Chiesurin

ANNO ACCADEMICO 2021/2022

Preface

There are many articles that discuss the human-induced seismicity of Koyna-Warna area (300 km south of Bombay, India), the role of reservoir water level and pore pressure, the structural geology of the area, etc., but few of them focused on the mineralogy and microstructure of the basement fault rocks possibly responsible for the seismicity. The main reason is that there were no deep wells capable of extracting samples directly from the Indian craton. In fact, the seismogenic volume where hypocenters are located in the Proterozoic (2.7 Ga) Indian crystalline basement is buried beneath a 1-2 km thick basaltic layer of the Deccan Traps (68-60 Ma). Because of this, to gain information on the seismicity of the area and to collect samples from the seismogenic volume, the largest International Continental (scientific) Drilling Project was carried on in 2011-2014.

Thanks to a collaboration with Prof. Sukanta Roy, Head of the Borehole Geophysics Research Laboratory in Karad (Maharashtra, India), and after a visit by Professor Giulio Di Toro and Dr. Elena Spagnuolo (Istituto Nazionale di Geofisica e Vulcanologia, Rome, Italy) to the Karad ICDP rock repository in Karad 2019, 17 fault and vein rock samples from the International Continental Drilling Project (ICDP) were brought in Italy. The samples were selected because they represented the last deformation events recorded in the studied boreholes. The aim of my Master's thesis was to study these samples for the first time from a mineralogical, geochemical and microstructural point of view, using X-ray powder diffraction (XRPD) and the field emission gun scanning electron microscope (FEG-SEM) recently installed at the Department of Geosciences. In particular, my contribution was to recognise the mineralogical phases that fill the fault/fractures, determine the deformation mechanisms that affected these samples and reconstruct the sequence of deformation events. This should allow me to understand whether these last deformation events are actually related to the human-induced seismicity observed in the area. The results of this thesis will be used for future experimental and theoretical studies on human-induced fault reactivation.

Contents

Abstract

This master's thesis describes the mineralogical and microstructural characteristics of fault rock samples taken from deep perforation boreholes in the Koyna area, India (https://www.icdp-online.org/projects/world/asia/koyna-india/). This area is of exceptional significance from the point of view of human-induced seismic activity. In fact, in 1967, in this area with very low natural seismicity, following the construction of a reservoir in the early 1960s, the most violent human-induced earthquake was recorded in India (magnitude - M_L= 6.3, 200 casualties).

Geologically, the area is characterized by 2 km thick basaltic lava flows belonging to the Deccan Traps, a magmatic province formed 68-60 Ma and covering the underlying Archean granitic basement (2.7 Ga). The basement hosts fractures and faults reactivated by anthropogenic activities. The drilling project includes 9 boreholes reaching a maximum depth of 1500 m and is aimed not only at the installation of seismometers and other instruments for measuring deformation, temperature, etc., but also at sampling the basement fault rocks.

In my thesis, I studied 17 fault rock samples from three of the nine boreholes. The selected samples include sub-vertical faults/fractures and veins. Mineralogical analysis carried out using the X-ray powder diffraction (XRPD) technique showed a considerable abundance of chlorite, which is present in different types according to chemical composition and formation temperature (129°C < T< 252°C), which was estimated using the Bourdelle & Chatelineau (2015) chlorite geothermometer. Microstructural study using optical microscope (OM) and ultra-high resolution electron microscope (FEG-SEM) allowed reconstructing the sequence of deformation events. The deformation structures include mylonites, breccias and cataclasites with a chlorite, epidote and calcite matrix and associated veins. Faults/fractures bearing veins associated with calcite precipitation are the last deformation event as they cut through all other structures in the area. The chlorite formation temperatures (129°C< T<252°C) are consistent with the temperatures estimated at the hypocentral depths of the Koyna-Warna area, as well as the location of the calcite/chlorite fault/fractures containing them are sub-parallel to the seismogenic structures evidenced by the location of the

hypocentres. From this analysis, I conclude that the faults currently reactivated by human-induced seismicity most likely correspond to those described in this thesis.

Riassunto

In questa tesi magistrale vengono descritte le caratteristiche mineralogiche e microstrutturali di campioni di roccia di faglia prelevati dai pozzi di perforazione profonda dell'area di Koyna, India (https://www.icdp-online.org/projects/world/asia/koyna-india/). Questa area è di eccezionale rilevanza dal punto di vista dell'attività sismica indotta dall'uomo. Infatti, nel 1967, in questa zona con bassissima sismicità naturale, a seguito della realizzazione di un invaso nei primi anni '60 del secolo scorso, venne registrato il più violento terremoto indotto da attività antropiche in India (magnitudo - M_L= 6.3, 200 vittime).

Dal punto di vista geologico la zona è caratterizzata fino a 2 km di profondità da una pila di colate laviche basaltiche appartenenti ai Deccan Traps, una provincia magmatica formatasi 68-60 Ma e che copre il sottostante basamento granitico Archeano (2.7 Ga). Il basamento ospita le fratture e le faglie sub-verticali riattivate dalle attività antropiche. Il progetto di perforazione comprende 9 pozzi che raggiungono una profondità massima di 1500 m, ed è mirato oltre all'installazione di sismometri e altri strumenti per la misura di deformazioni, temperature, ecc., anche al campionamento delle rocce di faglia del basamento.

Nella mia tesi ho studiato 17 campioni di roccia di faglia provenienti da tre dei nove pozzi. I campioni selezionati includono faglie/fratture sub-verticali e vene. L'analisi mineralogica svolta con l'ausilio della tecnica da diffrazione da polveri a raggi X (XRPD) ha mostrato una notevole abbondanza di clorite, che è presente in diverse tipologie in base alla composizione chimica e alla temperatura di formazione (129°C < T< 252°C), stata stimata con il geotermometro per le cloriti di Bourdelle & Chatelineau (2015). Lo studio microstrutturale mediante microscopia ottica (OM) ed elettronica ad altissima risoluzione (FEG-SEM) ha permesso di ricostruire la successione di eventi deformativi. Le strutture deformative includono miloniti, brecce e cataclasiti con una matrice in clorite, epidoto e calcite e vene associate. Le faglie/fratture vene associate alla precipitazione di calcite sono l'ultimo evento deformativo poiché tagliano tutte le altre strutture presenti nell'area. Le temperature di formazione delle cloriti (129°C< T<252°C) sono coerenti con le temperature stimate alle profondità ipocentrali dell'area di Koyna-

Warna, così come la giacitura delle faglie/fratture a calcite/clorite che le contengono sono sub-parallele alle strutture sismogenetiche evidenziate dalla localizzazione degli ipocentri. Da questa analisi concludo che le faglie attualmente riattivate dalla sismicità indotta dall'uomo corrispondono molto probabilmente a quelle descritte in questa tesi.

1. Introduction

1.1 Motivation

Over the past sixty years, various reservoir-induced seismic events (RIS) have been recorded at some 100-120 different sites around the world, and Koyna in Western India is one such site where RIS can be studied with great detail. Koyna is the name of the river that originates in the Western Ghat hills, 225 km southeast of Bombay, near Mahableshwar, Satara district, western Maharashtra, India (Figure 1.1). In this region, most rivers flow from west to east, while the Koyna River has a north-south direction, cutting through the Indian craton. After the Koyna Dam, the river bends to the east like the rest of the watercourses and tributaries. Because of the monsoon rains in western Maharashtra, a series of water reservoirs were constructed after the Second World War, including Koyna and Warna, with the aim of obtaining hydropower, flood control and irrigating fields (Gupta, 2002). The Koyna dam is the second largest hydroelectric project in India and was completed in 1962. Unfortunately, few months after the dam was completed and the reservoir filled, the first seismic sequence started. Then, on 10 December 1967, the largest and most catastrophic human-induced earthquake (magnitude Mw 6.3) was recorded, killing 200 people, injuring 1.500, leaving thousands of homeless and damaging the dam, roads and neighbouring villages (Figures 1.2 a-c). In the following years, there were very intense seismic events with several exceeding Mw 5.

These seismic sequences were related to reservoir operations, including annual water loading and unloading cycles, the rate of increase of the water level in the reservoir, the maximum height and the duration of the high water level (Gupta & Rastogi, 1976; Gupta, 1992; Talwani, 1997a, Talwani, 1997b; Gupta et al, 2015). The water level influenced the frequency and magnitude of earthquakes located near the Koyna reservoir (Gupta et al., 1972a; Gupta et al., 1972b; Gupta, 2002). The seismic activity was intense in the Koyna area from the first filling of the reservoir in 1962, but after the 1967 Mw 6.3 earthquake it migrated 10-25 km further south towards Warna (Rastogi, 1995; Rastogi et al., 2017). Here work began to build a second dam in 1976. The seismic activity affecting the Warna area increased especially after the first impoundment occurred in 1985 (Gupta et al., 2014; Rastogi et al., 2017). Today, the

seismically active area of Koyna-Warna is 30 km x 20 km (Figure 1.1). Because of the societal impact of the reservoir-related earthquakes, and the relatively easy logistic in this rural area of India, the largest and most important drilling project of reservoir-induced seismicity was undertaken.

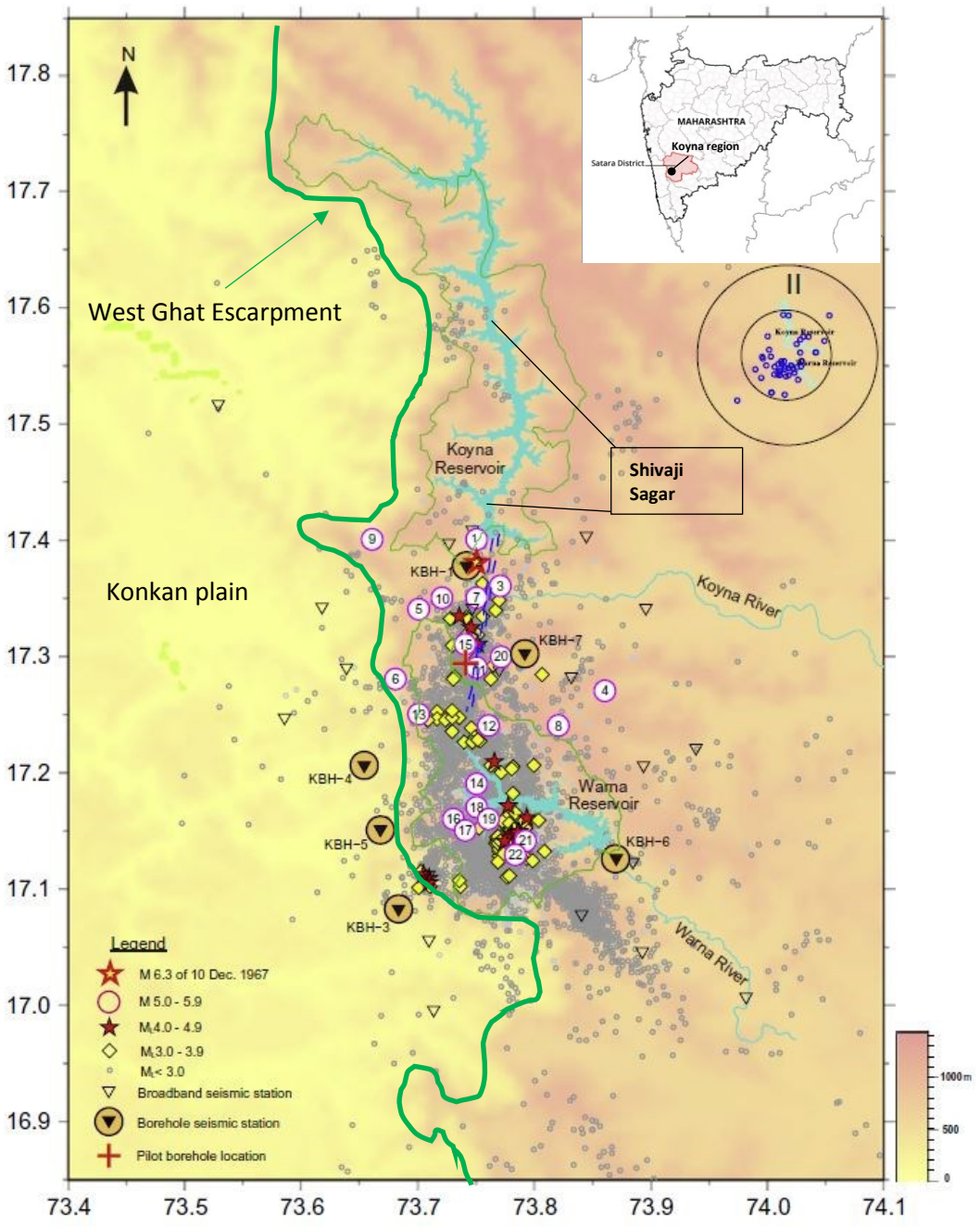

See the caption of **Figure 1.1.** on next page

Figure. 1.1. Map of the Koyna-Warna region showing the locations of the 1967 main shock, M ≥ 5 earthquakes since September 1967 and M < 5 earthquakes during Aug. 2005–Dec. 2015. Numbers inside pink circles show the chronological order of occurrence of the M ≥ 5 events. The networks of seismic stations are also shown. Surface broad-band station is also under operation at the locations of borehole seismic stations. Dashed lines (blue) indicate the Donichawadi fault zone (Gupta et al., 1999). Topographic undulations of the region are plotted which marks the steep differences in the elevations (The elevation scale is in meters). The green curve is the forest boundary. Inset I: Location of Koyna in India. Inset II: shows the distribution of earthquakes of M ≥ 3.7 during 1967–2015 (USGS) in the vicinity of Koyna-Warna region and outer circle of 100 km radius which shows there is almost no seismic activity outside the Koyna-Warna region figure and caption from Gupta et al., 2017a).

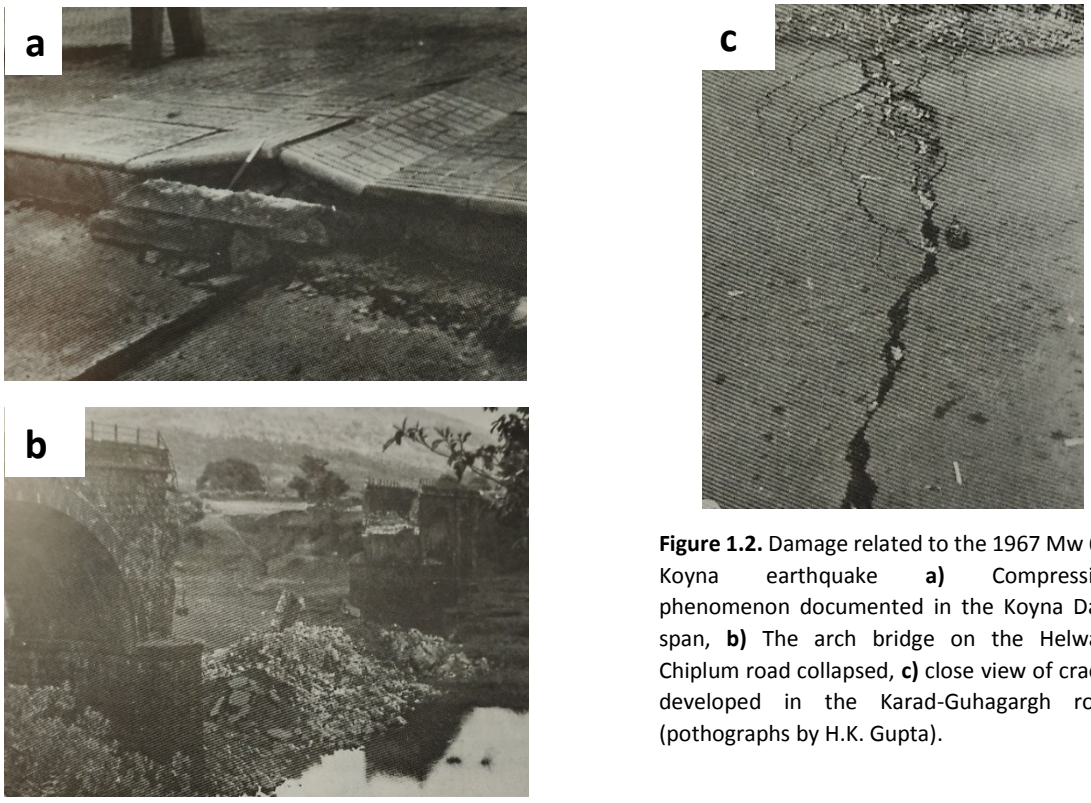

Figure 1.2. Damage related to the 1967 Mw 6.3 Koyna earthquake **a)** Compression phenomenon documented in the Koyna Dam span, **b)** The arch bridge on the Helwak-Chiplum road collapsed, **c)** close view of cracks developed in the Karad-Guhagargh road (pothographs by H.K. Gupta).

It is noteworthy that no major earthquakes were recorded in the Koyna-Warna region for several hundred years. The Konya river lies in an intra-plate environment and therefore seismic activity is not as frequent as in collisional zones further north, where plate boundaries are colliding. Therefore, the closest seismometer was located at a distance of about 115 km from the Koyna Dam and it was the latter, along with others, that recorded seismic events from the 1960s onwards, including the 1967 Mw 6.3 earthquake (Gupta, 1992, 2002). After the increase in seismic activity, a campaign was undertaken to set up new seismometers in the area to follow the seismic sequence; a network of 10 seismic stations was installed from April 1966 to December 1997 (Rai, 1999). Before that, however, due to the micro-earthquakes felt at the time of the first impounding of the reservoir, the first seismic observatory consisting of four stations was

set up by the Maharashtra Engineering Research Institute (MERI) to monitor the Koyna region (Talwani, 1997a). Between 1966 and 1997 the 10 seismic stations made it possible to locate 406 events confined to an area of 11 X 25 km^2, with a hypocentre limit of 10 km depth (Rai, 1999; Gupta, 2002). As mentioned earlier, the quality of the seismological data is rather poor for earthquakes that occurred before 1995 and were therefore relocated by Rajendran et al., (1996) and Talwani (1997a). The former author determined the epicenter of 207 earthquakes of Mw>3 that occurred between 1983 and 1993 and found that the earthquakes affected a larger area between June and December, following the impounding of the reservoir, than between January and May (Figures. 1.3 and 1.4). In addition, a relation between the filling of the reservoir and the seismic events appeared: during the impounding of the reservoir between June and December, corresponding to the monsoon season, earthquakes are larger in number and distributed in large area between the Koyna and Warna reservoirs (Figure 1.3a). Instead, during the lowering of the water level between January and May, earthquakes are smaller in number and localize near the Koyna dam (Gupta, 2002) (Figure 1.3b). Instead, Talwani (1997a) localized the hypocenter of 300 earthquakes of Mw > 3, that occurred between 1963 and 1995, and described the geometry of the seismogenic structures, through geological and geophysical studies, identifying the presence of several seismogenic crustal blocks, underlain by a fluid-filled fracture zone. After these studies, Talwani (1997a) proposed that the seismicity in Koyna area was limited to the west by the Koyna River Fault Zone (KRFZ) which borders the Western Ghat Escarpment (WGE: Rastogi et al., 1995), and to the east by the Patan Fault with a NE-SW direction (Gupta, 2002) (Figure 1.3). Both Talwani (1997a) and Gupta (2002) proposed that the area between the KRFZ and the Patan Fault was intersected by a series of sub-vertical faults/fractures with a NW-SE trend, which could extend from the Earth's surface to the hypocentral depths, providing conduits for fluid flow from the surface to the hypocentral depths (Gupta, 2002) (Figure 1.5). Thus, the presence of subsurface fractures that allowed the percolation of water from the Koyna and Warna reservoirs was already proposed in the 1990s; the fluid migration would influence the state of stress and trigger the seismic swarms in the Koyna area. After many studies, it was discovered that the Koyna region has a unique tectonic structure, characterised by strike-slip and normal faults (Rao & Shashidhar, 2017).

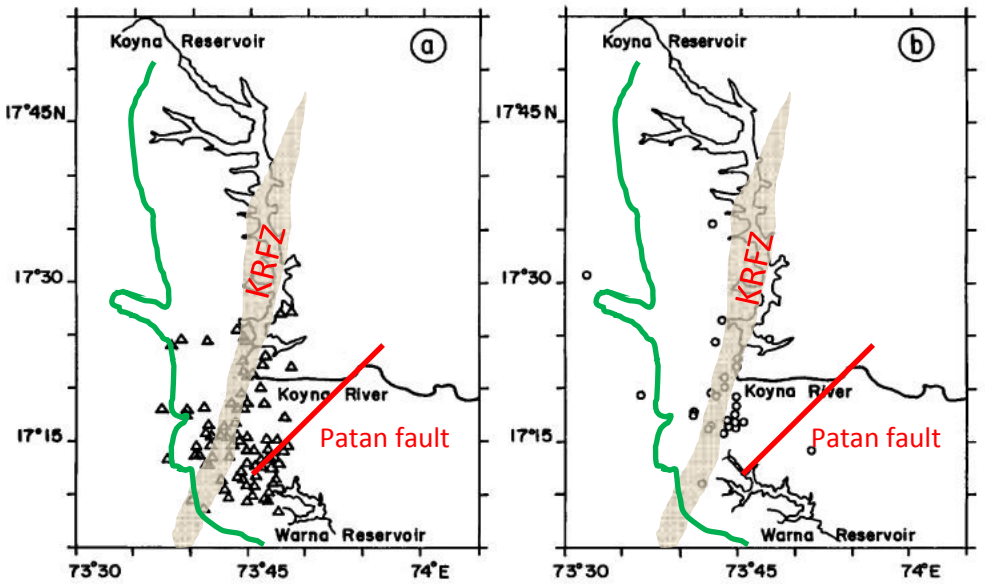

Figure 1.3. The relocated earthquakes for the period 1983-1993 at Koyna. **a)** For the period June through December, and **b)** January through May (figure and caption from Gupta 2002). In green is shown the Western Ghat Escarpment (WGE).

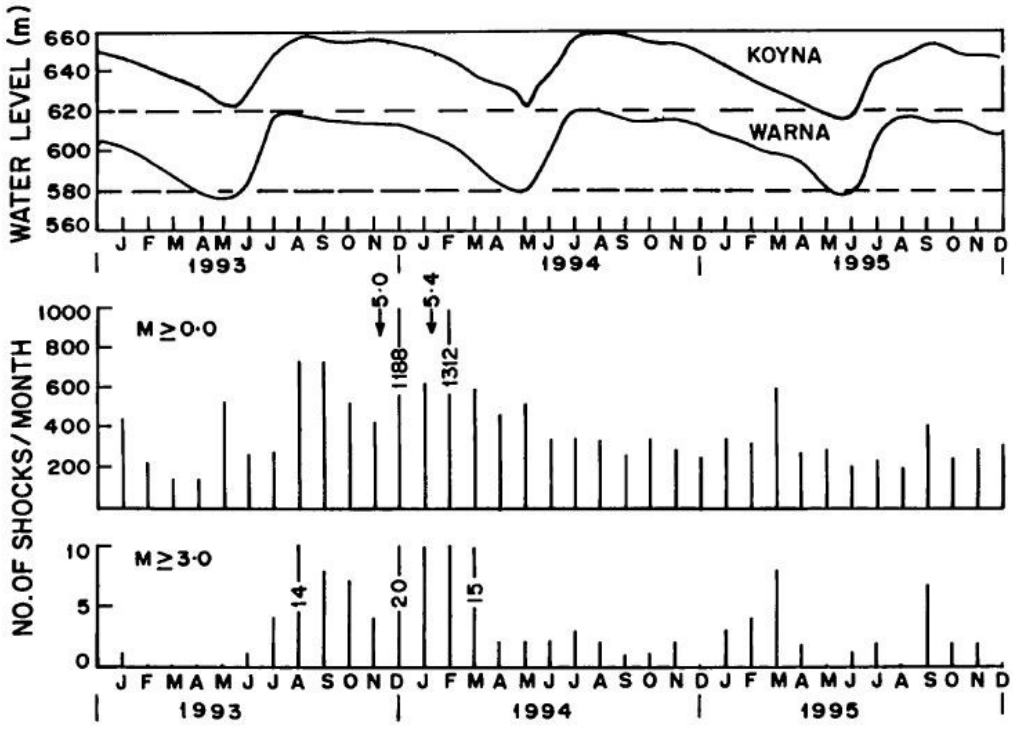

Figure 1.4. Water levels in Koyna and Warna reservoirs and the seismic activity in the Koyna and Warna reservoirs for the period 1993 through 1995. The middle figure shows the monthly frequency of M >0.0 and the bottom one for M >3.0 (figure and caption from Gupta, 2002).

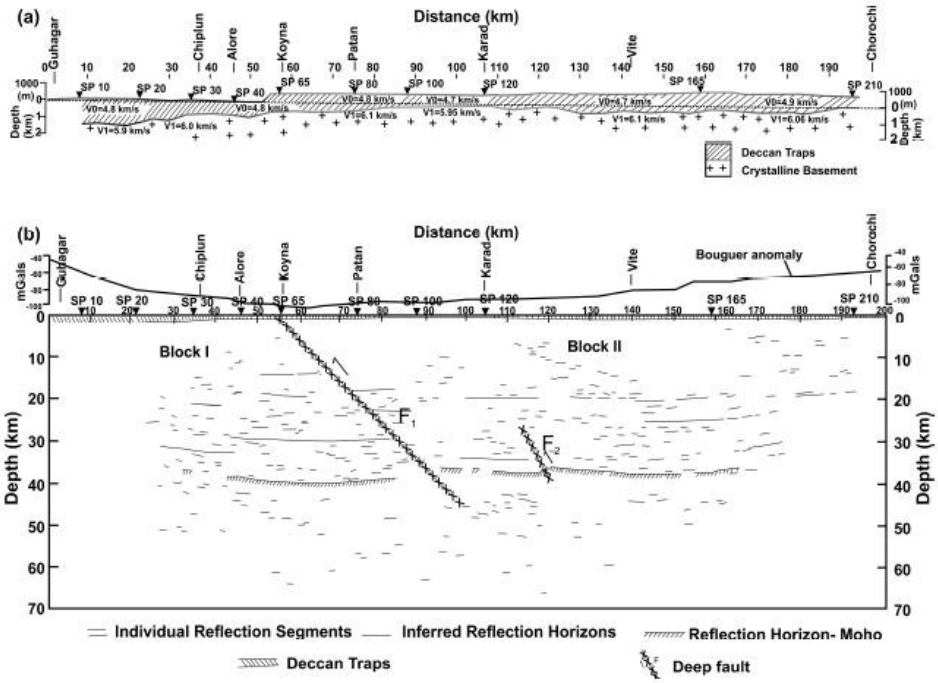

Figure 1.5. Thickness of the Deccan Traps **(a)** and section **(b)** of an E-W profile passing through the Koyna Dam. Sub-vertical faults cutting through the basement down to the lower crust are visible in (b) (Figure from Sakar & Sain, 2017)

After these studies, further research was focused on the relations between fluctuations in the water level of the Koyna and Warna reservoirs and seismic events. This relation, for example, was evident in 1993 when in July the water column exceeded 60 m above the water level in the period just before the monsoon and in August there were a lot of earthquakes larger than Mw 3 (Gupta, 2002). As can be seen in Figure. 1.4, the monsoon period and thus the rise in the water level in the reservoir led to a rapid (August and September) and a delayed (December-February) response of the seismic activity. In general, (Simpson et al., 1988) distinguish two types of reservoir-related human-induced seismicity:

Rapid response: increased seismicity due to rising reservoir water level (the basin is considered almost impermeable in the short time period). Seismic triggering is attributed to increased normal and shear stress in an elastic medium. Snow (1972) argues that the reservoir water level increase produces a static increase in load thus increasing the σ_V. In the Mohr space, for the normal faulting regime, the increased load increases the differential stress leading to fault reactivation (Figure 1.6) (Scholz,

2019). The earthquake magnitude is usually low and seismic activity is confined to the reservoir area.

Delayed response: seismicity occurs after some time from the reservoir impounding phase (the basin in considerer permeable in the long time period). Seismic triggering is attributed to poro-elastic effects associated with fluid diffusion from the reservoir to the hypocentral depths. This results in an increase of the pore fluid pressures which, in the Mohr space, result in the translation of the Mohr circle towards the fault reactivation criteria. Usually the earthquake magnitude is larger than in the *rapid response* and the seismic activity is well-beyond the perimeter of the reservoir, tens of kilometers too.

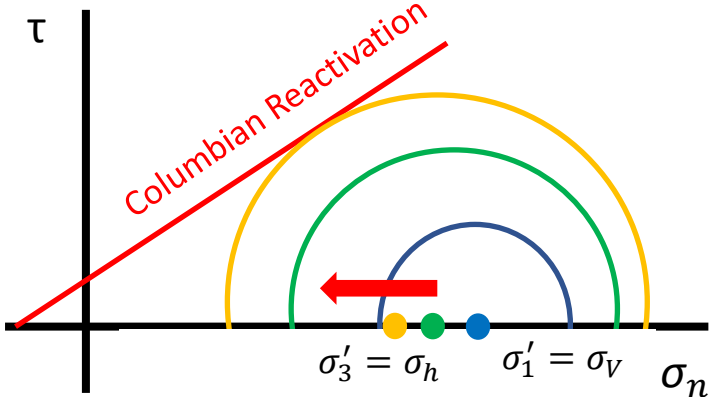

Figure 1.6. State of stress and stress variations induced by reservoir impounding operations (Mohr circle in a normal regime). Rapid response: the σ_V increases because the water level in the reservoir increases, so the differential stress (circle diameter) increases (rapid response). Delayed response: fluid diffuses at depth and the pore pressure also increases, so the circle moves to the left, thus touching the Columbian fault reactivation criteria.

The Koyna-Warna site has both responses in fact: just after the first filling of the reservoir (1962) seismic events occurred (*rapid response*), but the largest earthquake (1967) occurred after four months the maximum peak of reservoir water level (*delayed response*).

In summary, Koyna area is a classic site of human-induced earthquakes:

- Seismically active area located near the reservoirs since 1962;

- The largest human-induced earthquake (Mw 6.3) in 1967;
- Earthquakes are association with the loading and unloading cycles of Koyna and Warna reservoirs;
- Isolated seismic zone, 20 x 30 km^2, with hypocentres at a maximum depth of 13 km.

However, this knowledge was insufficient to reconstruct the model of the triggering of human-induced earthquakes. For instance, the geology of the Koyna area, the physical properties of the rocks and the hydrological parameters were poorly known because of the 1-2 km thick Deccan Traps cover that impedes the investigation of the underlying Archean basement rocks where the hypocenters are located. In 2011 an International Continental Drilling Programme (ICDP) workshop was organized to discuss a proposal to drill deep to the hypocentres of earthquakes, approximately 7-10 km and construct an in-well observatory capable of continuously monitoring a seismic area. This infrastructure would allow scientists to understand the mechanics of human-induced earthquakes, and to contribute to seismic risk assessment and earthquake forecasting (Gupta & Nayak, 2011). The investigation with the nine wells, reaching a maximum depth of 1500 m, started in 2011 (Gupta, 2017b). Then in 2014, in a second workshop, the results of the previous drilling phase were discussed and a suitable location for two very deep (3-5 km) pilot wells proposed (Gupta et al., 2014). In 2017, the construction of the first pilot well (KFD1), located in the epicentral area of the M 6.3 1967 earthquake, began. The current goal is the study of the bedrock and fault rocks from these deep boreholes to go into more detail about the seismicity of the area.

1.2 State of Art

1.2.1 Human-Induced Seismicity

Human-Induced Seismicity is triggered by a range of activities including reservoir impoundment, construction of tall buildings, coastal engineering, quarrying, extraction of groundwater, coal, minerals, gas, oil and geothermal fluids, tunnelling and adding material to the subsurface by allowing flooding of abandoned mines and injection of waste disposal fluids, enhanced oil recovery, hydrofracturing, gas storage and carbon sequestration (Foulger et al., 2018). Wilson, 2017 produced a public database of human-induced earthquakes, HiQuake, containing 700 instances of anthropogenic projects capable of inducing seismic activity (www.inducedaerthquakes.org) (Fig. 1.7a-b). Human-induced earthquakes have been increasing in recent years because of industrial development, but considering the large number of industrial projects, they remain rare (Table 1.1). Most induced earthquakes occur in intra-plate areas. This is the case because, first, the plate boundaries are mostly in the oceans and therefore cannot be affected by human activity and, second, because in intra-plate areas the rocks are close to failure and therefore little stress variations may trigger an earthquake (Zoback & Healy, 1984; Townend & Zoback, 2000; Brudy, et al., 1997). Moreover, in active seismic areas (e.g., instrumental and historical seismicity) or along plate boundaries is not trivial to distinguish between natural and human-induced earthquakes. Many natural processes contribute to the accumulation of stress on faults such as: tectonic deformation, volcanism, natural heat loss, isostatic uplift following deglaciation or oceanic discharge, land tides, intraplate deformation resulting from distant plate boundary events, large remote earthquakes, erosion, dissolution, natural groundwater migration and weathering. Added to these are industrial activities that may cause induced-earthquakes (Foulger et al., 2018). Anthropogenic stress variations capable to induce earthquakes range from a fraction of MPa (less than 1 atmosphere or about 1 m of rock cover, e.g., Keranen et al., 2014), to several tens of MPa. Human activity can therefore modify natural seismicity, slowing down/reducing it as in the case of oil and water extraction in Val d'Agri (Italy), or accelerating/increasing it as in the case of the construction of the Koyna dam, India.

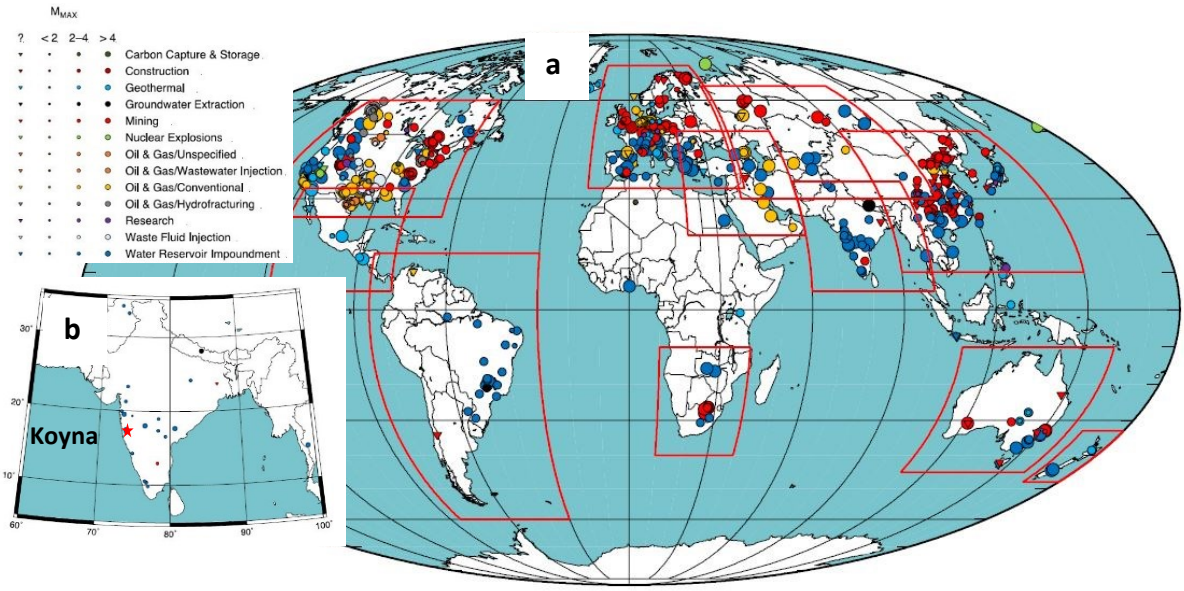

Figure. 1.7a. Cases of human-induced seismicity world-wide, in Mollweide projection, centered on the Greenwich meridian. Colors of symbols indicate different categories of seismogenic activity. Circle sizes indicate the magnitudes of the largest reported induced earthquakes in each category, and inverted triangles indicate cases for which this magnitude was not reported. Red boxes show the locations of the regional maps. **b)** It is a zoom of India nation and its RIS (figure and caption from Foulger, 2018).

Table 1.1 Foulger, 2018

Induced seismicity statistics for the total numbers of projects of different types, the number that are seismogenic, and related data.

Project type	# projects	# cases in the database	% projects that are seismogenic	Observed maximum magnitude (M_{MAX})	# seismogenic projects reported by Hitzman (2013)	Source for # projects
CCS	75	2	2.67	1.7	–	Huaman and Jun (2014)
Construction	Unknown	2	–	4.2	–	
Conventional oil and gas	67,000 fields	116	0.17	7.3	65	Li (2011)
Fracking	2,500,000 wells	21	0.00	4.4	2	King (2012)
Geothermal	Unknown	56	–	6.6	26	Bertani (2010)
Groundwater extraction	Unknown	5	–	7.8	–	
Mining	13,262 currently active mines	267	2.01	6.1	8 ("other")	http://mrdata.usgs.gov/
Nuclear (Underground)	1352 tests	22	1.63	4.9	–	Pavlovski (1998)
Research	Unknown	13	–	3.1	–	
Waste fluid injection wells (Class II wells)	151,000 wells (USA only)	33	0.02	5.7	11	Hitzman (2013)
Water dam	6862 reservoirs (> 0.1 km^3)	168	2.45	7.9	44	Lehner et al. (2011)
Total		705			156	

The Koyna case is an example of *reservoir-induced seismicity* (RIS), although the more appropriate term would be *reservoir-triggered seismicity* (RTS) because tectonic loading plays a primary role (McGarr & Simpson, 1997) as follows:

- RIS: Causal activity is responsible for most of the stress variations or most of the energy required to produce earthquakes;

- RTS: causal activity is responsible for a small fraction of the stress variations or energy associated with earthquakes, as tectonic loading plays a primary role.

For many years now, man has been building dams to create artificial reservoirs used for hydroelectric power collection, irrigation of fields, collection of waste water (oil and gas industry, quarrying activities). Earthquakes occurring near reservoirs, as a result of damming, would fall into the category of 'triggered seismicity', since the stress level changes associated with filling some of the deeper reservoirs are of the order of 1 MPa or so, while the stress drops associated with earthquakes are much larger (Gupta, 2002). In practice, RIS cases associated with dams should be referred to as RTS because it is not the anthropogenic stress (stress due to the dam/reservoir) that triggers the earthquake, but it speeds up or anticipates the occurrence of the seismic event (Foulger, 2018). From now on I will use the term triggered seismicity (RTS) with regard to the Koyna site.

There are as many as 168 cases of RTS in the HiQuake database, which have certain characteristics in common and that discriminate them from natural earthquake sequences (Gupta, 1992, though the RTS concept was introduced by McGarr & Simpson, 1997):

1. The frequency distribution of earthquakes over an observed magnitude range in a particular area can be represented by a simple relationship of the type (Gutenberg-Richter relation):

$$\log_{10} N = A - b\,M$$

here N is the number of shocks with magnitude greater than M, A is a constant that depends on the period of observation, the size of the region considered and the level of seismic activity, and b (or b-value) is the slope in the log N –M diagram and describes the earthquake distribution (a power law). The b-value is calculated empirically and ranges between 0.5 and 1.5. Mogi (1963) studied the b parameter in the laboratory with examples of rigidly fractured rocks and discovered that it depends on the mechanical heterogeneity of the rocks, which increases as their

heterogeneity increases (RIS are affected by greater heterogeneity and, as they are often superficial, depend on the mechanical structure of the Earth's crust). A fact that should not be underestimated is the link between heterogeneity and pore pressure because an increase in the latter leads to the first seismic events occurring in a highly heterogeneous environment. Gupta (1992; 2002) found that in an earthquake sequence in Koyna area, the b-value of the foreshocks was slightly higher than the one of the aftershocks and that both were higher than the regional b-value a 'natural earthquake' sequence.

2. The distribution of aftershocks can be given through the power law (i.e., Omori' law):

$$n(t) = C\, t^{-h}$$

where n(t) is the frequency of the aftershocks per unit time, C and h are constants, of which h indicates the rate of decay of the aftershock frequency and can be used to infer the physical and stress state of the aftershock area, and t is the elapsed time after the main shocks. The h value is usually lower for RIS and therefore the decay of aftershocks is slower than for 'natural earthquakes'.

3. Bath's law is an empirical observation, which is interpreted as a probabilistic consequence of two other laws: Omori's law and the Gutenberg Richter relationship (Schultz et al., 2022). The empirical formula is:

$$M_0 - M_1 = 1.2$$

where M_0 is the magnitude of the main shock and M_1 is the magnitude of the largest aftershock. This formula can also be used for RIS. Large values of b correspond to large terms of (M_0-M_1) and M_1 /M_0. So, for RIS the magnitude ratio of the largest aftershock to the main shock is high (Gupta, 2002).

4. Mogi, (1963) classified the foreshock-aftershock model into three different types based on the structural state of the materials and the spatial distribution of the applied stress (Figure 1.8).

    - Type I: homogeneous material and uniformly applied stress, the main shock occurs without foreshock and is followed by numerous elastic aftershocks.
    - Type II: rather heterogeneous material structure and/or non-uniformly applied stress, small elastic shocks precede the main shock and many aftershocks follow.
    - Type III: very heterogeneous material structure and/or concentrated applied stress; large number of shocks with a gradual increase in magnitude followed by a decrease.

    Typical of the Koyna-Warna area and all other RIS centres is the type II pattern, while in a 'natural earthquake' sequence it is the type I pattern.

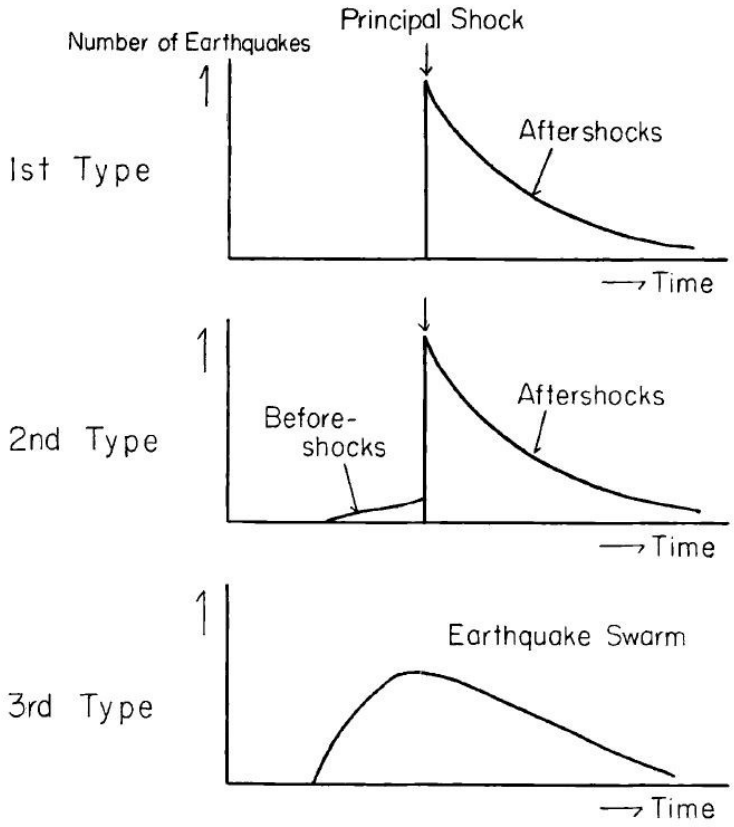

Figure 1.8. The typical patterns of the successive occurrences of the general earthquakes (Mogi, 1963).

The above factors are governed by the mechanical properties and their departure from natural seismic sequences indicates a change in these properties. For Koyna, the b-value is 0.81 for the shallowest events and 0.74 for the deepest (maximum 10 km) and these are very (Gupta, 2002).

Koyna is undoubtedly one of the most interesting areas in the world to gain information on the nature of triggered seismic events. Thanks to the construction of the deep wells, it has been possible to study the mechanical properties of the bedrock. Hopefully, the results of this large deep-drilling project may address most of the questions raised during the 2011 and 2017 workshops, including (Gupta et al., 2011; Gupta et al., 2014; Gupta et al., 2017a):

1. What is the pressure and permeability of fluids in and around the fault zone?
2. What are the composition and origin of the fluids and gases in the fault zone?

3. How do the orientation and magnitude of stresses vary in fault zones?
4. How are earthquakes triggered?
5. How do ruptures propagate during earthquakes?
6. How do seismic source parameters scale with magnitude and depth?
7. What is the role of reservoirs in earthquake triggering?
8. What is the 3-D/4-D nature of the fault zone?

1.2.2 Examples *of reservoir-triggered seismicity (RTS)*

As mentioned earlier, the HiQuake database recorded 168 cases of RTS including examples of RTS taken from Gupta 'Reservoir-Induced Earthquakes', (1992). Here we describe few cases selected because I wish to highlight the complexity and diversity of RTS, even when they occur in a fairly similar geological setting (Bhatsa Dam vs Koyna Dam):

1. *Oroville Dam (Mw 5.7 earthquake, 1975, USA)*

   In the Sierra Nevada foothills southeast of Oroville, California (USA), the largest induced earthquake in US history of magnitude Mw 5.7 occurred on 1 August 1975; the cause was the filling of the reservoir following the construction of the Oroville Dam. The main earthquake was preceded and followed by foreshocks and aftershocks respectively. The dam project was completed in November '67 and the water storage phase began immediately afterwards. Seismic events occurred in the Sierra Nevada foothills, which host a N-S fault system up to 320 km long. Unlike Koyna, the Northern California region has always been seismically active, but with occasional weak earthquakes. Between 1940 and 1974, some 40 earthquakes with a magnitude greater than Mw 3.5 were recorded, but none of these were located within a 40 km radius of the dam. During the 1975 event, 51 earthquakes with a magnitude greater than Mw 3 were recorded between 28 June and 16 August: two foreshocks even exceeded magnitude Mw 4 at a depth of about 8 km, while a dozen aftershocks exceeded this limit, including one with a magnitude of 5.2.

   The Oroville earthquake is associated with a pre-existing normal fault, dipping 60° to the west, with a small component of left lateral motion and a south-north direction. Seismic activity was most conspicuous in '75-'76 when the lake's water level fluctuation increased; in fact, the most intense seismic events on 1 August 1975 followed the largest seasonal fluctuation in lake level to date. In the years that followed, the increase in seismicity was observed constantly, so that the influence of the water level fluctuation on it

was evident. However, in '77-'78, after a major fluctuation no seismic event followed and therefore the Oroville region cannot be fully indicated as a seismic area dependent on water level variation in the reservoir. The most likely hypothesis is that Oroville is not a true RTS due to insufficient residual stress, which is no longer capable of inducing future earthquakes in response to reservoir water level fluctuations. In addition, Oroville's b-parameter is lower than Koyna's and thus legitimizes the question of whether the California case is an RTS or not (Gupta, 1992, 2002).

2. *Bhatsa Dam (Mw 4.9 earthquake, 1983, India)*

This site is located 200 km north of Koyna. The first earthquakes were recorded in mid-May 1983, while the largest seismic events were on 17 August and 15 September 1983 with magnitudes Mw 4.4 and 4.9 respectively, at a time when the water level in the reservoir was rising. The geology is similar to that of Koyna and therefore there was a fear that what happened in Koyna would also happen here; however, there were no significant events in the following years. The area has large variations in altitude spanning, over a distance of 20 km, from 608 m above sea level in the NW to 80 m to the SE. A series of strike-slip/normal faults with a NW-SE trend were mapped, which form a series of horsts and graben where the reservoir is located.

As previously stated, only on the west coast were earthquakes recorded in the past, while in the Bhatsa area none were recorded. Between the summers of 1982 and 1983, the water level rise to 40 m and to the point of triggering seismic events in May 1983; the most intense, up to Mw 4.9, occurred between August and September and then the seismic activity dropped over time. These earthquakes had a hypocentre between 1 and 3 km, although the two major earthquakes were triggered at a depth of 5 km; in addition, the seismic events of '83 and '84 occurred a few months after the maximum water level. The fact that seismicity did not continue after the two major events explains how the earthquakes that were triggered in this area are a direct effect of the reservoir being recharged

very rapidly; the following decrease of seismicity with time may also be an indication of a residual stress deficit (Gupta, 1992, 2002).

3. *Aswan Dam (Mw 5.6 earthquake, 1981, Egypt)*

The seismicity induced by the dam built to dam the Nile River and form the Nasser reservoir is different from the rest of the world, as the peak of seismic activity (earthquake of 14 November 1981 of magnitude Mw 5.6) was observed 17 years after the reservoir was filled in 1964; furthermore, the focal depth of the events was very deep, about 20 km.

The geology of the area is divided by a crystalline basement composed of igneous and metamorphic rocks of late Precambrian origin, cut by dykes striking north-south and east-west and by shear zones that make the rock volume more permeable. Further west, the Nubian Sandstone formation appears, in contact with the basement through an angular discontinuity; an E-W oriented strike-slip fault system called Kalabsha also prevails in this area. There are no earthquakes within a radius of 200 km in the catalogue for the period between 1920-1981, and the first seismometers were installed at a distance of about 60 and 165 km from the Kalabsha fault and in Aswan respectively. These two stations were not always operative, but between 1980 and 1981, they registered twenty earthquakes of magnitude 2.8 to 3.6 on the Kalabsha fault. The Mw 5.6 earthquake of 14 November 1981 was preceded by two foreshocks on 9 and 11 November of magnitude 4.2 and 4.5, respectively, and followed by an intense aftershock event. Thus, the typical characteristics of a RIS are all there: high b-value, seismic event occurring after a rise in the reservoir water level, intense foreshock phenomenon. The largest in magnitude earthquake occurred 17 years after the reservoir was filled probably because the Nubian sandstone is more porous (30%) and permeable than the bedrock; therefore, it stored water allowing a local rise in the water table and a flooding of large neighbouring areas; the stored water spread and increased pore pressure which contributed to the triggering of earthquakes (Gupta, 1992, 2002).

Clearly, seismic events triggered by water reservoirs activities are different because influenced by local geological setting, fault zone and rock properties, stress distribution and tectonic loading, hydrogeology, etc. As a consequence, the forecasting of RTS is extremely difficult.

2. The reservoir-triggered seismicity of Koyna-Warna area

2.1 Seismicity of the area

In the Koyna-Warna since 1962, when the filling of the Koyna reservoir began, there have been more than 100,000 earthquakes, of which 22 were of Mw > 5 and 200 of Mw > 4.0 (Gupta, 1992; Rastogi, et al., 1997; Gupta, 2002; Rastogi, 2017). These earthquakes occurred over an area of 30 km x 20 km between the Koyna and Warna reservoirs (Talwani, 1997a) (Figure 1.1). The most notable earthquakes are those of Mw > 5 that occurred in the following time intervals: 1967-68, 1973, 1980, 1993-94, 2000 and 2005. Prior to the construction of the reservoir, the area was not seismically active and the only recorded earthquakes were 70-100 km away from the Koyna Dam, along the west coast of India (Gupta, 1992). From 1962 until 1992, the epicenters of earthquakes were confined to an area south of the 20-km-long Koyna Dam, while from 1993 onwards, seismic activity was concentrated further south near the area's second dam, the Warna Dam (Rastogi, 2017). As the region is covered by a thick layer of Deccan basalts, the structural setting of the area was unknown because there were no outcrops; the only evidence of seismic ruptures were cracks and fissures in the ground associated with the Mw 6.3 1967 earthquake (Gupta, 1992).

2.1.1. Faults and stress regime

*T*he Koyna dam project was undertaken to obtain a large reservoir for energy purposes and to reduce flood-related risk. After the reservoir was filled in 1962, seismic activity began and micro-earthquakes were recorded (Gupta et al., 1980). Immediately after the first earthquakes, and especially after the Mw 6.3 earthquake in 1967, several studies were undertaken to find out more about the causes and to learn about the faults related to these seismic events.

The Koyna-Warna region is situated in a plateau with valleys, terraces and ridges, bounded to the west by the Western Ghat escarpment with a N-S direction, which separates it from the Konkan plateau (Chadha et al., 2008) (Figure 1.1), and bounded to the south by the Dharwar region. The Western Ghat escarpment formed as a result of

an intense erosional and extensional rifting phase of the Indian plate (Subrahmanya, 1998; Goswami, 2020).

There are two main fault orientations in the Koyna-Warna region: NNE-SSW and NW-SE (Gupta, 1992; Talwani, 1997a; Rastogi et al., 1997) (Figure 2.1). These faults/fracture (often, lineaments) were recognized thanks to remote sensing (Landsat satellite images, (Durà-Goméz & Talwani, 2009); LiDAR or Light Detection and Ranging images, (Arora, et al., 2017), geomorphological studies (Jadhav & Lalitkumar, 2017), aeromagnetic data (Talwani et al., 1996) and analysis of seismicity data (Talwani et al., 1996; Talwani, 1997a). In particular, the main structures include (Figures 2.1 and 2.2):

1. The N-S and NE-SW striking lineaments, including: the large Donichawadi fault, located mainly in a narrow area about ten kilometers long between the Koyna and Warna reservoirs and parallel to the Western Ghat escarpment (Arora et al., 2017), the NE-SW striking Patan fault (Talwani et al., 1996; Talwani, 1997a) and the fault P1 parallel to the Patan fault (Talwani et al., 1996; Talwani, 1997a). Hot springs are aligned along the N-S Western Ghats escarpment (Pascoe, 1964; Valdiya K. , 1984). The presence of springs suggests a link of the hydrogeological regime with the occurrence of earthquakes in this area (see Chapter 2.1.2) (Arora et al., 2017). Talwani (1997a) proposed that the N-S striking faults/lineaments extend from the surface to seismic hypocentres, and act as preferential pathways for flows of fluid.

2. The NW-SE striking L1 to L7 lineaments, which seem to start from the Koyna River Fault Zone (KRFZ). L1 and L2 intersect with the Patan Fault, reaching probably P1, L3 extends towards the Warna Dam (Langston, 1981) and L4 to L5 reach P1 (Figure 2.2).

The seismicity has been divided in three main areas based on the epicentral and hypocentral distribution (Rai, 1999; Sarma & Srinagesh, 2007) (Figure 2.2):

(1) the North Escarpment zone (NEZ) with a NE-SW orientation parallel to the Donichawadi fault;

(2) the South Escarpment Zone (SEZ) with NW-SE orientation parallel and corresponding to the L6 and L7 lineaments and,

(3) the West/Warna Seismic Zone (WSZ) with orientation NW-SE parallel and corresponding to the L4 and L5 lineaments.

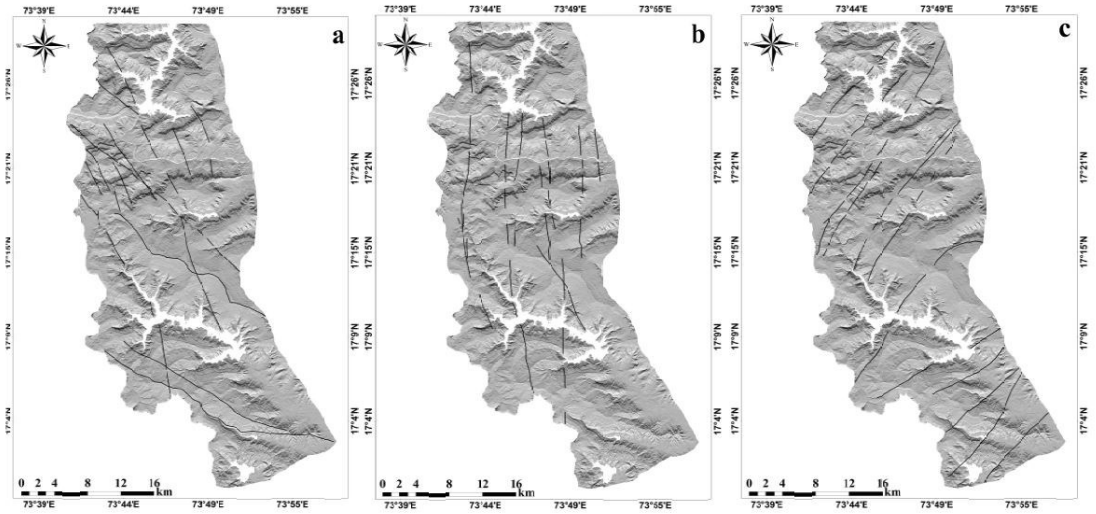

Figure 2.1. Lineaments delineated from LiDAR high resolution DEM in three directions (**a**) NW-SE, (**b**) N-S and (**c**) NE-SW (figure and caption from Arora at al., 2017).

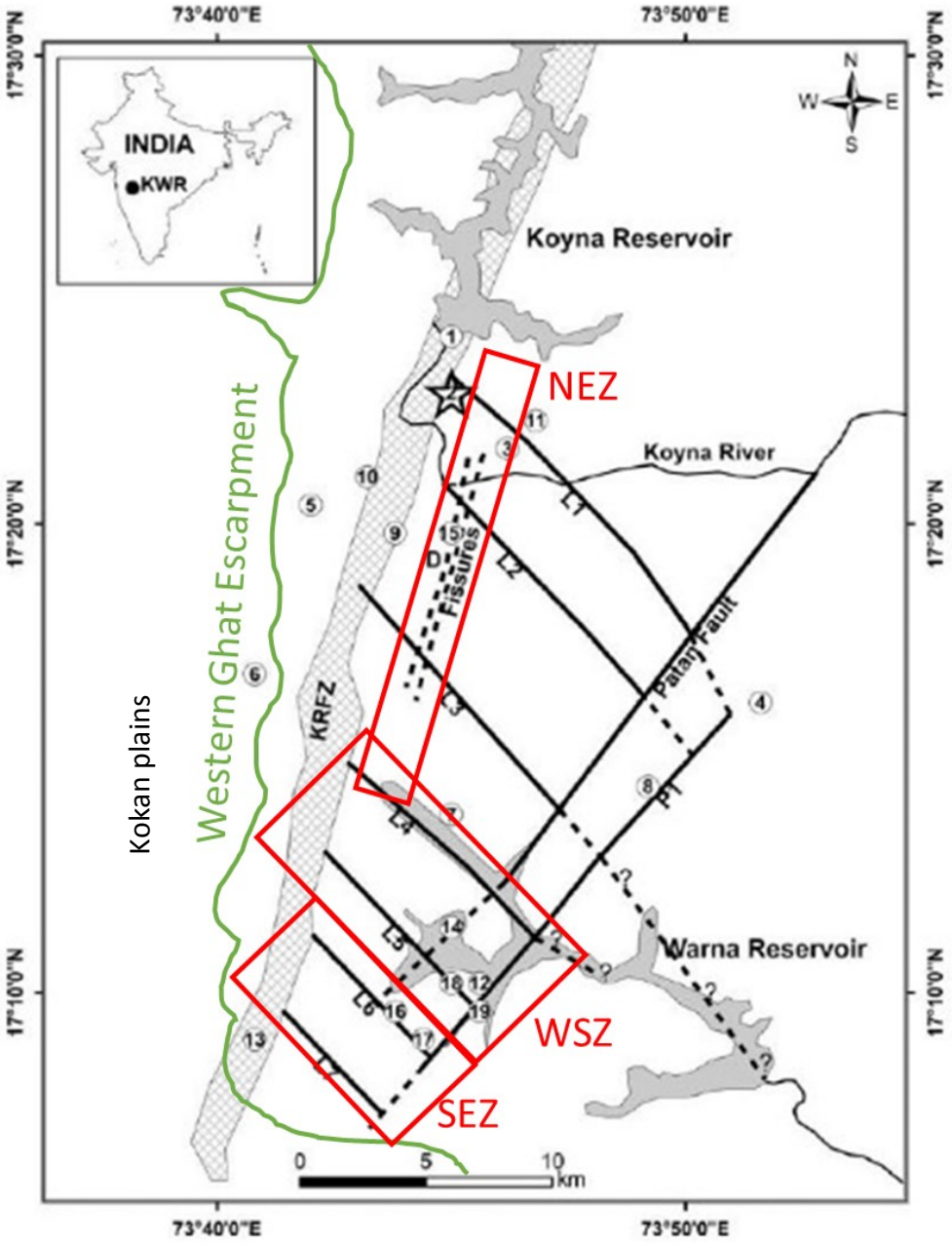

Figure 2.2. Location of Koyna–Warna region, showing the chronological locations of 19 M > 5 events, taken from Talwani et al. (1996), Gupta et al. (2002) superposed on the revised seismotectonic framework. D, near the word "Fissures" is the Donichawadi fault, with fissures associated with the 1967 shock. The red rectangles correspond to the three seismic zones (figure and caption from Dura-Gomez et al., 2009).

One of the most relevant faults in the Koyna area is the Donichawadi fault, belonging to the NEZ, and probably associated with the 10 December 1967 earthquake due to its proximity from the epicentre (inset Figure 2.3a), its NNE-SSW strike subparallel to the aftershock distribution and sinistral strike-slip (Harpster et al., 1979; Gupta et al., 1999). Soil helium monitoring and oblique drilling confirmed that the rupture surface

cracks were the expression of the Donichawadi fault zone which dips of 60° to the WNW (Fig. 2.3b).

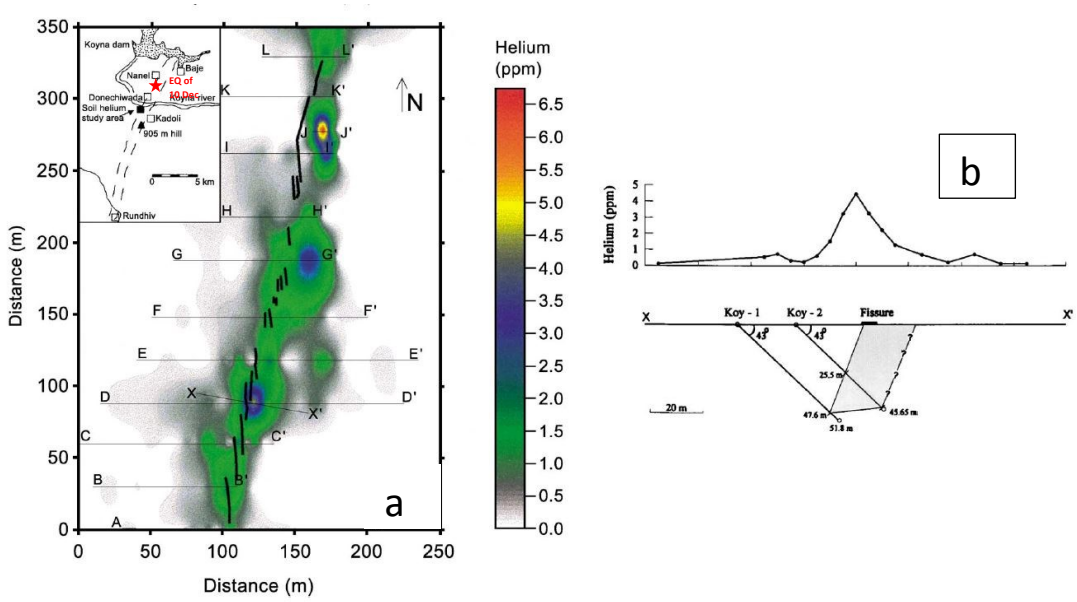

Figure 2.3 a) Map of Donichawadi fault zone—line in the inset SE of the Koyna Dam shows the location of area where soil helium was conducted. Solid rectangles indicate coincidence of helium anomalies with coseismic and en-echelon fissures created by 1967 earthquake (thick lines) in Donichawadi fault zone. Anomalies were established by soil helium measurements along 12 traverses (AAV to LLV) across the fissure system. The peak values of DDV, IIV and JJV are 4.5, 4.5 and 6.7 ppm respectively. XXV is the traverse where two borewells were drilled (figure and caption from Gupta, 2002); **b)** Koyna seismic fault reconstructed by drilling. The two boreholes drilled are on a WNW–ESE traverse, perpendicular to the general strike of the fissure zone. Solid circles show the bottom of the boreholes. The brecciated zone was met with in the subsurface between 47.6 and 51.8 m along KOY-1. In KOY-2, it was met with between 25.5 and 45.65 m along the hole. A 60° dip towards WNW for the fault is obtained by connecting the points of first intersection of the breccia zone in the two boreholes and its extrapolation to the surface fissure (figure and caption from Gupta et al., 1999).

The hypocentres are located in a maximum depth of about 13 km in the Koyna area and within 8 km in the Warna area (Rao & Shashidhar, 2016) (Figure 2.4). In both cases, the seismogenic volumes, located in the Proterozoic basement, appear as low-velocity zone possibly because they include a dense network of sub-vertical faults/fractures (Krishna et al., 1989). Estimate of earthquake hypocentral depths was derived using moment tensor inversion of broadband waveform data from selected earthquakes in the Koyna-Warna region, resulting in focal mechanism solutions based on the best-matched waveform criterion (Rao & Shashidhar, 2016). Focal mechanisms (50 in total) show a prevalence of normal faulting at shallow depth in the Warna region,

and, to a less extent, strike-slip faulting; reverse faulting mechanism is absent (Shashidhar, 2011).

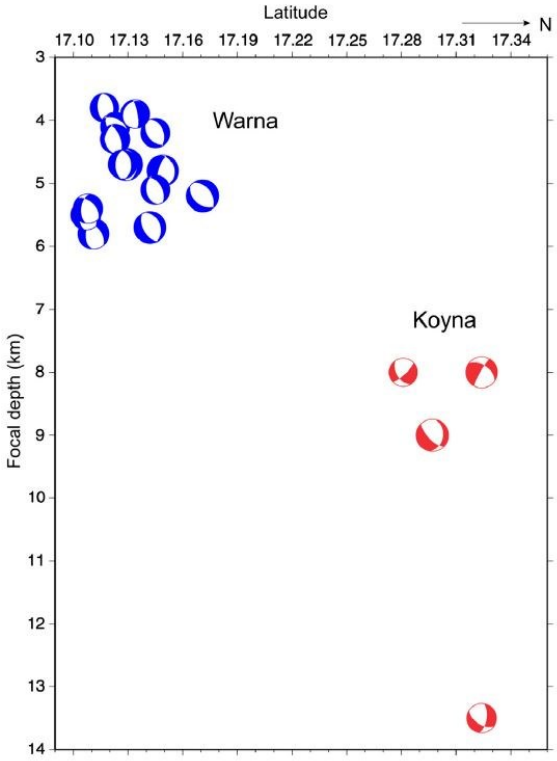

Figure 2.4. Focal mechanism solutions plotted in a North–South depth section across the Koyna and Warna regions. Note the distinct seismogenic depths of 4–6 km in the Warna region (red) and 8–13 km in the Koyna region (blue) (figure and caption from Rao and Shashidhar, 2016).

Goswami et al., (2020) calculated the principal horizontal stress S_{Hmax} orientation down to 3 km depth in the Koyna region to be N 9°W ± 17° (NW-NNE interval) from borehole breakouts and drilling-induced tensile fractures (DITFs) from borehole KFD1 (see location in Figure 1.1). This orientation is consistent with the one of the Indian Peninsular Shield (Rao & Shashidhar, 2016). The borehole KFD1 crosses the damage zone of the Donichawadi fault, which strikes NNE-SSW (Gupta, 1992; Gupta et al., 2017a) and, as a consequence, is parallel to the horizontal maximum principal stress of the Koyna region (Goswami et al., 2020). A series of steply dipping (40°-75°) fractures striking NNW-SSE to NW-SE were observed within the borehole from a depth of 2100 m; therefore, they are subparallel to the S_{Hmax} orientation and, therefore, quite favourable oriented for normal and strike-slip fault reactivation (Anderson, 1905). In fact, the focal mechanisms of the Koyna-Warna region are both normal and strike slip, with the first more common in the Warna area and the latter in the Koyna area (Rao & Shashidhar, 2016) (Figure 2.5). The stress regime in the Koyna-Warna region was also

inferred by both Rao & Shashidhar (2016) and Goswami et al. (2020) via stress inversion of earthquake focal mechanisms. The stress regime at Koyna has the maximum principal compressive stress (σ_1) vertical, the intermediate principal stress (σ_2) oriented NNW-SSE and the minimum principal stress (σ_3) having strike ENE-WSW (Figure 2.6a). The stress regime at Warna is similar: σ_1 vertical and the NNW-SSE and ENE-WSW directions coinciding with the intermediate principal stress (σ_2) and the minimum principal stress (σ_3) respectively (Figure 2.6a). Thus, if one were dealing with a normal fault regime σ_V would correspond to σ_1, σ_{Hmax} to σ_2 and σ_{hmin} to σ_3, whereas if one were dealing with a strike-slip σ_V would be σ_2, σ_{Hmax} to σ_1 and σ_{hmin} to σ_3 (Anderson, 1905). In Figure 2.6b are reported the fault planes (blue crosses) from the focal mechanism of the earthquakes in the Koyna and Warna area (Goswami et al., 2020). Looking at Figure 2.6b, it appears that the fault reactivation in Warna area is better described by Mohr-Coulomb fracture criteria than in the Koyna area (Goswami et al., 2020). Thus, the faults in the Warna area seem to be more critically stressed for normal faulting reactivation than in the Koyna area. This would be consistent with the common normal focal mechanisms in Warna with respect to both normal and strike slip focal mechanisms in the Koyna area (Figures 2.5 and 2.6c). In addition, the distribution of the histogram of shape ratios ($R=(\sigma_1-\sigma_2)/(\sigma_1-\sigma_3)$) shows a low value and wide distribution for earthquakes in both regions (Figure 2.6d), indicating that the magnitudes of the maximum and intermediate principal stresses are close to each other (Goswami et al., 2020). As a consequence, small changes in stress magnitude, also related to seismic stress drops, may trigger the transition from normal to strike-slip faulting (Goswami et al., 2020).

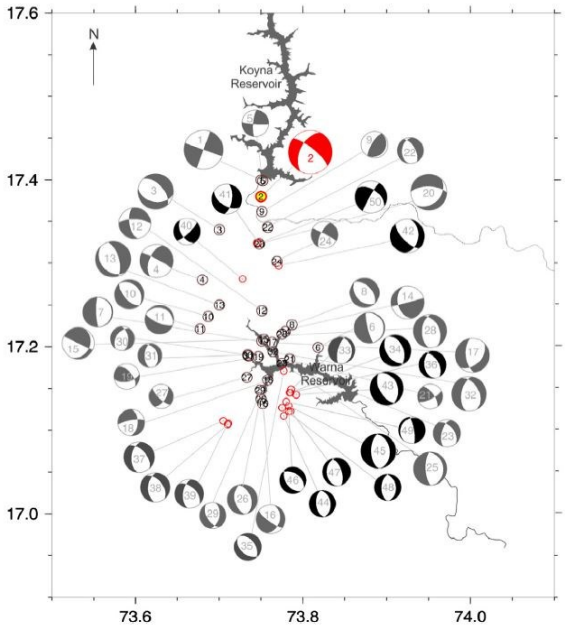

Figure 2.5. Strike-slip focal mechanism prevails around the Koyna area, while nomal mechanism mainly in the Warna reservoir (Figure from Rao and Shashidhar, 2016).

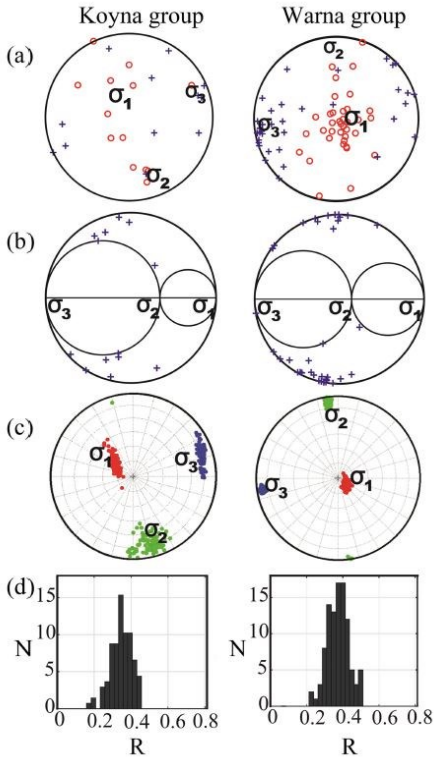

Figure 2.6. Plots illustrating results of iterative stress inversion of earthquake focal mechanisms of 50 earthquakes (M ≥ 3.6) from Koyna-Warna region. The left panel shows the results for Koyna group and right panel shows the results for Warna group. **a)** P (red) and T (blue) axes with retrieved principal stress directions, **b)** Mohr's circle diagram with positions of faults (blue plus signs), **c)** regimes of principal stresses σ_1, σ_2, and σ_3 shown with relative uncertainty by red, green, and blue solid circles, respectively, and **d)** histogram distributions of shape ratio (R) (figures and caption Goswami et al., 2020).

Rao & Shashidhar (2016) identified three different clusters of seismicity (Figure 2.7), which partly correspond to the NEZ, WSZ and SEZ of Figure 2.2:

1. The first cluster is the largest in size, has a NNE direction and crosses the Koyna Dam until it reaches the Kundi region west of Warna; it includes westward steeply dipping strike-slip faults near Koyna (Shashidhar, et al., 2013), and a network of subvertical normal faults west of Warna. In this region, there is a combination of the two faulting regimes (Goswami et al., 2020). This cluster most

likely corresponds to the North Escarpment zone (NEZ), which includes the Donichawadi fault;

2. The second cluster, located south of the Warna Reservoir, has a NNW trend and it includes sub-vertical normal faults dipping either eastward or westward. It corresponds to the southern limits of South Escarpment Zone (SEZ) and West/Warna Seismic Zone (WSZ);
3. The third cluster, located in the south-east of the Warna Reservoir, is possibly related to quarrying activities (Shashidhar et al., 2014).

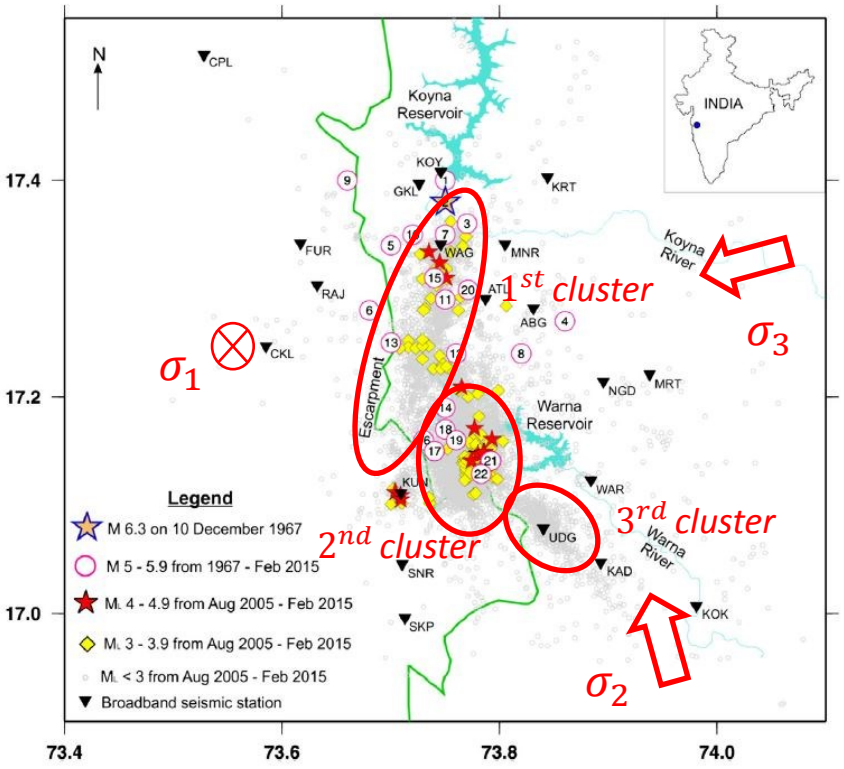

Figure 2.7. Representation of the three main earthquake clusters and the stress orientations in the Koyna-Warna region (figure from Rao and Shashidhar, 2016).

2.1.2. The role of water level fluctuations and pore pressure in Koyna

In the years following the impoundment of the Koyna Reservoir in 1962, the water level fluctuated because of load-unloading cycle and these fluctuations were correlated with seismic events (Gupta et al., 1972a, 1972b; Gupta & Rastogi, 1976; Kalpna & Chander, 2000; Gupta, 2002; Dura-Goméz & Talwani, 2009). Figure 2.8 shows the reservoir loading and unloading phases in 1973, 1980 and 1993 compared with the monthly frequency of M>4 earthquakes for the period 1970 to 1999. The loading phase (water impounding) increases from June until August, reaching a peak water level in August and then remaining stable and decreasing (unloading phase). The reason why the water level rises so rapidly is due to the monsoon rains, which account for 88% of the rainfall that falls throughout the year, approximately 7000-6000 mm, and impact on the hydraulic regime of the region (Naik et al., 2003). Therefore, in the monsoon season, seismicity is minimal at the beginning, but then increases until it peaks in September (rapid response seismicity). The frequency of earthquakes decreases until January, but then slightly increases in February, which is related to the reservoir unloading phase (possible delayed seismicity, see Chapter 1.1) (Rajendran et al., 1996). Thereafter, the seismicity decreases again till the minimum in July and then restarts in a new, monsoon/reservoir-modulated, cycle. Thus, there are persistent seismic activity peaks in the years, with the particular peak of December possibly due to pore pressure diffusion (Gupta, 2002). This cyclical behaviour has been repeated since 1962, although the last earthquake with M > 5 was recorded in 2017. The graphs in Figure 2.8 show the correlation between the fluctuation of the water level in the Koyna reservoir and the number of seismic events.

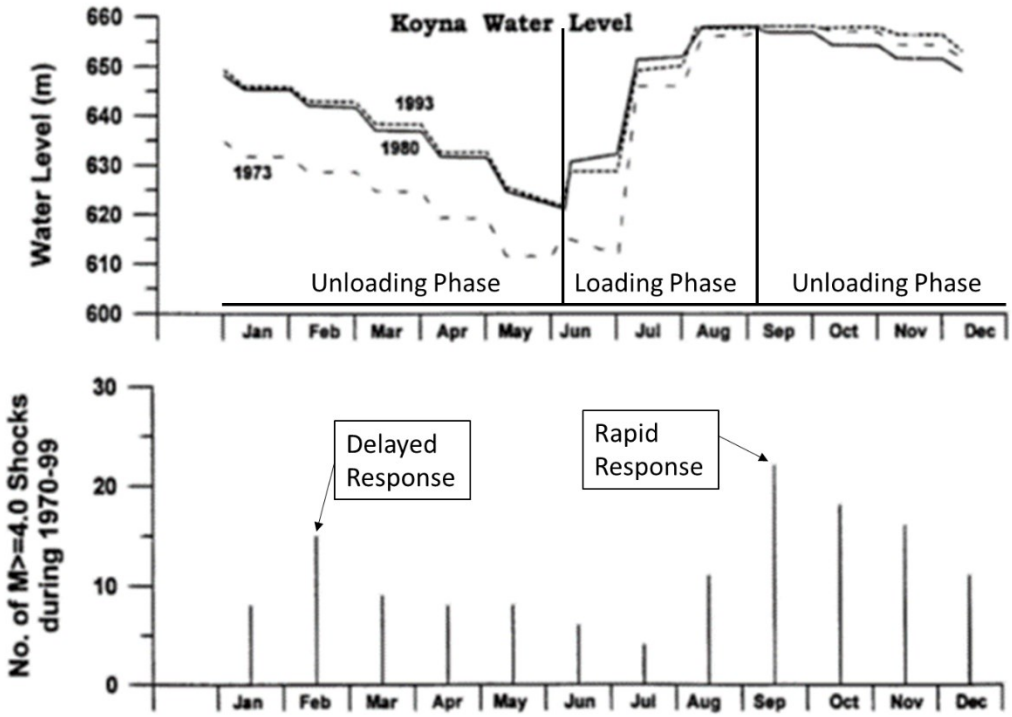

Figure 2.8. Water levels in Koyna reservoir for the years 1973, 1980 and 1993 and the monthly number of earthquakes of M 4 and larger for the period 1970 through 1999 (figure and caption from Gupta, 2002)

Thanks to the construction of 21 wells between 1995 and 1998 around the Koyna seismically active zone, a drop of a few centimetres in the water level was detected several days before an earthquake (Kuempel et al., 2017), defining the trend of water level fluctuation as a precursor to a seismic event; this drop was possibly correlated with an increase in porosity and permeability due to early fracturing, with subsequent recovery attributable to fluid inflow or compression (Roeloffs, 1988). Pressure transducers with a resolution of 1 mm were installed in these wells to measure the hydraulic pressure of the water column. By monitoring the change in water level, it was noted that the fluctuations in the well level responded to earthquake-induced changes in crustal volume deformation in the form of stepped co-seismic changes (Chadha et al.,2005; Kuempel et al., 2017) (Figure 2.9). These water-level changes are probably fluctuations in pore pressure related to changes in porosity volume caused by stress redistribution in the brittle crust (Bodvarsson, 1970; Kuempel, 1992; Muir-Wood & King, 1993). Another possible precursor to the earthquakes in the Koyna-Warna region are changes in chemical and stable isotope composition in the groundwater (Cl, SO_4 and F,

$\delta^{18}O$) (Reddy et al., 2017). The results on stable isotope contents indicate a long-term change in stable isotopes, which could be related to the build-up of stresses taking place before the earthquake. The changes in spring water compositions are attributed to the mixing of two aquifers with different ion concentrations due to the accumulation of stresses prior to the occurrence of the earthquake (Reddy et al., 2017).

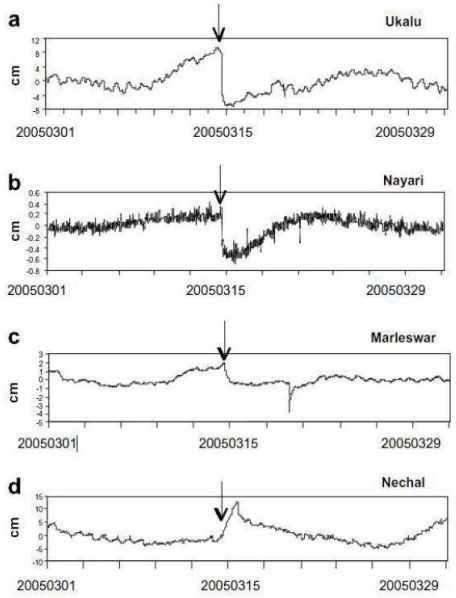

Figure 2.9. Co-seismic water level anomalies in wells **(a)** Ukalu, **(b)** Nayari, **(c)** Marleswar, and **(d)** Nechal wells. The arrow shows the time of the local M5.1 earthquake on March 14, 2005. As can be seen there is a drop of a few cm in the water level in the wells (figure and caption from Kuempel et al., 2017).

The seismicity in the region underwent changes over space and time related to the construction and infilling of the two reservoirs of Koyna and Warna. In the first twenty years, only the area around the Koyna reservoir was seismically active, while from 1993 onwards also the area around the Warna reservoir was active. In particular:

- Pre-Warna reservoir (1968-1993): the first filling of the Koyna reservoir in 1962 triggered a pore pressure front that propagated over time beneath the reservoir, possibly thanks to an underground permeability of 10^{-15}-10^{-14} m^2 capable of generating pore pressure variations of 0.1-1 MPa up to 10 km depth in the vicinity of the reservoir (Hazarika et al., 2017). Due to the Terzaghi effect, this pore pressure perturbation facilitated earthquake triggering, including the 1967 Mw 6.3 earthquake, which occurred five years after the reservoir was filled (Hazarika et al., 2017). The infiltration of water beneath the Koyna reservoir was mainly controlled by the N-S fracture network (Arora et al., 2017) (Figures 2.1, 2.10), leading to a pore pressure increase also south of the Koyna reservoir,

which triggered the earthquakes during the September filling cycle (loading peak/rapid response phase visible in Figure 2.11) (Talwani & Acree, 1985). The migration of the pore pressure front triggered further earthquakes in December (unloading peak/delayed response) (Arora et al., 2017). Earthquakes were triggered up to 25 km south of Koyna dam, near Warna Reservoir, and were mostly deep, 5-13 km (Gupta, 2002).

- Post-Warna reservoir (1994-2013): additional water infiltration, even if probably small in volume, began from the Warna reservoir into the same fracture network; this led to an increase of seismicity especially after the Warna reservoir reached its full capacity in 1993 (Arora et al., 2017). While the peak of seismicity in September and December, though reduced, was still there, the combined impact of the Koyna and Warna reservoirs resulted in a new peak of seismicity in March-April (delayed response), with most earthquakes nucleating at shallow depth (<10km, Arora et al., 2017) (Figures 2.10, 2.11). The variation in seismicity peaks suggests a change in the hydrogeological system (Arora et al., 2017). Of course, the impounding of the Warna reservoir resulted also in the migration of the seismic activity to the south (Rastogi et al., 1997).

Clearly, the Koyna-Warna region has a complicated evolution, especially after the construction of the second reservoir of Warna. The causes of the seismic events, which lasted for years in the Koyna region, include several factors that together led to the emergence of an RTS zone. The main are: the annual monsoon events that fill the reservoirs, the dense network of faults that act as a preferential pathway for fluids and the normal regime that allows the faults to be reactivated. All of this allows the increase and the diffusion of pore pressure that is the trigger of earthquakes (RTS) (Simpson et al., 1988).

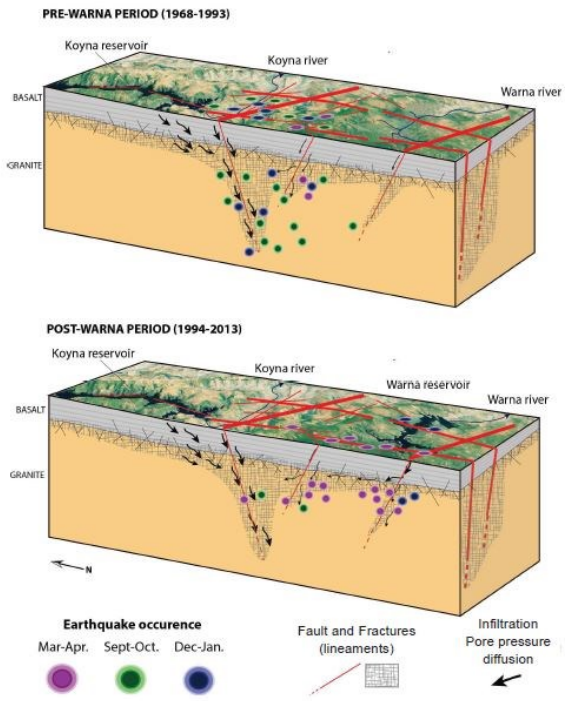

Figure 2.10. A cartoon showing the conceptual model to explain the seismic activity along the main N-S fault system and fracture zone and the impact of Warna reservoir impounding in changing hydro-geological regime and shift in seismicity (figure and caption from Arora et al., 2017).

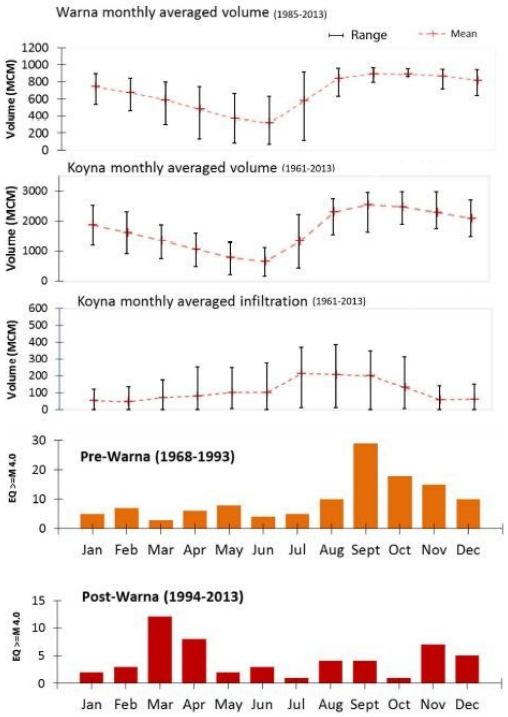

Fig.2.11. Monthly averages of the Warna and Koyna reservoir volumes over the years since their respective impoundment and monthly averages of the infiltration volume of the Koyna reservoir. Monthly distribution of earthquakes (M>4.0) during pre Warna (orange) shows prominent peak during September, which declining trend till December and during post Warna (brown) March April peak becomes prominent with diminished peaks in September and December. (figure and caption from Arora et al., 2017).

2.2. Seismicity from 1962 to today

The filling of the Koyna reservoir began in 1962 and the first earthquake was recorded and felt in the same year, during the monsoon season, by residents in the area (Gupta, 1992; Arora et al, 2017). The initial reservoir-filling phase lasted until 1965 and was associated with an increase in seismic activity near the dam (Guha, et al., 1968). On 30 August 1967, the overcoming of the previous reservoir water level, probably caused the first moderate in magnitude (Mw 5.2) earthquake of 13 September 1967. However, the water level was further increased until October 1967. This was followed by the 10 December 1967 Mw 6.3 earthquake, and by 46 aftershocks of Mw > 4, including five Mw>5 over the next three days, the last of which was on 29 October 1968 (Gupta, 1969; 2002). After the Mw 6.3 earthquake, the activity migrated south (Gravilenko et al., 2010). The most distant seismic event was located 20 km south-east of the dam on 24 December 1967, together with other aftershocks of Mw4 near the future Warna reservoir. On 2 September 1973, the maximum water level was again exceeded, triggering an increase in seismicity until the Mw= 5.1 earthquake of 17 October 1973. In this case, the sequence was less intense. It is not known why the seismicity at Koyna is continuous or even why this last seismic event was less intense than the previous 1967 one. Perhaps the 1967 Mw 6.3 released a relevant part of the elastic strain energy stored in the area. Surely, factors that influence the seismicity at Koyna are: the rate of rise of the water level in the reservoir, the maximum water level reached and the duration of water level maintenance (Gupta et al. 1972 a,b; Gupta, 2002). On 2 September and 20 September 1980, there were two earthquakes of Mw 5.5 and Mw 5.3 respectively, triggered once again the water level was exceeded. Both epicentres were 25 km south of the Koyna Dam and were probably generated by different faults that were, however, connected to the Koyna Basin by the more conductive N-S striking faults/fractures (Talwani, 1997a; Arora et al., 2017). Thereafter, the seismicity was drastically reduced until the filling of the Warna reservoir between 1985 and 1993. There were two earthquakes with Mw>5: on 8 December 1993 and 1 February 1994, at distances of approximately 13 and 25 km from Warna Dam, respectively. The last event was associated with a normal fault on the Patan Fault, while the aftershocks were located along L2 (Dura-Goméz & Talwani, 2009). These two events occurred 158 and 213 days, respectively, after the 1992 reservoir water level exceedance, showing evidence of pore

pressure diffusion (Simpson et al., 1988) to the northwest of Warna Reservoir, along the same series of fractures that were associated with southward pore pressure diffusion from Koyna Reservoir during previous episodes. In these two and a half years, between July 1993 and December 1995, there were 127 earthquakes of $3 < Mw < 3.9$, 8 of $4 < Mw < 4.9$, and 2 of $Mw > 5$, whereas in the previous 2.5 years there were only 30 earthquakes of $3 < Mw < 5$ (Rastogi et al., 1997). The epicentres of the earthquakes are aligned along two subparallel NNE direction separated by 5-10 km, possibly the Donichawadi fault, and the Bhogiv Fault, which crosses the Warna reservoir; the latter should correspond to Dura-Goméz's P1 (2009), which is parallel and close to the Patan fault (Rastogi et al, 1997). From here onwards, a phase of declining water levels followed, where two events were recorded in March and April 2000, about 10 km south of the Warna Dam, in an area that had so far been aseismic. In addition, they were recorded a full year and a half after the last water level rise. The last earthquake of $Mw>5$ was recorded on 3 March 2005 and again it was a year and a half after the water level was exceeded. A further increase in the seismic phase took place in 2009-2010 when two earthquakes of $Mw>5$ were recorded on 14 November and 12 December 2009 near Warna, while in the area near the Koyna reservoir, no earthquakes of $Mw>4$ had been recorded for years (Gupta et al., 2011). Finally, the seismic activity subsided and the last relevant event was recorded on 3 June 2017 of $Mw=4$ (Anuradha & Malika, 2017, see Figure 2.12 for the entire seismicity from 1966 to 2018).

A clear distinction can be made, as already done in Chapter 2.1.2, between pre- and post-Warna seismic events: earthquakes occurring before 1993 are a manifestation of crustal-scale stress memory and are related to the operations in the Koyna reservoir, while tremors recorded after 1993, located closer to the Warna area, can be explained by the change in the hydrogeological regime, which perturbed the regional stress (Arora et al., 2017).

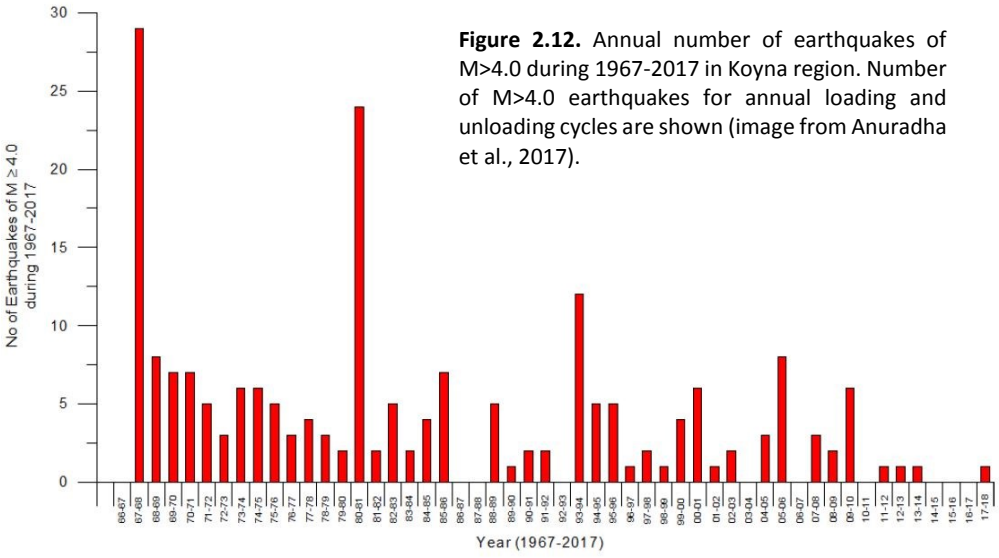

Figure 2.12. Annual number of earthquakes of M>4.0 during 1967-2017 in Koyna region. Number of M>4.0 earthquakes for annual loading and unloading cycles are shown (image from Anuradha et al., 2017).

2.3. Deep drilling project

Because the fault/fracture network is buried beneath 1-2 km thick basalt Deccan traps, it was decided to set up a large deep drilling project (Scientific Deep Drilling Project in Koyna). After a workshop held in 2011, organised by the National Geophysical Research Institute (NGRI) and supported by the Ministry of Earth Sciences (MoES), the Indian government and the International Continental Scientific Drilling Program (ICDP), it resulted that was the ideal site for the construction of a large deep observatory designed for continuous monitoring of human-induced earthquakes (Gupta et al, 2011). The infrastructure improved the localization of earthquake hypocentres through the installation of seismometers along the wells. In fact, the seismic stations at the surface had large errors of hypocentral localization (Gupta et al., 2014). Therefore, the installation of deep boreholes with built-in seismometers improved the detection and location capability by an order of magnitude. The construction of the nine wells took place between 2011 and 2014 (Gupta, 2017b) (Figure 2.13). Subsequently, in a second workshop held in 2014 in Karad it was decided to improve the geological knowledge of the basement below the Deccan traps. This resulted in the selection a suitable location for the installation of two new 3-5 km deep pilot boreholes to further enhance the hypocentre location capability, reaching an error of 100 m in the horizontal (Figure 2.14). The first pilot well (KFD1) was drilled in December 2016 and was completed in June 2017. The drilling was 3000 m deep, close to KBH7 and intersected the Archean basement at 1247 m depth (Gupta, 2017b). The preliminary results from the Scientific Deep Drilling Project in Koyna are very promising, as they allowed to constrain the thickness of the Deccan Traps, the geology of the underlying granitic basement, and, relevant for the purposes of this thesis, the proposal of a new and better constrained thermal model, an improved knowledge of the fault network and, thanks to continuous coring, the collection of host and fault zone rock specimens from hypocentral depths.

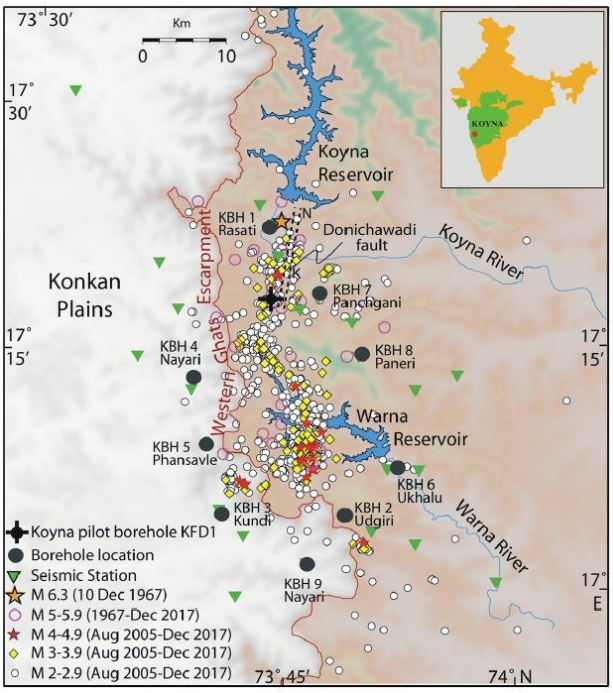

Figure 2.13. Koyna-Warna region showing the locations of the nine deep boreholes of the ICDP (figure from Misra et al., 2022).

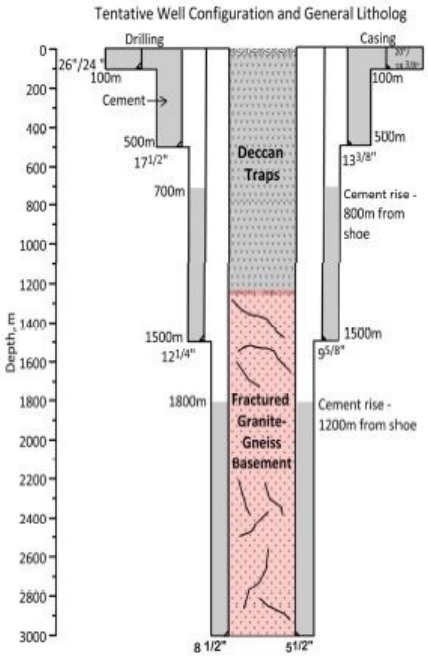

Figure 2.14. Generalized configuration of the 3000 m deep pilot borehole. The borehole entered the basement at a depth of 1247 m after a penetrating through the basalt column (figure from Gupta, 2017b).

3. Geological setting of the Koyna-Warna area

3.1. Geodynamics of Indian plate

The Koyna-Warna region is located in the western portion of the Deccan volcanic province (DVP) in the Indian plate (Figure 3.1). The latter is composed of the Indian craton and a portion of the Indian Ocean seafloor, and bounded to the southeast by the Australian plate, to the southwest by the African plate, to the north and northeast by the Eurasian plate, and to the west by the Arabian plate (White & Lister, 2012) (Figure 3.2). van Hinsbergen, (2011) studied the geodynamic evolution and the drift towards the north of the Indian plate. The separation between the Indian plate and Gondwana occurred around 130-120 Ma as a result of the spreading of the ocean floor between India and Antarctica-Australia (Gaina et al., 2003, 2007). At that time, the Indian plate was surrounded to the south by other oceanic spreading centres and to the north by subduction zones. A second oceanic basin formed ~90 Ma between India and Madagascar (African plate), associated with the onset of the Morondova Large Igneous province (LIP). Subsequently, the Indian plate fragmented due to the separation of India from the Seychelles around ~65 Ma. The break-up was associated with the formation of the Deccan Traps. After the late Cretaceous phase of arc-continent collision, around 55-50 Ma, a major episode of continental subduction began, followed by continent-continent collision between the Indian and the Euroasian plate. Around 50 Ma, the Indian plate interacted with the Reunion hot-spot. From here onwards the compressional phase prevailed resulting in the formation of the Himalayan Mountain belt, which is still uplifting (Figure 3.3).

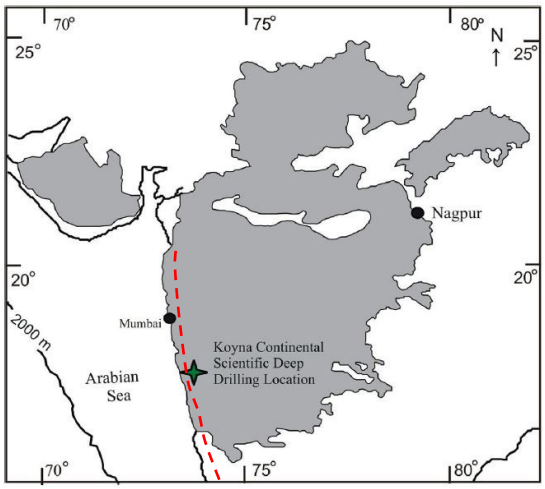

Figure 3.1. Geological map showing the areal spread of the Deccan flood basalt eruptions and location of the Koyna International Continental Deep Drilling Project. The dot red line is the WG (figure and caption taken from Venkateshwarlu et al., 2022).

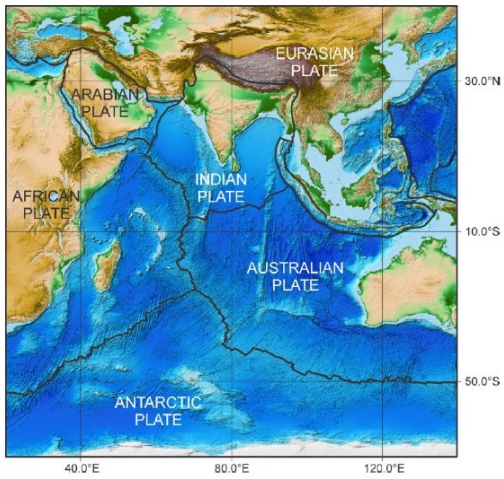

Figure 3.2. Topographic and bathymetric map of Indian ocean showing the location of the boundaries of the African, Arabian, Antarctic, Australian, Indian and Eurasian tectonic plates (figure and caption from White and Lister, 2012).

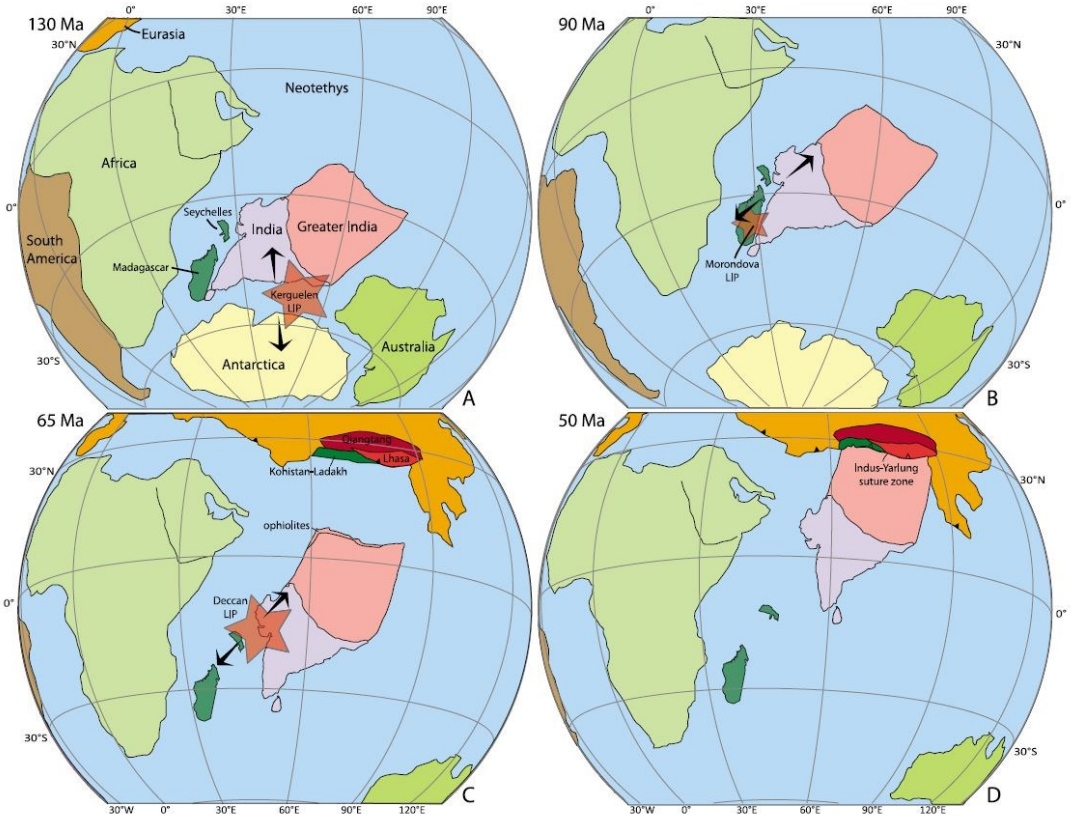

Figure 3.3. Plate reconstructions showing the configurations of India at **(a)** 130 Ma, at the initiation of the India-Antarctica/Australia separation and the onset of the Kerguelen LIP; **(b)** 90 Ma, at the initiation of Madagascar-India separation and the onset of the Morondova LIP; **(c)** 65 Ma, at the initiation of India-Seychelles separation and the onset of the Deccan LIP; and **(d)** 50 Ma, during the early stages of India-Asia collision (figure and caption from van Hinsbergen et al., 2011).

Regarding the deformation of the Indian craton, it was thought to be stable, having a strong, thick and cold lithosphere (Pandey et al., 2013). However, the occurrence of seismic events, such as those in the Koyna-Warna area could be indicative of minor deformation (3 ± 2 mm/year) within the Indian subcontinent, as well as along the northern plate boundary where large earthquakes are frequent as a result of the continent-continent collision with the Eurasian plate (Paul, et al., 2001; Bilham et al., 2003). In any case, the Indian subcraton in the Koyna-Warna area seems critically stressed: within just 35 years after the 1967 Koyna earthquake, the number of earthquakes per year within the Indian plate doubled (Bilham & Gaur, 2000). This suggests that stresses within the plate are high due to the Indo-Asian collision, and earthquakes occur within regions of rheological weakness (Gowd et al., 1992). These weaknesses concentrate stress inside plate triggering rare but devastating intra-plate earthquakes (King & Bilham, 1973). Human activities, such as dam construction, may also trigger earthquakes in this critically stressed and heterogeneous subcontinent (Bilham et al., 2003).

3.2. Geological setting of the Koyna-Warna area

The Koyna-Warna region is a hilly area located on the western edge of the Mahabaleshwar Plateau, at an average elevation of 1200 metres above sea level, and separated from the lower areas to the west by a prominent escarpment called the Western Ghats (WGE) (Figure 1.1). The latter, has a north-south trend and extends for as much as 1500 km parallel to the Indian Ocean coast. This escarpment formed as a result of rifting and the separation of India from the Seychelles and is closely related to the Deccan Traps magmatic event (ca. 65 Ma) (Radhakrishna et al., 2019). The Koyna Basin has a N-S trend and is parallel to the escarpment from the Western Ghat (Subbarao & Courtillot, 2017). The Deccan Traps (also DVP) are bounded by the Bastar, Aravalli-Bundelkhand and Dharwar cratons to the east, north and south, respectively. Beneath this thick layer of basaltic lava flows is the crystalline basement, of Neoarchean age, composed of granitic, gneiss and amphibolite rocks. The thickness of the DVP varies greatly the east to the west of the WGE. In particular, based on borehole data from the Scientific Drilling Project in Koyna, basaltic flows are about 500 m thick to the west and 1000-1200 m thick to the east in Koyna-Warna area (Misra et al., 2017).

3.2.1. Proterozoic Basement in Koyna area

The basement is not outcropping in the area because covered by the Deccan volcanics. Therefore, before the Scientific Drilling Project in Koyna, information regarding the crystalline basement came from indirect studies such as:

1. Rare occurrences of crustal/mantle xenoliths (Duraiswami & Karmalkar, 1996; Dessai et al., 2004);
2. Coring in a few locations, mainly along the peripheral parts of the DVP;
3. Geophysical data (e.g., Kaila et al.,1981; Sain et al., 2002; Praveen Kumar & Mohan, 2014; Rao et al., 2015; Deshpande & Mohan, 2016).

In Koyna, the crystalline basement is probably an extension of the Neoarchean granitoid of the Dharwar Craton (south of Koyna), which splits into western and eastern (Rao et al., 2013; Roy, et al., 2013). The crystalline basement of Dhawar preserves a

record of multiple magmatic events, deformations and accretionary terranes of ages between 3.5 and 2.5 Ga (Bhaskar Rao, et al., 2017). Instead, the precise age at which the basement in the Koyna-Warna area was placed is not yet well known: Upadhyay, (2015) inferred that it formed 2.53 Ga and metamorphosed/deformed at 2.46 Ga and 2.37 Ga, while Bhaskar Rao et al., (2017) suggests that the granitic basement formed 2.7 Ga (Archean). However, thanks to the Scientific drilling project it has been possible to reach the upper Indian basement (Tripathi, 2012; Misra et al., 2017). Misra et al. (2017) recognised the main magmatic and metamorphic rocks located below the Deccan Traps, which include granite, granite-gneiss, migmatite-gneiss and amphibolite. U/Pb Zircon ages yield 2710 ± 63 Ma and 2700 ± 49 Ma for granodiorite and monzogranite, respectively, of the Koyna area (Bhaskar Rao et al., 2017). These rocks are typical of the cratons of the Indian Peninsula (Bhaskar Rao et al., 2017; Misra et al., 2017) and represent an adamellite-granodiorite-tonalite suite (Kumar Shukla et al., 2022). The basement rocks have a mantle origin, later contaminated by crust or by a mixing process (Kumar Shukla et al., 2022).

The rock samples I will be studying relate to three of the nine boreholes of the drilling project, which are: KBH-1 (Rasati), KBH-6 (Ukhalu) and KBH-7 (Panchgani) (Fig. 2.13). Therefore, I will focus on the description of the basement rocks from these three wells, although in general the basement is similar in the entire Koyna-Warna area. Misra et al., (2017) described the petrography, mineralogy and geochemistry of these three wells (Figure 3.4):

- KBH-1 (Rasati): lies very close to the epicentre of the Mw 6.3 1967 earthquake. The basement section from 932.5-1522.5 m depth is predominantly composed of: granite-gneiss (~60%) (Figure 3.5a), migmatitic gneiss (~25%) (Figure 3.5b), granite (~10%) (Figure 3.5c-d), amphibolite and other mafics (~5%) (Figure 35e). The granite-gneiss are well-preserved include alternating ca. 3 cm thick sub-parallel bands made of felsic (feldspar and quartz) and mafic (biotite and hornblende) minerals. The granitic gneiss includes mafic enclaves and are cut by fine-grained basic dykes, very coarse-grained acid pegmatites and quartz-epidote bearing veins (Sinha et al., 2017). Migmatitic gneisses consist in leucosomes composed of quartz, K-feldspar, plagioclase and as accessories chlorite, biotite, Fe-Ti oxides, epidote, apatite and zircon; melanosomes include

amphiboles, epidotes, chlorite, quartz, plagioclase and opaque minerals. Very frequent are reddish-brown in color haplitic/granitic vein systems. Granitoids have a peralluminous character (alumina saturation index: 1.12-1.62), $K_2O/Na_2O < 1$, indicating the predominance of sodic granitoids with calcic to alkalic affinity (Bhaskar Rao et al., 2017). According to the Streckeisen (1976) petrological QAP classification, the rock samples from KBH-1 are tonalites, granodiorites, monzogranites, quartz-monzogranites and monzodiorites (Figure 3.6).

- KBH-6 (Ukhalu): the basement from 775.04-1503.0 m depth is mainly composed of granite (~55%), amphibolite and other mafics (~20%), granitic gneisses (~15%) and migmatitic gneisses (~10%). The cores are mostly crushed and fractured throughout the section (Figure 30f). Steeply dipping shear fractures cutting the gneiss are common and their intensity is higher than in KBH-1 and KBH-7 cores (Misra et al., 2017). The granite and gneiss are similar to those found in KBH1.
- KBH-7 (Panchgani): the basement section from 1251.23-1500.7 m depth is mainly made by migmatitic gneiss (~60%), granite-gneiss (~20%), granite (~15%) and amphibolite (~5%). The entire section is preserved and the samples recovered as cylindrical cores. The granites have igneous structures with interlocking grain arrangements (the same applies to KBH1). Hornblende is present as a metamorphic mineral in the mafic domains of migmatitic gneisses and amphibolites. The basement rocks are cut by steeply-dipping basaltic dykes of the DVP (Figure 3.5g).

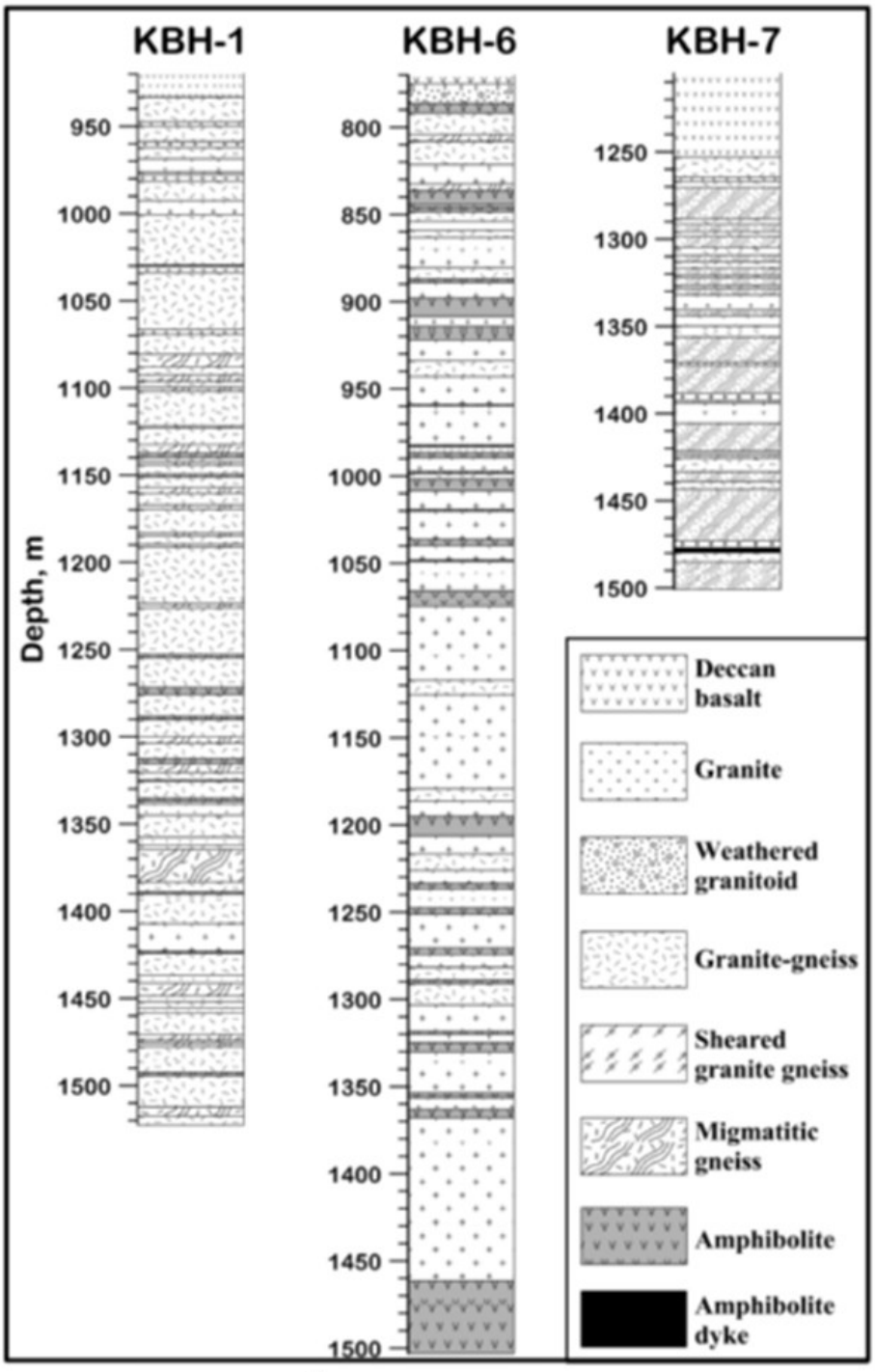

Figure 3.4. Detailed lithology of granitic basement sections from three boreholes KBH-1, KBH-6 and KBH-7 in the Koyna region. The dominant rock types constituting the basement are granite, granite-gneiss and migmatitic gneiss. The proportions of these constituents vary between the different borehole sites (figure from Misra et al., 2017).

Figure 3.5a. Gneiss granite from KBH1 recovered at 1039 m deep (sample KBH1-346). The core is cut by a subvertical fault filled by Chlorite and later Calcite.

Figure 3.5b. Proterozoic Migmatitic gneiss from KFD1 with alternation of leucosomes (white bands) and melanosomes (black bands) (photo by Di Toro, 2019, Karad repository).

Figure 3.5c. Granite cut by a steeply-dipping fault filled first by chlorite and then by later calcite veins (photo by Di Toro, 2019, Karad repository).

Figure 3.5d. Granitoid, possibly a tonalite, KFD1, cut by a steeply-dipping epidote-bearing fault (photo by Di Toro, 2019, Karad repository).

Figure 3.5e. Amphibolite from KBH-5, cut by chlorite joints (photo by Di Toro, 2019, Karad repository).

Figure 3.5f. Fractured and altered foliated shear zone from KBH6 (photo by Di Toro, 2019, Karad repository)

Figure 3.5g. Contact of the Archean wall (left) with a volcanic (Deccan) dyke from a core in KBH7. The steeply-dipping chlorite band of growth fibers marks the contact. (photo by Di Toro, 2019, Karad repository)

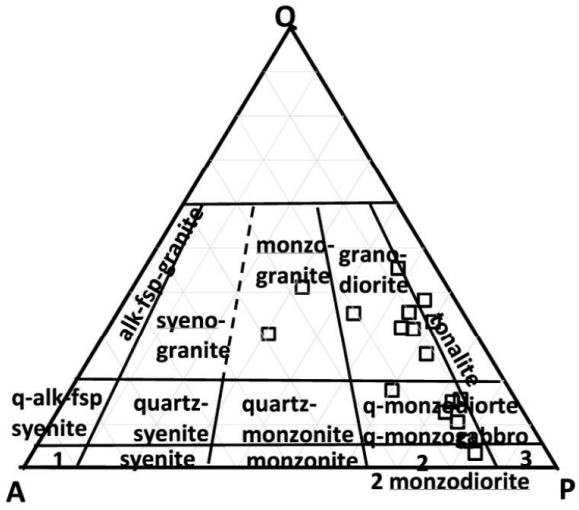

Figure 3.6. Petrological classification based on Quartz (Q) Alkali feldspar (A) and Plagioclase (P) abundances (after Streckeisen, 1976) for basement rocks from KBH-1 borehole (figure from Bhaskar Rao et al., 2017).

Ray et al., (2021) measured the petrophysical properties (e.g., rock density, porosity, thermal conductivity) and radioelements content of both Deccan basalts and the underlying basement plus the heat flux (ca. 45 mWm^{-2}, see also Gupta et al, 2015) in borehole KBH-5 (Phanasavale, Figures 1.1, 2.13) to model the geothermal gradient down to 10 km depth. These depths correspond to those of the most deep-seated human-induced earthquake hypocenters in the area. The modeled geothermal gradient ranged from 16 to 25 °C/km, or 165°-250° at 10 km depth (Figure 3.7 a, b).

Because of the Deccan traps cover, the Proterozoic basement rocks were not affected by weathering and erosion over the past 65 million years. Goswami, et al., 2017 tested in triaxial machine 181 rocks samples stem from boreholes KBH-3, KBH-4A, KBH-5 and KBH-7 and found that they failed preferentially along steeply-dipping (= sub-parallel to the borehole) fractures filled by secondary minerals. The strength of the basement rocks is variable because of their different composition, but especially because of the high spatial variability of the density of these secondary/minor fractures (Goswami et al., 2017).

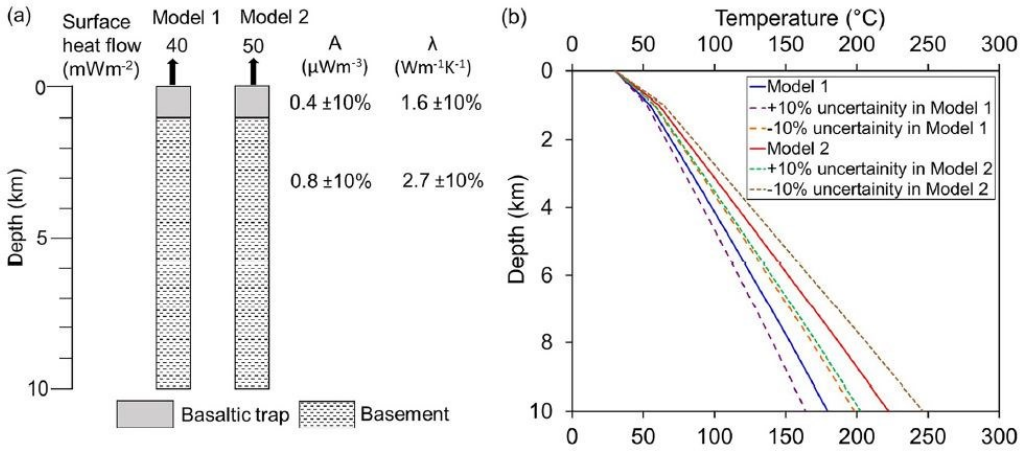

Figure 3.7. **(a)** Crustal heat production/thermal conductivity model up to 10 km, **(b)** Temperature estimates up to 10 km of the Koyna−Warna region, Deccan Volcanic Province, India. A: heat production (with ±10% uncertainty); λ: initial thermal conductivity (with ±10% uncertainty); b: 0.0007 K^{-1}; c: 0.0015 km^{-1}, where b and c are temperature and pressure coefficients of thermal conductivity, respectively (figure and caption from Ray et al., 2021)

3.2.2. Deccan Traps

The Deccan Traps are a km-thick sequence of basaltic flows commonly interspersed with much thinner sedimentary layers or volcanic ash beds (Sheth & Cañón-Tapia, 2015), plus nepheline syenite, alkaline trachyte and carbonatites found in dykes, sheets and plugs cutting the traps (Sen & Chandrasekharam, 2011). The DVP, is localized in the western part of India, is extended overs 500.000 km^2 with a volume of 1 X 10^6 km^3 (Dessert, et al., 2001) (Figures 3.1, 3.8a). The DVP has been put in place during several pulses between 68 and 60 Ma with the highest peak around 65.6 Ma (Hooper et al., 2010; Baksi, 2014; Schoene, et al., 2015). The thickness of the Deccan basalt in the Koyna-Warna region is estimated to be between a few hundred metres and a few kilometres by geophysical surveys (Kailasam et al. 1976; Kaila et al., 1981), while in the rest of the region it can exceed 2000 m in thickness, especially north of the Western Ghat; hence a southward dipping of the successions that make up the DVP is assumed (Beane et al., 1986) (Figure 3.8b). The contact of the Deccan Traps with the Proterozoic basement is sub-horizontal and sharp (Roy et al., 2013), and subparallel to the topography in the western portion (Subbarao & Courtillot, 2017). Instead, in the easternmost portion, corresponding to the Koyna area, based on the data from the ICDP wells, the original topography of the basement was irregular or there was a small fault (Vaidyanadhan & Ramakrishnan, 2010; Valdiya K. , 2010). In addition, there are three major dyke swarms in the Deccan Trap (Auden, 1949; Deshmukh & Sehgal, 1988;

Vanderkluysen et al., 2011): one of them is the ENE trending Narmada-Tapi dyke swarm (e.g. Melluso et al., 1999; Ray et al, 2007); and other two are the north-trending Western coast dyke swarm and the NNE-trending Pune Nasik dyke swarm (Barbar et al., 2017).Two types of basaltic flows, up to 50 m thick, were distinguished in the Deccan Traps: compound and simple (Walker, 1972). (Mishra, et al., 2017) first described a complete succession of DVP basaltic flows using the KBH-7 well. He found a total of 46 basaltic flows with a predominance of simple ones, up to 78 m thick, while compound ones are up to 52 m thick. The flows are mainly made by massive (74%), vesicular and amygdaloidal basalts (24%). The basaltic flows are made by clinopyroxene phenocrysts, olivine and plagioclase (Sinha et al., 2017), while the background paste contains quartz, biotite, zeolite, calcite, Fe and Ti oxides and glass (Mishra et al., 2017; Banerjee et al., 2021).

The simple flow (Figure 3.9a) has massive basalt at the base, vesicular basalt and amygdaloid in the middle-upper portion and a top “red bole” (Figure 3.10a). The latter corresponds to a *hiatus* between flows due to clays from basalt alteration at the ground surface, before being covered by the successive flow, and the basal breccia of the upper lava flow.

The compound flow (Figure 3.9b) contain at least ten flow units and include tube-like vesicles in the basal flow unit, more massive basalt in the centre and a highly vesicular and brecciated basalt at the top. The basalts often are fragmented and then cemented by a secondary minerals, mainly calcite, which also fills the vesicles (now amygdalae) (Figure 3.10b, c).

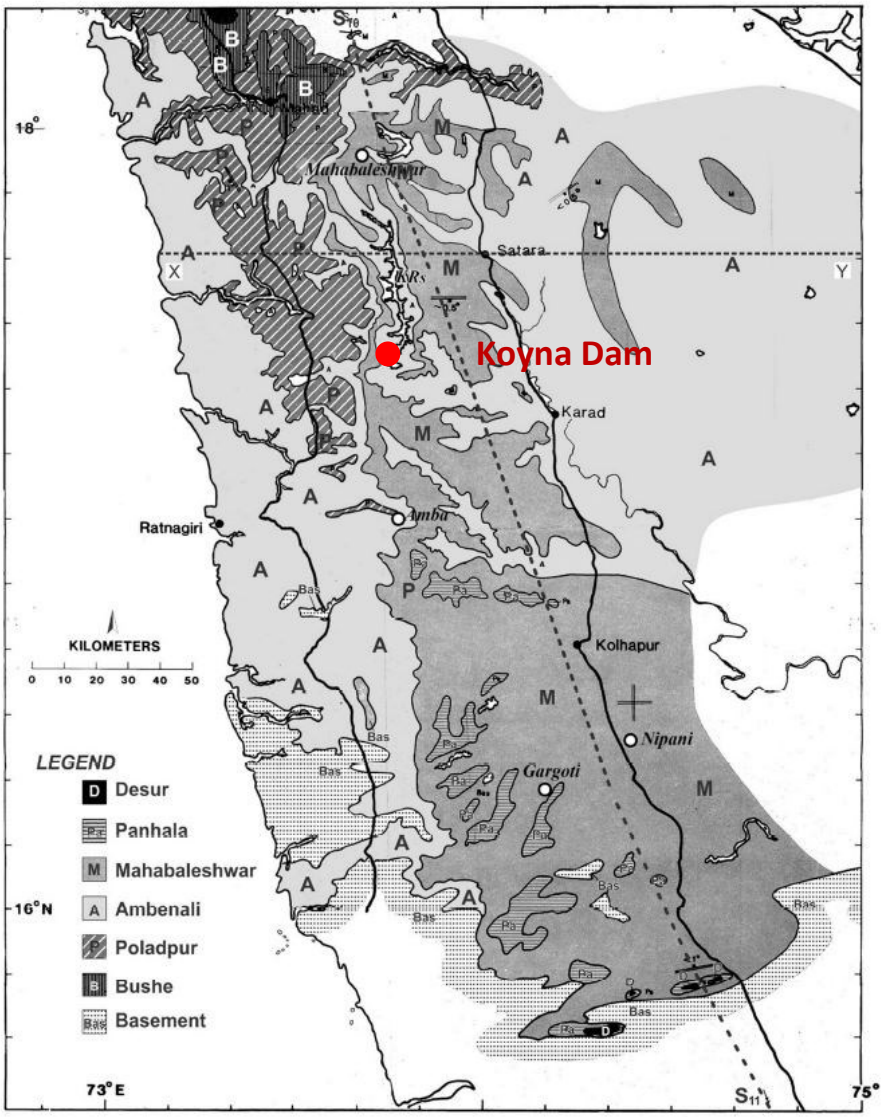

Figure 3.8a. Geological sketch map of the southern part of the Deccan volcanic province (Beane et al., 1986; Devey and Lightfoot, 1986; Mitchell and Cox, 1988; Subbarao and Hooper, 1988) (figure from Subbarao and Courtillot, 2017).

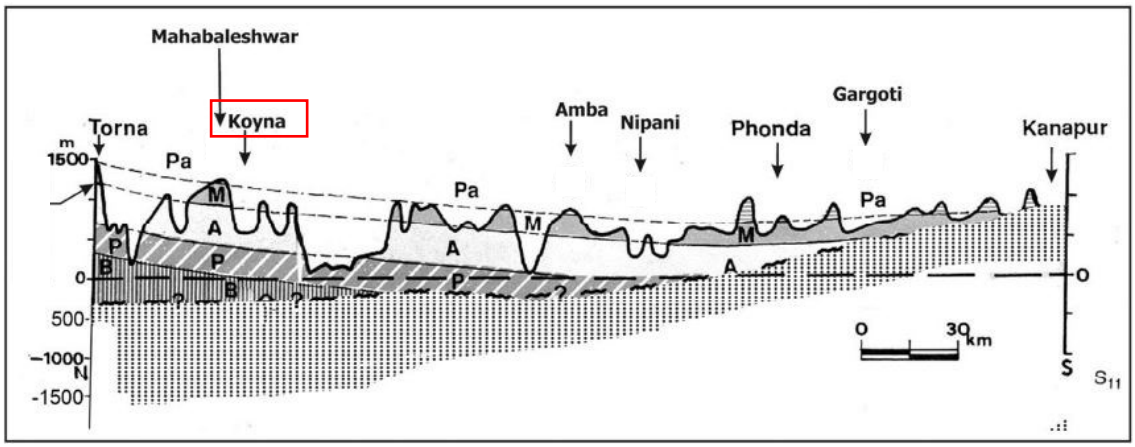

Figure 3.8 (b). N-S cross section (N to the left, see Fig. 3.8a; S10-S11) in the Koyna rea showing the Deccan Traps structure (see Fig 3.8a for legend). M, A and P correspond to the Mahabaleshwar, Ambenali and Poladpur formations of the Wai Subgroup, respectively, and B to the Bushe Fm. of the Khandala subgroup. In this area, the thickness of the Deccan Traps reduces towards the south (figure from Subbarao and Courtillot, 2017).

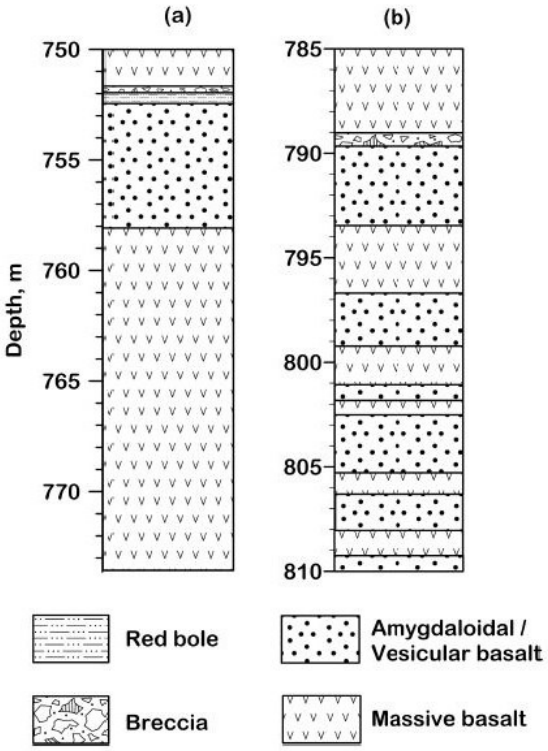

Figure 3.9. Lithology of **(a)** typical simple flow (751.67-773.63 m), and **(b)** 25 m section (785-810 m) of a 50.91 m thick compound flow showing multiple flow units from the KBH7 (figure from Mishra et al., 2017).

The Deccan Traps are subdivided into three subgroups and ten formations based on their field characteristics and chemical and isotopic composition (Beane et al., 1986) (Table 2.1).

The three subgroups are from the bottom to the top (Beane et al., 1986):

- Kalsubai Subgroup: comprises the five lowest formations with a minimum thickness north of the DVP of 2000 m. All five formations are characterised by amygdaloid flows; picrite (>10% MgO) is relatively common and contains olivine and/or clinopyroxene phenocrysts. Abundant, small plagioclase phenocrysts are typical only in the upper formation. A peculiarity of this subgroup is that the primitive flows of the lower formations are separated by flows containing giant plagioclase phenocrysts (2-5 cm long), called giant plagioclase basalts (GPB). They are the most chemically evolved flows of the Western Ghats.
- Lonavala Subgroup: composed of the Khandala and Bushe Formation, with a maximum thickness of 525 m. The former is characterised by simple flows, while both have high Ba/Ti and Ba/Sr and low MgO content. The Bushe, on the other hand, is composed of coarse-grained, aphyritic and amygdaloid composite flows,

which are generally indistinguishable and have a greatly reduced abundance range for most elements.

- Wai Subgroup: comprises the upper part of the stratigraphic succession of the DVP and includes the Poladpur, Ambenali and Mahabaleshwar formations. The total thickness is around 1000 m at Mahabaleshwar, but towards the south the last formation is thicker. The formations that make up this subgroup are characterised by simple flows with minor compound flows. These three formations appear more evolved than those of the other subgroups.

(b)	Subgroup	Formation	Member / Flow	Thickness M	Polarity
DECCAN BASALT GROUP	Wai	Desur			N
		Panhala		>175	
		Mahabaleshwar		280	
		Ambenali		500	
		Poladpur		375	
	LONAVALA	Bushe		325	
		Khandala		145	
	Kalsubai	Bhimashankar	Monkey Hill GPB Giravili GPB	140	R
		Thakurvadi	Manchar GPB	650	
		Neral	Tunnel-5 GPB	100	
		Igatpuri	Kashele GPB	> 500	
		Jawhar	Thalghat GPB	> 200	

Table 2.1. Simplified stratigraphic column of the Deccan Basalt Group in the Western Ghats, showing the position of the giant plagioclase basalts (GPBs) at the top of each Formation in the Kalsubai Subgroup (Beane et al., 1986; Devey and Lightfoot, 1986; Subbarao and Hooper, 1988) (from Subbarao and Courtillot, 2017).

In the Koyna-Warna area are present only the Wai Subgroup and the uppermost formation of the Lonavala Supergroup (i.e., Bushe Fm., Figure 3.8b; Table 2.1). The lava flows are either composed or simple, the latter being the most common and include 64% of pahoehoe and coarse pahoehoe, 29% only pahoehoe and 2% aa-type (Mishra et al., 2017; Duraiswami, 2017). In detail, starting from the oldest rocks (Beane et al., 1986):

- Bushe Formation: topmost formation of the Lonavala Subgroup made of coarse-grained, altered and amygdaloid, aphyric compound basaltic flow with sparse

plagioclase. The basalts have a high Sr ratio compared to other formations and therefore to be contaminated by the granitic crust.

- Poladpur Formation: is at the base of the Wai subgroup and made of lava flows. The lava flows are vesicular with an oxidised top; the grain size of the phenocrysts of plagioclase, plagioclase + augite or plagioclase + augite + olivine ranges from fine to coarse. The Ba and Sr concentration is high, while the Mg content is low like the rest of the subgroup.
- Ambenali Formation: is part of the Wai subgroup, about 400 m thick and consists of simple basaltic flows. The concentration of LIL is low and so is the Sr ratio. It is assumed that these basalts underwent minor contamination from the continental crust (Sano et al., 2001).
- Mahabaleshwar Formation: is youngest Fm. of the Wai subgroup cropping out in the area and composed of only two lava flows; Ba and Sr (LIL) content is higher than that of the Ambenali.

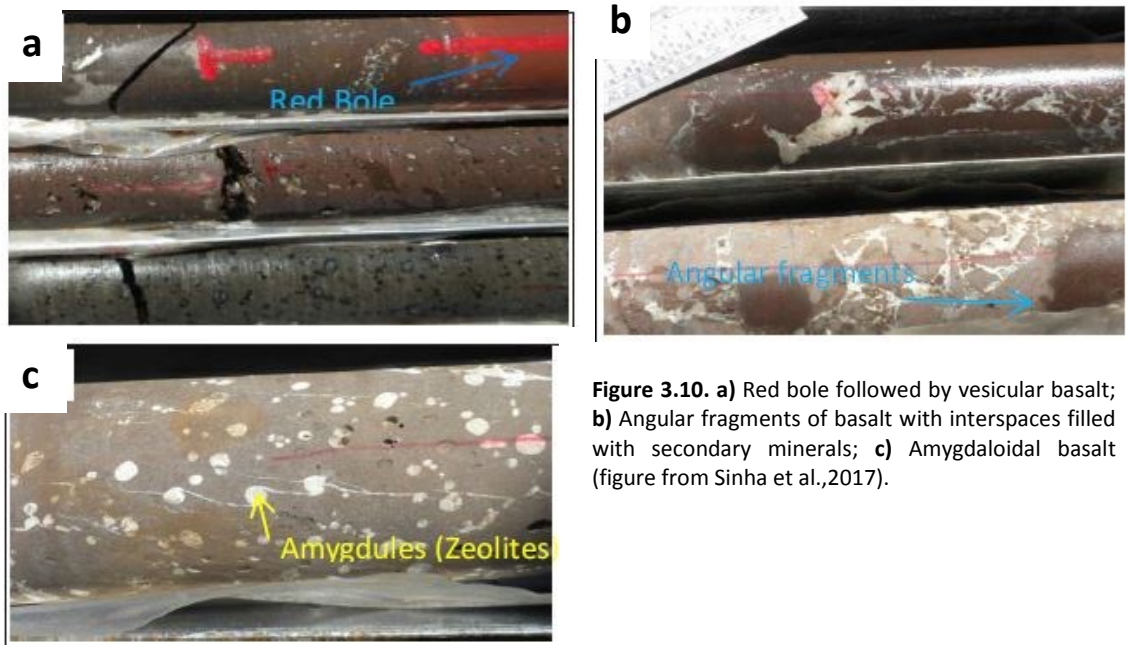

Figure 3.10. a) Red bole followed by vesicular basalt; **b)** Angular fragments of basalt with interspaces filled with secondary minerals; **c)** Amygdaloidal basalt (figure from Sinha et al.,2017).

3.3. Structural Features from Drilling Cores

The samples from the boreholes KBH1, KBH6 and KBH7 show macroscopically a dense network of fractures cutting at 75°-85° with respect to the well vertical axis the granitic-gneissic basement (Misra et al., 2017) (Figures 3.5 c-d, 3.11). The fact that the boreholes (vertical) passed through sub-vertical fractures and faults is indicative that the latter are abundant in the area. Fractures are interconnected and form an anastomosing network, which may facilitate fluid flow at depth (Misra et al 2022). Since the strike of faults/fractures tends to be sub-parallel with the WG escarpment, these could have formed at the same time. The faults are filled by quartz, chlorite, epidote and calcite. Crosscutting relations between fractures and their mineral filling allowed me to reconstruct the sequence of deformation events as I will discuss in Chapter 6.2. Less abundant are the fractures cutting the basaltic flows, which are sub-horizontal and more often oblique (45° to the core axis) to sub-vertical (0°-15° to the core axis) (Sinha et al., 2017). Fractures in basalts are often related to lava cooling and are filled by quartz, zeolite, calcite and occasionally chlorite veins (Sinha et al., 2017). Fractures and fissures are more abundant approaching the Donichawadi fault; here the basalt, which is highly weathered, is cut by sub-vertical fractures striking between N30°W and N50°E (Goswami et al., 2020). They are filled by secondary phases, as fissures are preferential pathways for water percolation (Misra et al, 2017). Regarding the fracture density in the boreholes, the highest concentration of fractures in KBH-1 is between 940-1075 m and 1142-1238 m borehole depth (Misra et al., 2017). The abundant presence of fractures and faults, especially in the two zones above, is evident from the low Rock Quality Designation (RQD) values (Misra et al., 2017) (Figure 3.12). The RQD represents the percentage of intact core > 10 cm in length and provides a good measure of the overall quality of the recovered core (Deere, 1963). Regarding KBH-6, the granitoid has large RQD at 904.42-973.75 m, 981.85-1148.60 m, 1248.34-1307.40 m and 1358.78-1472.45 m depth. Finally, the KBH-7 core are less fractured, although there are limited volumes with high RQD at 1253.43-1289.91 m, 1331.67-1370.95 m and 1478.15-1491.80 m depth. These volumes with large RQD index correspond to volumes with higher porosity, up to 33 %, while in basement rocks from the same area is 0.1-1% (Goswami et al., 2019) (see chapter 5.2).

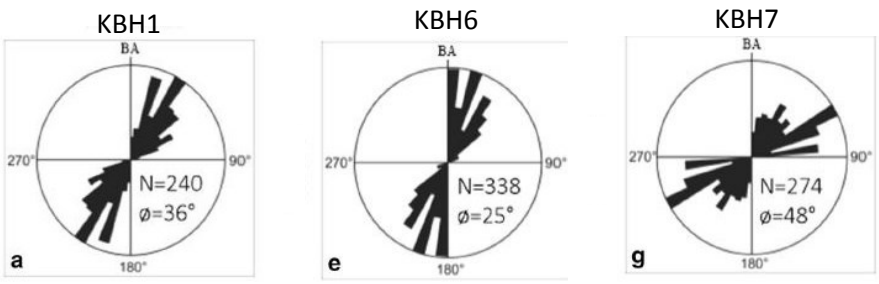

Figure 3.11. Rose diagrams representing the distribution of angles of fractures measured with respect to the vertical borehole axis (BA) in KBH-1, KBH-6 and KBH-7. N is the number of data and Φ is the mean resultant dip angle of planar features measured with respect to the Borehole Axis (BA) (capture and image taken from Misra et al., 2022).

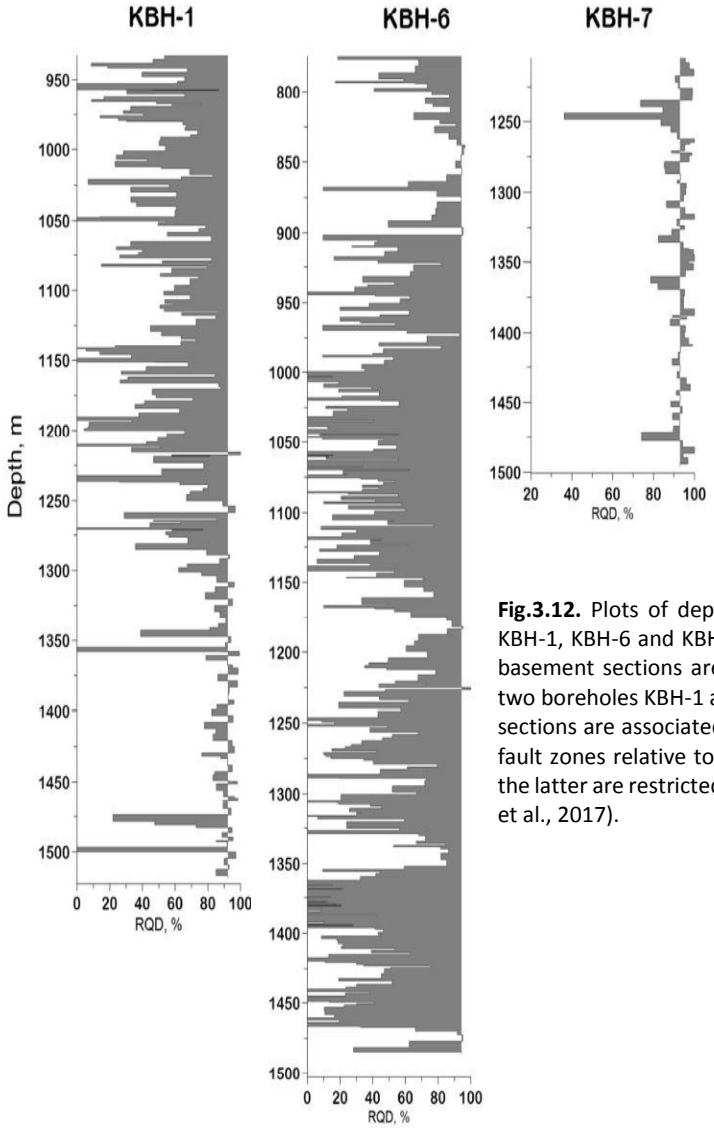

Fig.3.12. Plots of depth vs. RQD (%) in the three boreholes KBH-1, KBH-6 and KBH-7. Fault and fracture zones within the basement sections are associated with low RQD values. The two boreholes KBH-1 and KBH-6 showing poor RQD over large sections are associated with higher frequency of fracture and fault zones relative to KBH-7. The fault and fracture zones in the latter are restricted to localized sections (figure from Misra et al., 2017).

4. Materials and Methods

4.1. Materials

The thesis is focused on rock samples from three (KBH1, KBH6 and KBH7) of the nine deep boreholes of the International Continental Drilling Project (ICDP) of Koyna, India (Figure 2.13). Thanks to a scientific collaboration with Dr. Sukanta Roy, Head of the Borehole Geophysics Research Laboratory in Karad, Dr. Elena Spagnuolo (Istituto Nazionale di Geofisica e Vulcanologia, Rome) and Giulio Di Toro, visited in 2019 the borehole repository of Karad, which houses all the cores of the ICDP of Koyna for a total length of approximately 17 km, and selected 17 samples (Table 4.1). The main scientific topic is the understanding of the faults/fractures reactivated by the human-induced seismicity of Koyna-Warna areas.

4.2. Samples Analysis

All fault rock samples were prepared (including in some cases consolidation with epoxy) and analysed in the Department of Geosciences, University of Padua. Parts of the specimens were ground to make powders and the other parts cut and polished, also with Syton®, to obtain thin sections of 30 µm thickness. The samples were cut orthogonal to the fracture surface. All thin sections were scanned at high resolution under both parallel and cross Nicols. The Syton® ultrapolished thin sections were immersed in an ultrasonic bath with methanol to eliminate the micro-powders used for polishing and then covered with coating film of carbon.

Sample No.	Borehole	Box No.	Section	From (m)	To (m)	Length (cm)	Sample Designations
1	KBH1	250	4	1039.85	1039.91	6	KBH1_346
2	KBH1	254	3	1057.42	1057.53	11	KBH1_347
3	KBH1	256	5	1069.50	1069.57	7	KBH1_348
4	KBH1	257	5	1073.95	1073.98	3	KBH1_349
5	KBH1	274	4	1153.69	1153.78	9	KBH1_350
6	KBH1	287	2	1211.40	1211.43	3	KBH1_351
7	KBH1	327	3	1404.89	1404.94	5	KBH1_352
8	KBH1	343	3	1483.10	1483.14	4	KBH1_353

Sample No.	Borehole	Box No.	Section	From (m)	To (m)	Length (cm)	Sample Designations
1	KBH6	365	1	1470.48	1470.52	6	KBH6_67
2	KBH6	365	1	1470.58	1470.62	4	KBH6_68
3	KBH6	365	1	1470.27	1470.32	5	KBH6_69
4	KBH6	365	1	1470.56	1470.59	3	KBH6_70
5	KBH6	364	5	1469.85	1469.89	4	KBH6_71
6	KBH6	364	5	1469.6	1469.65	5	KBH6_72
7	KBH6	364	1	1465.07	1465.12	5	KBH6_73

Sample No.	Borehole	Box No.	Section	From (m)	To (m)	Length (cm)	Sample Designations
1	KBH7	368	1	1476.59	1476.66	7	KBH7_594
2	KBH7	368	4	1479.47	1479.52	5	KBH7_595

Table 4.1. List of the seventeen thesis samples with their respective depths.

4.2.1. Optical Microscope

The microstructural study was carried out with the OLYMPUS BH-2 optical microscope, in the Microscopy Laboratory, at parallel and crossed Nicols using 4x, 10x, 20x and 40x objectives. Afterwards I took microphotos using the CANON EOS 650D camera installed on the Nikon ECLIPSE ME600 microscope.

4.2.2. X-ray powder diffraction (XRPD)

The mineralogy of fault rocks was determined with semi-quantitative X-ray powder diffraction (XRPD) analysis. The samples were first grounded with a mechanical mullion with an agate mortar and then again manually with a second agate mortar to obtain powders with grain size below 2 μm. Then the powders were analyzed (X-ray diffraction) at room temperature with an X'Pert PRO MPD (PANalytical) instrument in Bragg–Brentano geometry with iron-filtered Co-Kα radiation (40 kV, 40 mA, λ = 0.1789 nm), equipped with an X'Celerator detector. The powders were placed onto a rotating metal slide; the angular range was set as 2θ = 3-85°, with a step size of 0.017° and scan speed of 0.0061° s^{-1}. The identification of the crystalline phases was obtained using the X'Pert High Score Plus software, which includes PDF-2, Pan-ICSD and COD (Crystallography Open Database) databases.

4.2.3. Field Emission Gun Scanning Electron Microscope (FEG-SEM)

The TESCAN SOLARIS Field Emission Gun Scanning Electron Microscope (FEG-SEM) for high-resolution microstructural and microanalytical investigations (Figure 4.1). The following techniques were used with the TESCAN SOLARIS:

- Collection of Back-Scattered Electrons (BSE) images with the in-beam mid-angle-BSE detector, operating at an accelerating voltage of 5 kV, beam current of 300 pA.

- Semi-quantitative (EDS) though calibrated chemical analyses and maps with Oxford Instrument Ultime Max 65 SDD, operating at an accelerating voltage of 15 kV, beam current of 15 nA, timing each analysis 40 s, using a 1-μm beam.

Natural minerals (Amelia's albite for Si and Al, diopside for Ca, San Carlos' olivine for Mg) and pure oxides (for Fe, Mnand Ti) were used as standards. The AZtec® program was used to convert X-ray counts into weight percent oxides. PAP corrections were applied to correct matrix effects.

- Quantitative chemical analyses of chlorites with Oxford Instrument Wave 700 WDS spectrometer with 5 diffracting crystals (LSM200, LSM80N, TAP, PET, LIF), operating at an accelerating voltage of 15 kV, beam current of 15 nA, counting time of 15 s for Si and Fe peaks and 15 s for background, counting time of 10 s for Mg, Al, Mn and Ti peaks and 10 s for background, using a 1-µm beam. The analyses on saponite grains were replicated using a lower beam current (10 nA) and a defocused beam (5 lm) to minimize interlayer cation loss. Natural minerals (Amelia's albite for Si and Al, diopside for Ca, San Carlos' olivine for Mg) and pure oxides (for, Fe, and MnTi) were used as standards. The AZtec® program was used to convert X-ray counts into weight percent oxides. PAP corrections were applied to correct matrix effects.

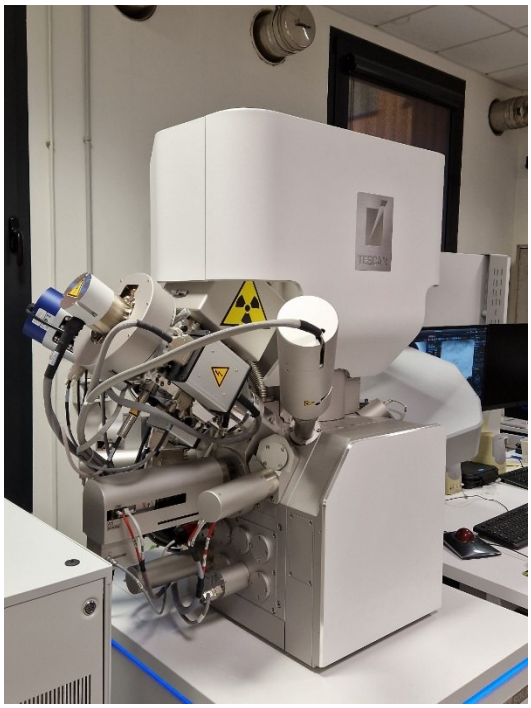

Figure 4.1 TESCAN SOLARIS Field Emission Gun Scanning Electron Microscope (FEG-SEM) installed at the Department of Geosciences, Padua, Italy.

5. Results

The 17 studies samples (Table 4.1, see in Appendix 1) are from boreholes KBH-1, KBH-6 and KBH-7 located east of the Western Ghat escarpment and around the Koyna-Warna seismic region (Figure 1.1). Misra et al, (2022) used SQD (Sample Quality Designation), a classifier identical to the RQD (Chapter 3.3), to divide the cores into four categories:

- A for cores more than 50 cm long,
- B between 25-49 cm long,
- C between 5-24 cm long and
- D less than 5 cm long.

Fracture density increases from category A to D. Categories C and D include highly fractured fault rocks and all the samples in this thesis belong to them.

Here, I first summarize the main rock-forming minerals of all the samples based on XRPD semi-quantitative analysis. Then, I describe the main microstructural features of the samples from OM and FEG-SEM investigations, and eventually I present the chemical composition of the chlorites obtained with the FEG-SEM WDS for geothermometer applications (Chapter 6.1).

5.1. Mineralogical Composition (XRPD analysis)

All XRPD data are reported in Table 5.1 and Figure 5.0, while all the XRPD spectra in Appendix 2. I present here the most significant data for basement and fault rocks, the latter distinguished breccias and cataclasites and faults and fractures filled by chlorite, epidote and calcite veins (see section 5.2.2 definitions and microstructural description).

Sample	Qtz	Cc	Chl	Kfs	Pl	Ep	Px	Ms	An	Zeo	Tit	Goe	Tl	Rock type
KBH1-346	6	78	4	7	5									Fault calcite-bearing vein
KBH1-347	7	76	2		12		2							Fault calcite-bearing vein
KBH1-349	1	1	37		51	5		3	1					Fault chlorite-bearing vein
KBH1-350	2	86	4		7									Fault calcite-bearing vein
KBH1-351	50	10	34						1	2				Fault chlorite-bearing vein
KBH1-352	25			4	26	42				3				Fault epidote-bearing vein
KBH6-73	19		15	12	54									Granodioritic basement
KBH6-72	88	8	10								1			Fault/ fracture quartz-bearing vein
KBH6-71	64	1	31								4			Fault/ fracture quartz-bearing vein
KBH6-69	43		51								5	1		Fault/ fracture chorite-beraing vein
KBH6-67	32	2	36		4	20					4	1		Fault/ fracture chorite-beraing vein
KBH6-70	18	1	23	10	23	25	1							Green-schist
KBH6-68	29	3	32	10		20					4	1		Green-schist
KBH7-594	15	56	27											Fault/ fracture calcite-bearing vein
KBH7-595	52	9	33								2		5	Fault/ fracture chorite-beraing vein

Table 5.1. XRPD semi-quantitative analysis. Mineral composition in wt. %: Qtz (quartz), Cc (calcite), Chl (chlorite), Kfs (K-feldspar), Pl (Plagioclase), Ep (Epidote), Px (Pyroxene), Ms (Muscovite), An (Anatasio), Zeo (Zeolite), Tit (Titanite), Goe (Goethite) and Tl (Talc).

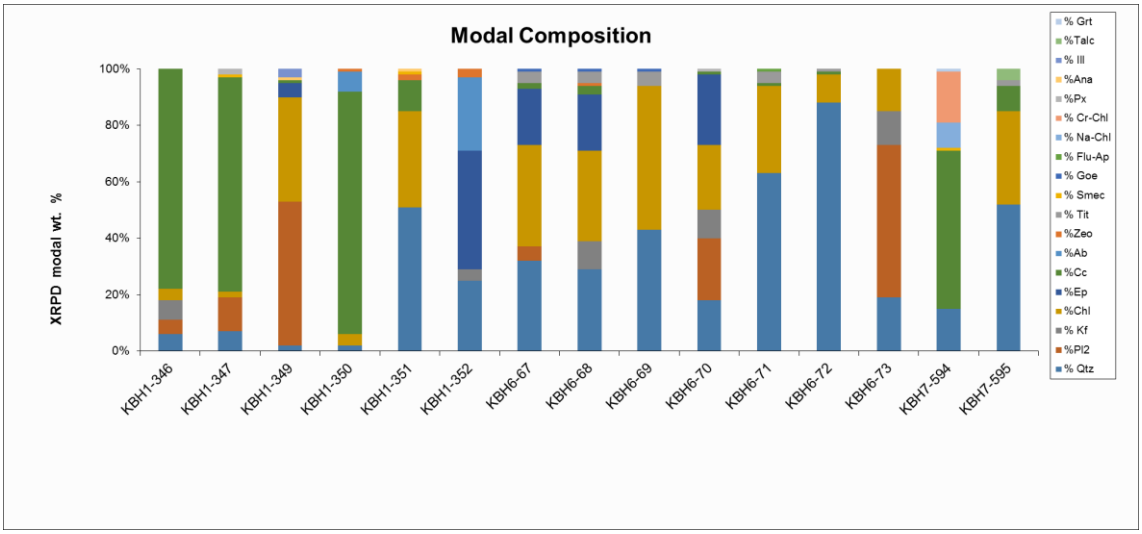

Figure 5.0. Modal semi-quantitative composition of the samples of samples used with XRPD method

5.1.1. Basement rocks

Crystalline basement of the Koyna-Warna region includes granites, tonalites, granodiorites and monzogranodiorites (Bhaskar Rao, 2017) (Figures 3.5a to e). Instead, amphibolites are abundant especially in KBH6 (Misra et al., 2017) (Figure 3.5 e, f). I analyzed the following basement rock samples:

KBH6-73 (1465.07 m depth)

KBH6-70 (1470. 56 m depth)

KBH1-346 (1039.85 m depth)

KBH1-347 (1057.42 m depth)

KBH1-348 (1069.50 m depth)

KBH1-350 (1153.69 m depth)

Sample KBH-73 has percentages of the mineralogical phases typical of a granitic basement rock (wt. %): plagioclase 54, quartz 19, chlorite 15, K-feldspar (possible microcline) 12 (Figures 5.0 and 5.1) (Table 5.1). The mineral composition corresponds to the one of a granodiorite in the QAPF diagram (Figure 5.2). The presence of chlorite

indicates the occurrence of alteration, possibly under green-schist to sub-greenschist facies conditions (see WDS analysis and discussion).

Samples KBH1-346, 347, 348 and 350 have a typical granodiorite composition (Table 5.1). Secondary minerals include hornblende, chlorite and epidote and accessory minerals are titanite, anatase, zircon and apatite.

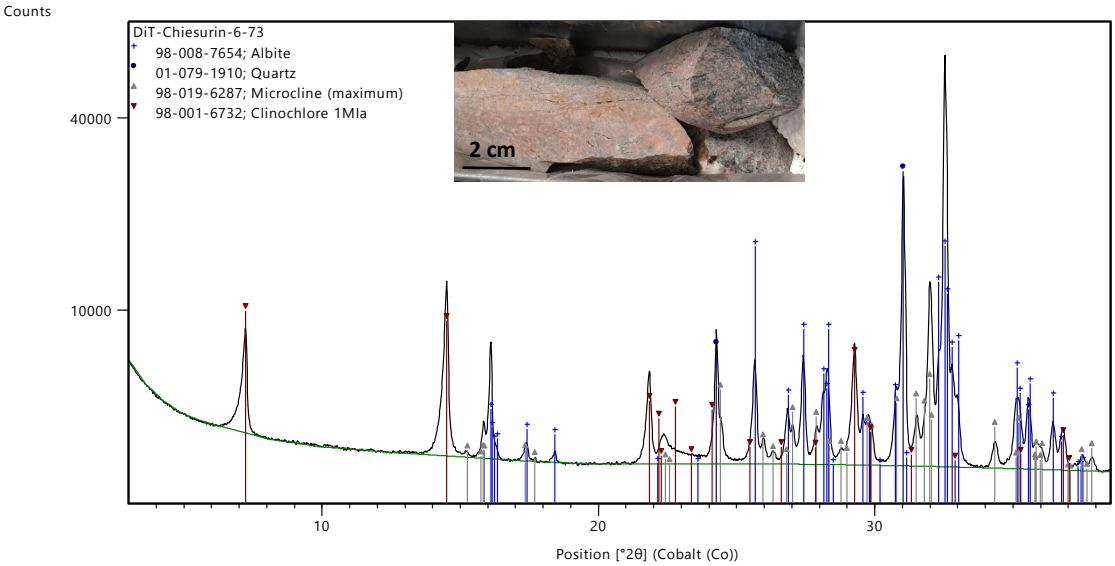

Figure 5.1 Powder diffractogram of sample KBH6-73

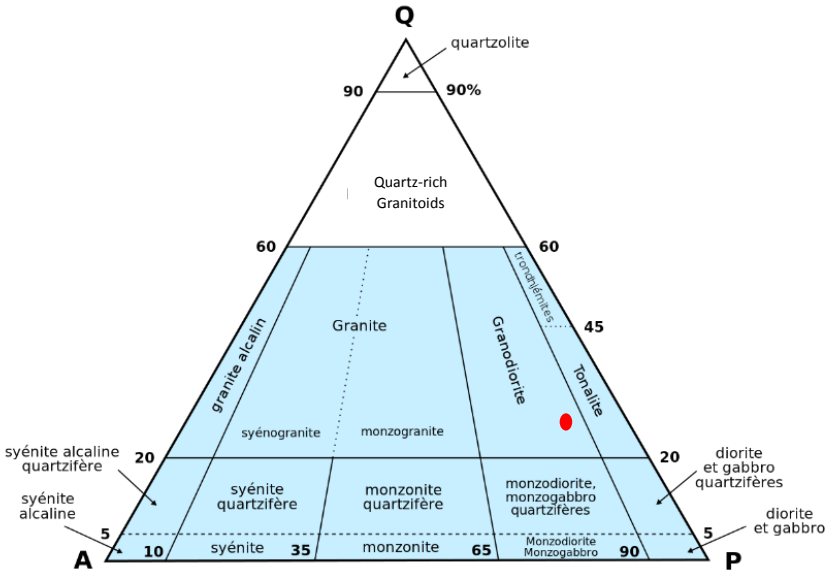

Figure 5.2. QAP diagram for granitic rocks. The red dot indicates the composition of sample KBH6-73. The composition of the Koyna's basement in this borehole is granodioritic.

Instead, some basement rocks are altered under green-schist facies and are interpreted as former amphibolites (Misra et al., 2017, see Figure3.5f and Appendix 1) as they include large amounts of chlorite and epidote, up to 51% and 25% (Table 5.1).

Sample KBH6-70 has moslty mineral assemblages typical of green-schist facies rock (wt. %): epidote 25, clorite 23, plagioclase 23, quartz 18, K-feldspar 10, pyroxene 1, calcite 1 (Figures 5.0 and 5.3).

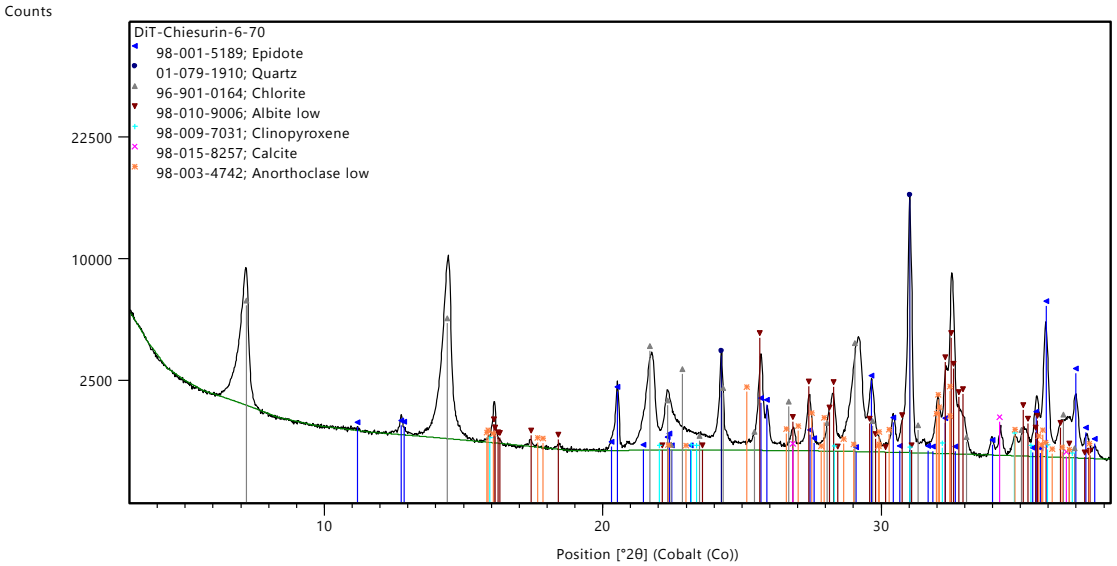

Figure 5.3 Powder diffractogram of sample KBH6-70.

5.1.2. Fault rocks

The Koyna samples are often faulted and fractured and their filling includes chlorite, epidote, calcite and, to a less extent, quartz veins. I analyzed the following samples:

KBH1-346 (1039.85 m depth)

KBH1-352 (1404.89 m depth)

KBH6-72 (1469.60 m depth)

KBH6-69 (1470.27 m depth)

KBH7-594 (1476.59 m depth)

Faults and fractures filled by chlorite veins

These are faults and fractures filled with chlorite. Sample KBH6-69 has the following wt.% in oxides: chlorite 51, quartz 43, titanite 5, goethite 1 (Figures 5.0 and 5.4, see Appendix 1). Sample KBH6-67, collected near to KBH6-69, has a similar composition. Secondary minerals include plagioclase and K-feldspar and the accessory minerals are titanite, goethite and apatite.

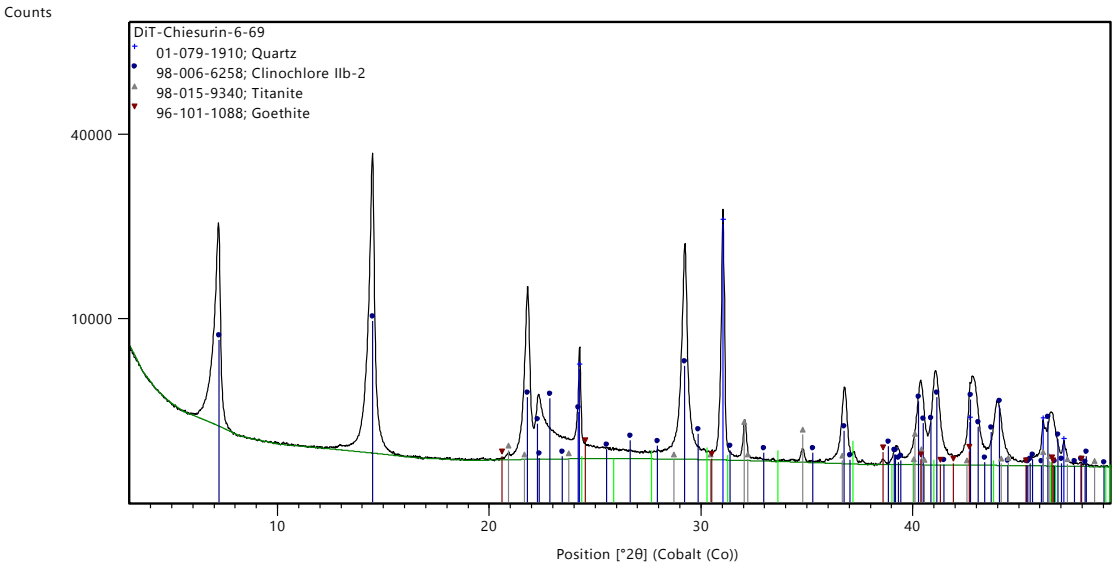

Figure 5.4 Powder diffractogram of sample KBH6-69.

Faults and fractures filled by epidote veins

Other types of faults and fracture bearing veins are those filled only by epidote, as in sample KBH1-352 (Figures 5.0and 5.5). Epidote, albite and quartz are the most abundant phases, while K-feldspar occurs as secondary phase (wt.%): epidote 42, albite 26, quartz 25, K-feldspar 4, zeolite (possible phillipsite) 3 and smectite (possible montmorillonite) < 1 (Figures 5.0 and 5.6).

Figure 5.5. Sample KBH1-352 showing a fault/fracture filled by epidote vein cutting through the granite basement.

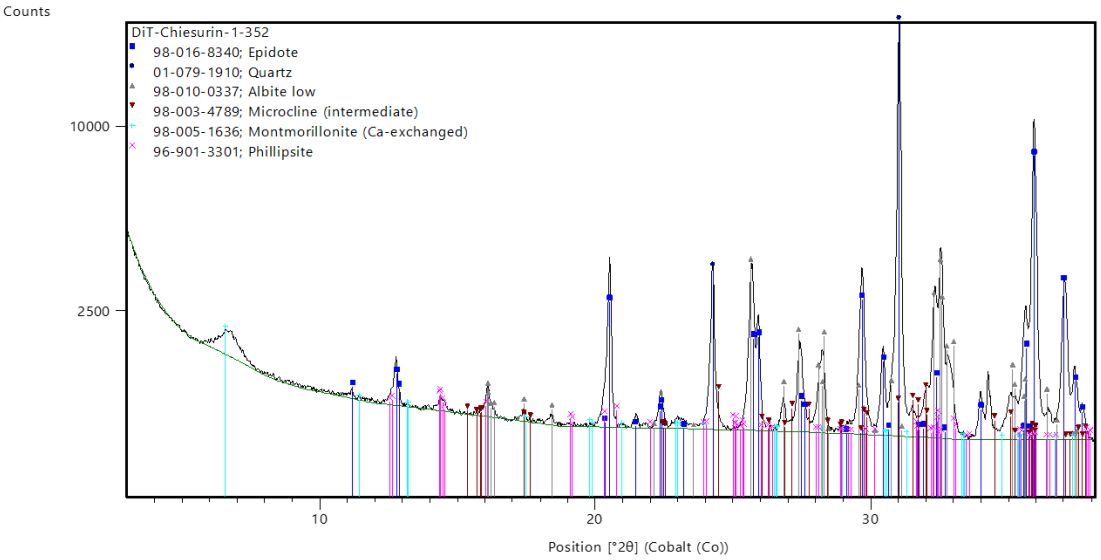

Figure 5.6 Powder diffractogram of sample KBH1-352 (fault/fracture filled by epidote vein).

Faults and fractures filled by quartz veins

Dense networks of faults/fractures sealed by quartz veins were recovered from borehole KBH6 (samples KBH6-71 and 72, Figure 5.7). The composition of these samples in wt.% is (KBH6-72): quartz 88, chlorite 10, calcite 1, titanite 1 (Figure 5.8).

Figure 5.7. Core sample from Karad repository with the dense network of quartz sealed by quartz veins.

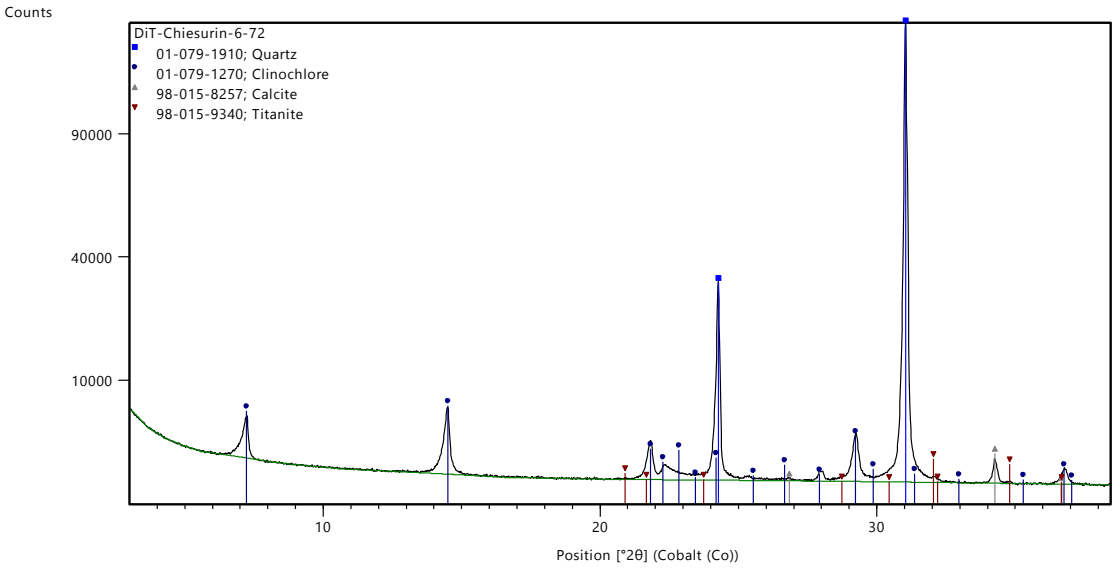

Figure 5.8. Powder diffractogram of sample KBH6-72.

Faults and fractures filled by calcite veins

Calcite-bearing veins are present in most of the studied samples. Figure 5.9 shows a white calcite patina overprinting a chlorite-filled fracture. The percentage composition of the calcite-bearing vein (wt. %) is (KBH1-346): calcite 78, K-feldspar 7, quartz 6, plagioclase 5 and chlorite 4 (Figure 5.10). With the exception of calcite, which is the vein filling, the other minerals are in fragments from the granodioritic basement distributed in the vein (see microstructural description below).

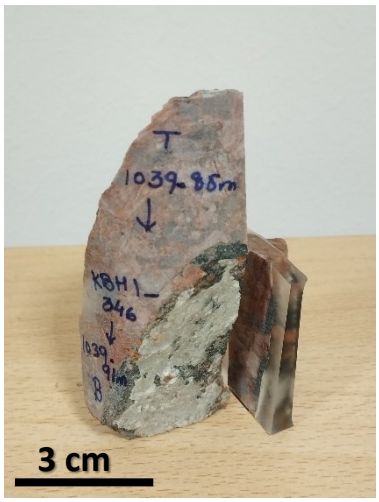

Figure 5.9. Sample KBH1-346 where the subvertical fault is filled by a dark green in color chlorite vein and cut by a whitish calcite-bearing vein.

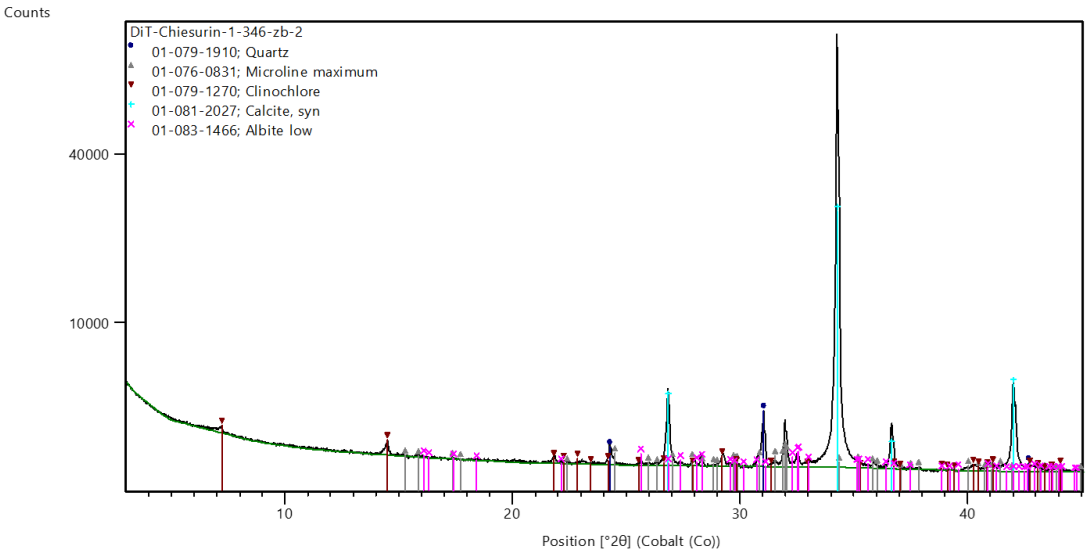

Figure 5.10. Powder diffractogram of sample KBH1-346.

Another example of a calcite-rich vein is from borehole KBH7 (sample KBH7-594) at the contact between a dyke of the Deccan Traps with the Archean basement (Figure 3.5g). The mineralogical semi-quantitative analysis includes (wt. %): calcite 56, Cr-chlorite 18, quartz 15, Na-chlorite (possible glagolevite) 9, garnet (possible uvarovite) 1, smectite (possible montmorillonite or corrensite) 1 and zeolite (possible laumontite) < 1 (Figure 5.11).

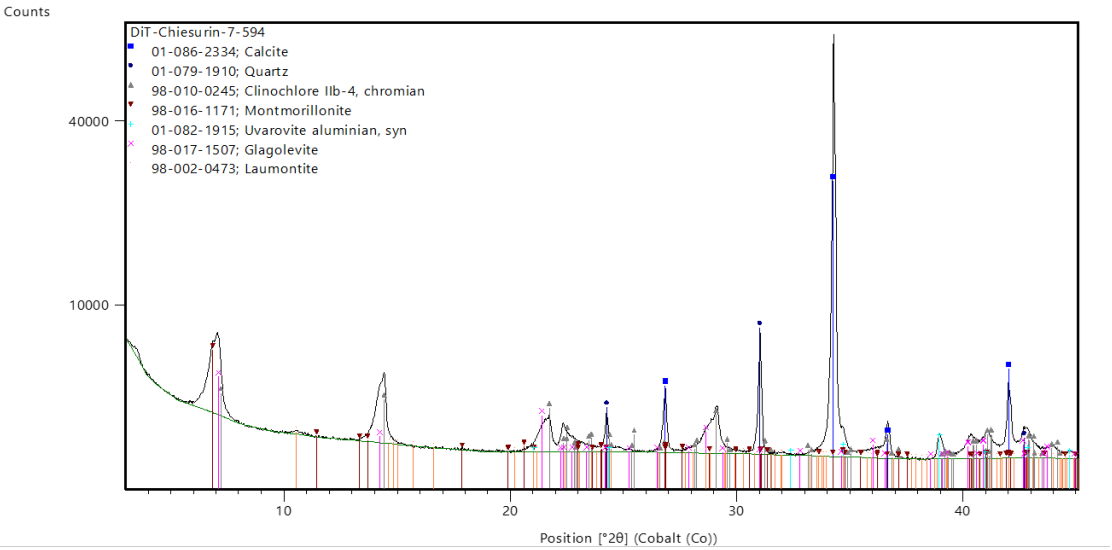

Figure 5.11. Powder diffractogram of sample KBH7-594.

5.2. Microstructural observations

The microstructures were studied under the optical (OM) and field emission scanning electron microscope (FEG-SEM). Table 5.2 summarizes the seventeen samples studied with the type of fault rock and main characteristics. Microstructures are grouped in basement rocks, mylonites, breccia & cataclasites and faults and fractures filled by veins. Note that some samples may be contaminated by drilling muds which transport and redeposit wall rock fragments (KBH6-67, Figure 5.12).

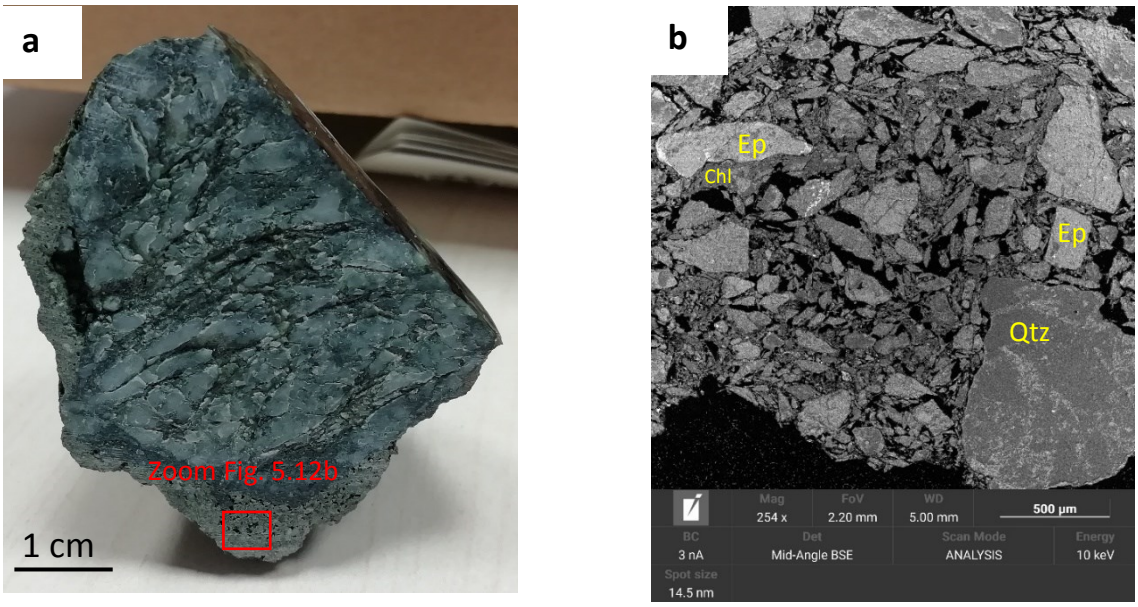

Figures. 5.12. Core sample KBH6-67 of breccia and cataclasite with chlorite matrix. **a)** Bottom: consolidated drilling muds; **b)** FEG-SEM image of the drilling muds with cuttings which include clasts made of epidote, chlorite and quartz.

SAMPLE	FAULT ROCK TYPE AND MAIN CHARACTERISTICS
KBH1_346	Breccia & cataclasite with chlorite matrix cut by subvertical fault/ fracture filled by calcite vein, fault/ fracture epidote-bearing vein
KBH1_347	Breccia & cataclasite with calcite matrix, fault/ fracture filled by epidote vein
KBH1_348	Fault/ fracture filled by chlorite vein
KBH1_349	Fault/ fracture filled by chlorite vein
KBH1_350	Breccia & cataclasite with chlorite matrix cut by subvertical fault/ fracture filled by calcite vein
KBH1_351	Mylonitic block incorporated in a Fault/ fracture filled by chlorite vein
KBH1_352	Fault/ fracture filled by epidote vein
KBH1_353	Breccia & cataclasite with epidote matrix truncate by fault/ fracture filled by epidote and calcite veins
KBH6_67	Breccia & cataclasite with chlorite matrix, fault/ fracture chlorite-bearing vein
KBH6_68	Fault/ fracture filled by chlorite vein (very disturbed by drilling mud)
KBH6_69	Fault/ fracture filled by chlorite vein
KBH6_70	Amphibolitic basement cut by fault/ fracture quartz-, chlorite- and calcite-bearing veins
KBH6_71	Fault/ fracture filled by quartz, chlorite and calcite veins
KBH6_72	Fault/ fracture filled by quartz, chlorite and calcite veins
KBH6_73	Granodioritic basement
KBH7_594	Fault/ fracture calcite-bearing veins (Growth fibers at the basaltic dyke-basement contact)
KBH7_595	Breccia & cataclasite with chlorite matrix, Fault/ fracture filled by chlorite and calcite veins

Tab 5.2. Type of fault rock and main characteristics of each sample.

5.2.2. Basement Rocks

The studied samples are those presented in section 5.1.1. and are from KBH1 and KBH6. These rocks are cut by sub-vertical faults and fractures which allowed fluids percolation and precipitation of secondary phases (see next section).

In basement rocks, the magmatic texture of the granite is hypidiomorphic as the plagioclase and K-feldspar have prismatic to subhedral habit, while quartz has an anhedral habit (Figure 5.13a). The grain size is coarse (10 mm in average, KBH1-346) and medium/fine at greater depth (2-3 mm in average, KBH1-347, -348, -350). The rock forming minerals record high temperature (late-magmatic) to low temperature (mainly green-schist facies) deformation and alteration features. In particular:

Quartz grains show in some cases (sample KBH1-347) chessboard extinction (Mainprace & Nicolas, 1989; Stripp et al., 2002; Kruhl, 1996) (Figure 5.13b). This peculiar feature is associated with high-temperature deformation (Passchier & Trouw, Microtectonics, 2005). Both high and low temperature recrystallization by grain boundary migration is present (Figure 5.13c). Low temperature wavy extinction is common;

K-feldspar has strong intracrystalline deformation including intra-granular faults, twins and flame-like structures (sample KBH1-346, Fig. 5.9), indicating high differential stress (Passchier, 1892) (Figure 5.13d). Probably, in view of the lattice-like extinction of crossed Nicols, the K-feldspar is a microcline;

Plagioclase is rich in fluid inclusions, altered (sericification), and has albite gemination possibly indicative of deformation at high differential stress at low-medium grade conditions (400-500°C) (Passchier & Trouw, 2005) (Figure5.13e);

Mafic minerals. Often (e.g., sample KBH1-347) the only mafic mineral is hornblende (confirmed by EDS-WDS-FEGSEM analysis), locally substituted by chlorite (Figure 5.13f). In fact, chloritization of mafic minerals (biotite, amphibole) is widespread in most of the studied basement samples. This would be consistent with the green-schist facies conditions metamorphism of the basement rocks (300-450°C and 0.1-0.4 GPa).

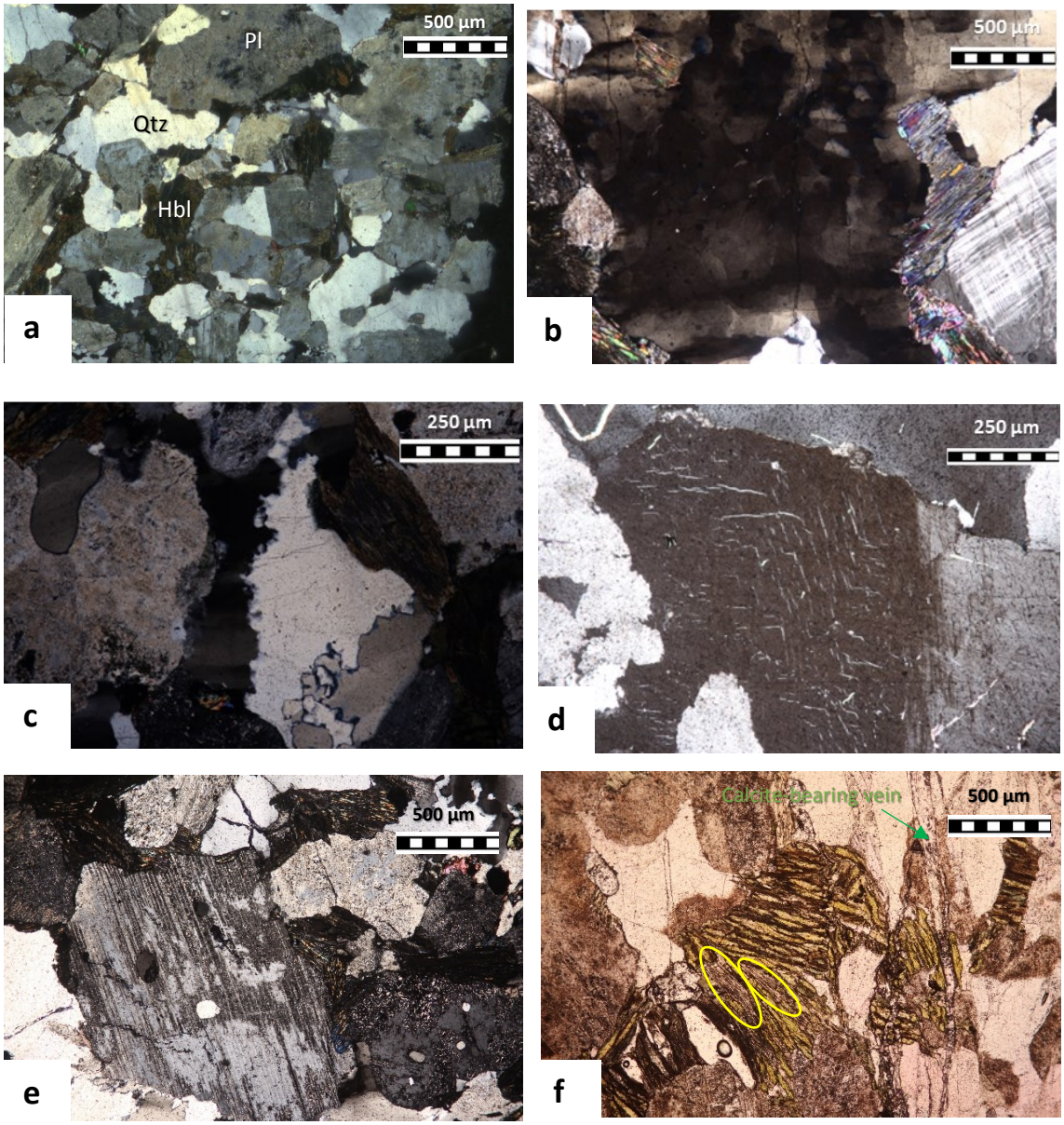

Figure 5.13. Microstructures in Proterozoic basement rocks: **a)** hypidiomorphic texture of the granodioritic basement from sample KBH-350; **b)** chessboard extinction of a quartz clast from of sample KBH1-347; **c)** high and low temperature recrystallization by grain boundary migration of quartz clasts from sample KBH1-350; **d)** flame-like structures in a K-feldspar clast from sample KBH1-346; **e)** alteration (sericification) and albite gemination of plagioclase clast from sample KBH1-348; **f)** hornblende crystal with its typical green colour and strong cleavage from sample KBH1-347. The two areas circled in yellow indicate the alteration by the Chl. It is possible to observe a sub-vertical fault/ fracture calcite-bearing vein cutting the wall rock.

Regarding the amphibolites (sample KBH6-70), the rock is cut by a dense network of fractures and veins (Figure 5.14a). *Epidote* crystals are recognisable by their high relief and harlequin interference colour (Figure 5.14b) and are cut by fractures filled by chlorite (yellow circle in Figure 5.14a-c). *Chlorite* is widespread in most of the basement rocks (Figure 5.14c). *Quartz* crystals have cuspate-lobate boundaries possibly due to silica dissolution. These boundaries are decorated by chlorite, which may precipitate from silica under-saturated fluids.

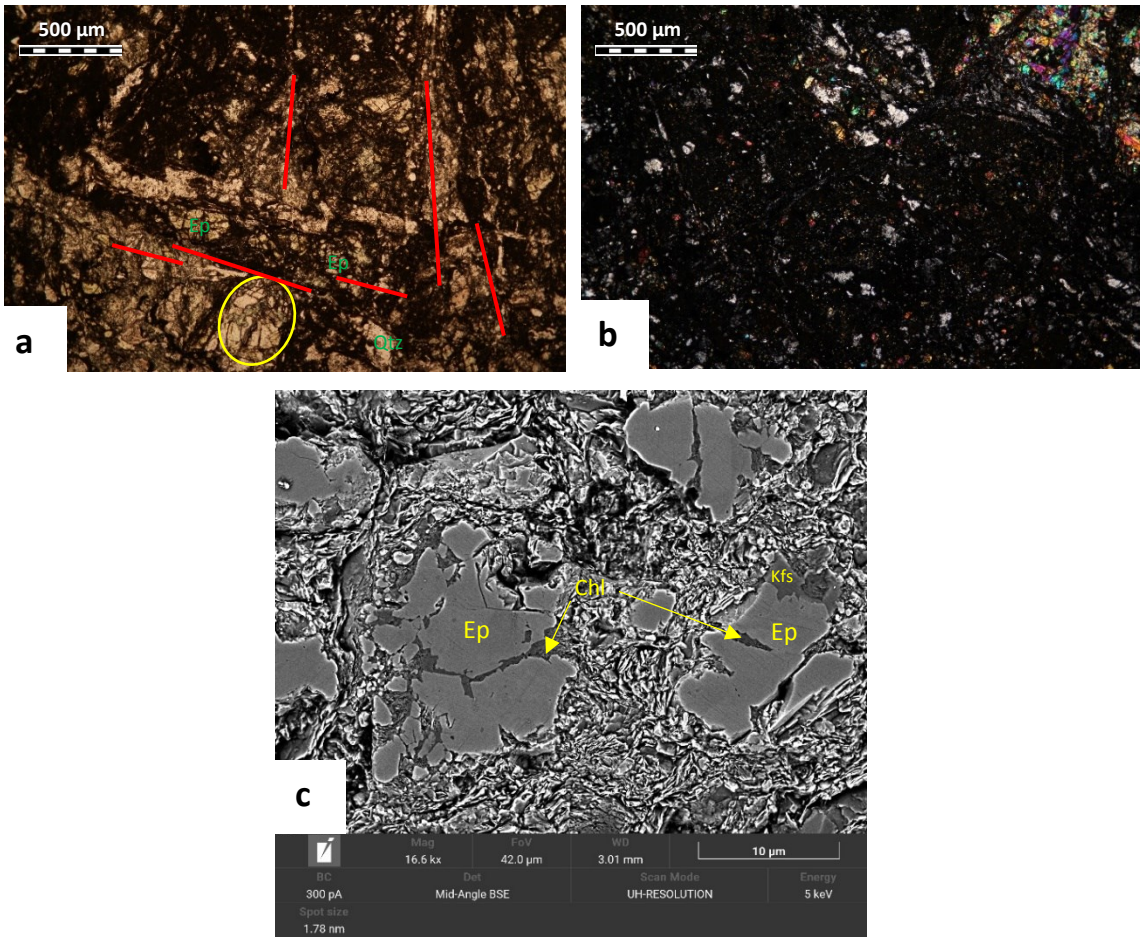

Figure 5.14. Highly fractured amphibolite basement (sample KBH6-70. **a)** Epidote clasts cut by fractures filled by chlorite; **b)** clast of epidote grains are visible in the top-right corner. The black matrix is made by small epidote grains and chlorite; **c)** Vein matrix in Figure (b) with chlorite filling cracks in epidote (BSE-FESM image).

5.2.3. Fault rocks (latu-sensu)

Fault rocks in the area include mylonites, breccias and cataclasites, and faults/fractures filled by epidote, chlorite, quartz and calcite veins. These fault rock assemblages pertain to both the so called “brittle” and “ductile” regimes: I followed the classification of fault rocks in (Scholz, 2019). I distinguished breccias and cataclasites from faults/fracture filled by epidote, chlorite, quartz, and calcite veins based on the % of vein deposit (i.e., cement) in the matrix as in (Woodcock & Mort, 2008). Though the studied samples come from wells KBH1, KBH6 and KBH7 (Figures 1.1, 2.13 and Table 4.1) located up to 30 km apart, and their deformation histories, petrography, etc., might be different, they share some common microstructural and alteration features as presented below.

Mylonites

There are different generations of mylonites cutting the Proterozoic basement as they are pre-Cretaceous (i.e., pre-Deccan volcanism) in age and span from granulitic to amphibolitic facies conditions (see (Misra et al., 2022). The mylonites found in the studied cores are (1) interpreted as altered under greenschist-facies conditions and cut the amphibolites (KBH6-69, Fig. 3.5f) or (2) found as fragments in the cataclasites (KBH1-351, Fig. 5.15). The mylonitic fragment is composed of quartz, chlorite, titanite and hematite and is suspended in a fault chlorite-bearing vein which is cut by a calcite-bearing vein (Figure 5.15).

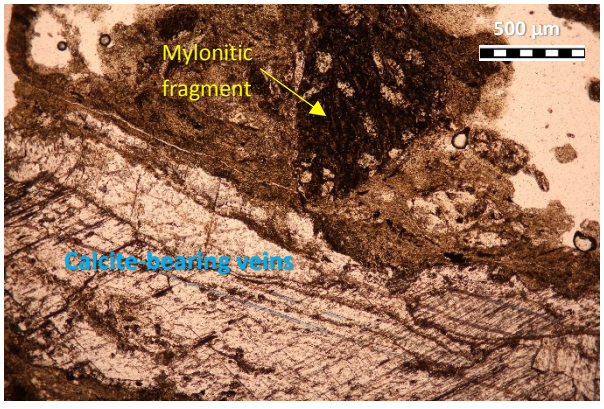

Figure 5.15. Mylonitic fragment in a fault/ fracture chlorite-bearing vein, cut by a calcite-bearing vein (image from KBH1-351).

Breccias and cataclasites (e.g., KBH1-346, -347, -353; KBH6-67; KBH7-595)

In the three studied boreholes, faults sharply cut the granitic and amphibolitic basement and are made of cohesive breccias and cataclasites cut by faults/fractures filled by chlorite, epidote and calcite veins (Figure 5.16a, b).

Breccias and cataclasites have a chlorite-rich or epidote or calcite matrix and clasts are in contact to each other (e.g., Figure 5.16a to f). In the case of breccia with chlorite matrix, it appears dark green in parallel and brown in crossed Nicols (*Brown Chl KBH1*, Figure 5.16a, d). Based on its chemical composition (section 5.3), this type of chlorite has an estimated formation temperature of ca. 252±20°C (see section 6.1). If the breccias and cataclasites cut the granitic basement the clasts are made of quartz, plagioclase and K-feldspar from the wall rocks (Figure 5.16a to e). Usually, *quartz* grains have wavy extinction and lobed and cusped rims, possibly related to cataclasis associated with fluid-rock interaction and dissolution in under-saturated silica fluids (this is consistent with the widespread precipitation of chlorite); *K-feldspar* grains have angular and sharp-edged rims due to dominant fragmentation processes (Figure 5.16e); *plagioclase* grains are also fragmented and include twins.

Other breccias and cataclasites and especially those cutting the amphibolitic basement in KBH6, possibly formed at the brittle-transition for quartz, as attested by the presence of both cataclastic features and evidence of dynamic recrystallization in quartz by low temperature grain boundary migration (Fig. 5.16f). Also in this case fluid-rock interaction results in quartz dissolution (lobed and cusped rims) (Figure 5.16f). Similar brittle features associated with fluid-rock interaction can be found in borehole KBH7 (dissolution features in quartz, microfaults, domino-like microstructures, etc., Figure 5.16 g-h).

As mentioned above, breccias and cataclasites are systematically cut by faults/fractures filled by calcite veins (Figure 5.16b). Only in the core KBH1 the faults/fractures filled by calcite veins reactivate the breccias and cataclasites (Figures 5.9, 5.16a). In any case, the calcite-rich vein breccia is neither truncated nor reactivated by other faults/fractures with other mineral filling (Figure 5.16e).

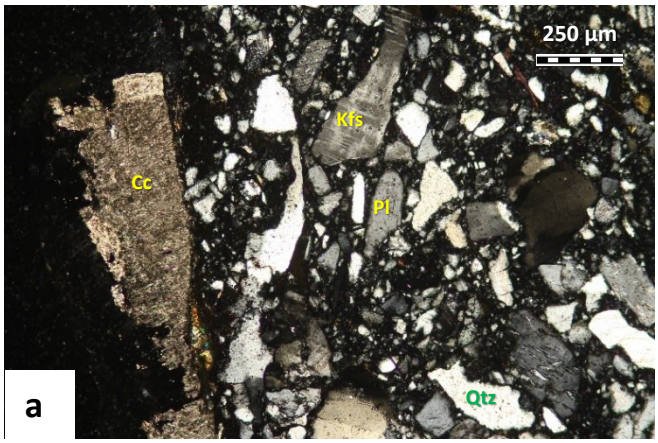
250 µm
Kfs
Cc
Pl
Qtz
a

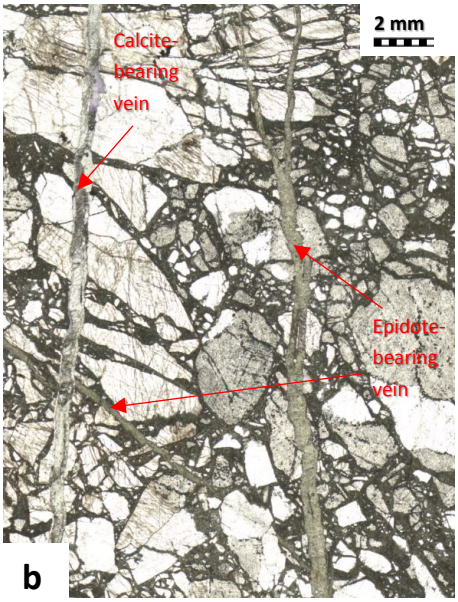
2 mm
Calcite-bearing vein
Epidote-bearing vein
b

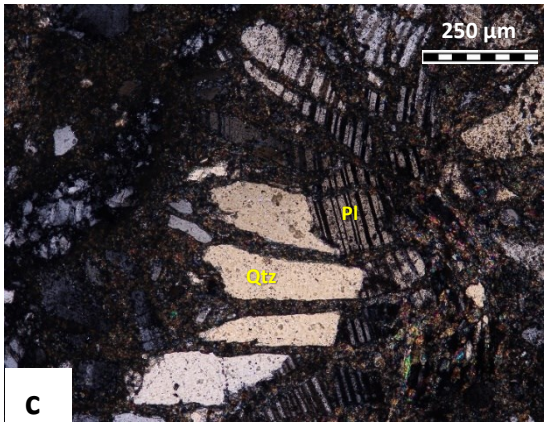
250 µm
Pl
Qtz
c

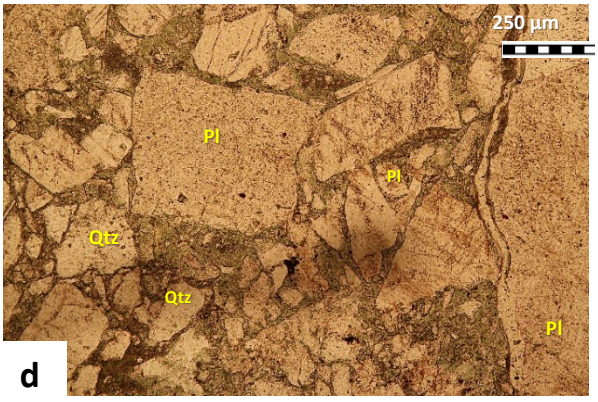
250 µm
Pl
Pl
Qtz
Qtz
Pl
d

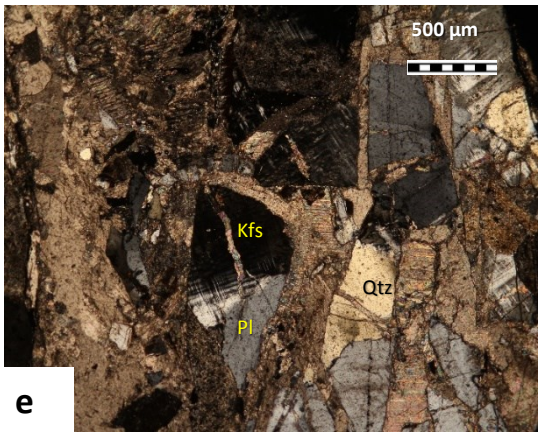
500 µm
Kfs
Qtz
Pl
e


250 µm
f

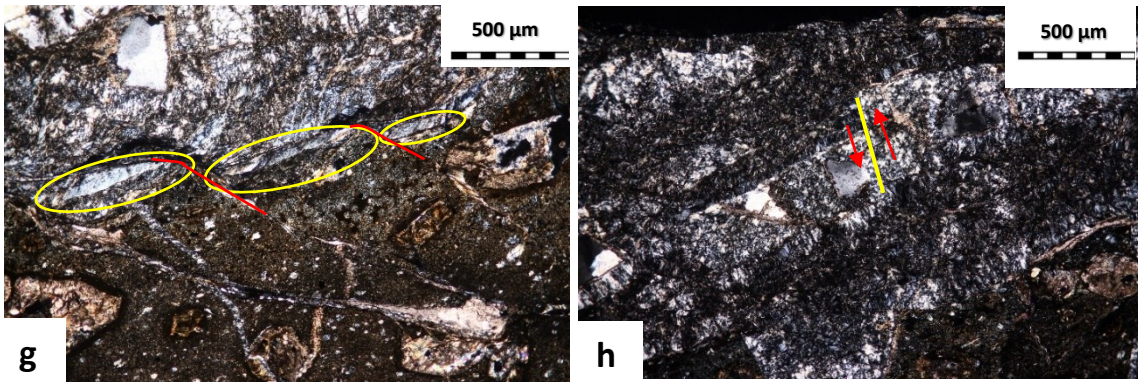

Figure 5.16. Breccias and cataclasites **a)** Cataclasite with chlorite matrix cut by calcite-bearing vein (image from KBH1-346); **b)** cataclasite with epidote matrix cut by epidote-bearing and calcite-bearing veins (image from KBH1-353); **c)** detail of (b) with fragmented quartz and plagioclase clasts; **d)** chlorite matrix in (a) with quartz clasts with lobed and cusped boundaries and K-feldspar clasts with angular and sharp-edged boundaries; **e)** breccia and cataclasite with calcite matrix (image from KBH1-347); **f)** breccia and cataclasite with chlorite matrix and evidence of low temperature crystal plastic deformation for quartz (image from KBH6-67); **g)** fragmented quartz grains (yellow circles) along the contact between basement rocks and the dyke (image from KBH7-595); **h)** fragmented quartz grains inside the breccia and cataclasite with chlorite matrix (image from KBH7-595).

<u>Faults and fractures filled by epidote veins</u> (e.g., KBH1-346, -352)

Faults and fractures filled by epidote veins are predominantly sub-vertical structures that cut through the granite basement and breccia. They occur as:

(1) Ultracataclasites with epidote matrix and small fragmented clasts of albite, plagioclase, K-feldspar, quartz, chlorite and pyrite (Figure 5.17a, e.g., KBH1-352);

(2) Fractures filled by epidote veins with well-developed epidote crystals (Figure 5.17b, e.g., KBH1-346, -347). These are peculiar veins cutting granitoid rocks and change in structure and mineral assemblage depending on the wall rock minerals. When the fracture cuts K-feldspar grains, the vein filling includes well-developed epidote crystals at the centre bounded by small quartz and Fe-oxides at the contact with the wall rocks. When the same fracture cuts quartz grains, the vein filling includes quartz grains with the fracture boundaries decorated by fluid inclusions trails (Figure 5.17c). In general, this second type of fault and fracture filled by epidote veins are sub-vertical and thus parallel to the other "brittle" structures such as breccias and cataclasites (e.g., KBH1-346).

The faults and fractures filled by epidote veins are systematically cut by calcite-bearing veins (see Figure 5.17d).

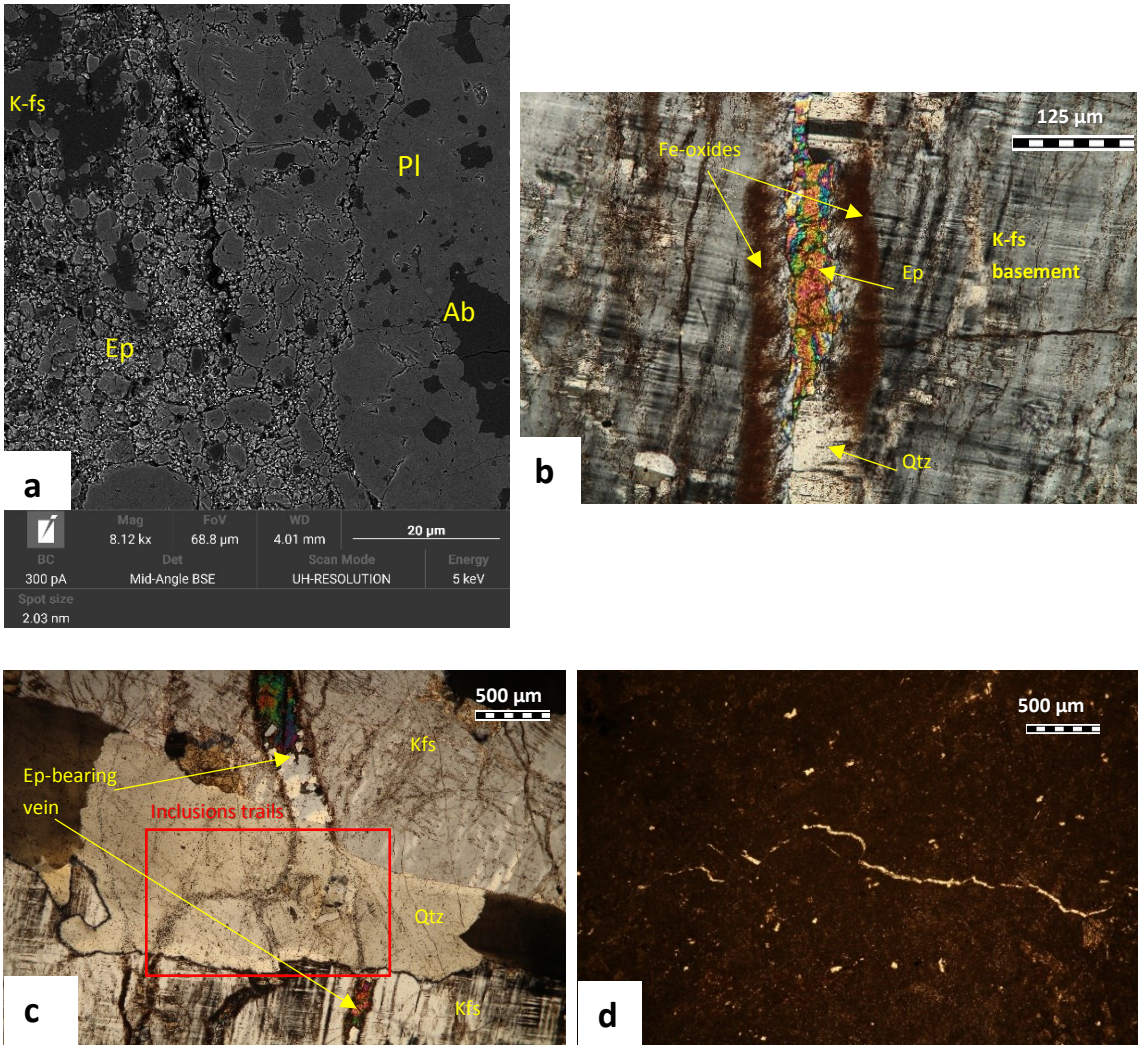

Figure 5.17. Faults and fractures filled by epidote veins **a)** Fault and fracture filled by epidote vein with fine grains of albite, plagioclase and K-feldspar (SEM image from KBH1-352); **b)** fault and fracture filled by epidote vein with epidote crystal in the center and quartz crystals and Fe oxides at the boundary with K-feldspar crystals (image from KBH1-346); **c)** Same fracture as in (b), but now the fracture cuts quartz grins. The red rectangle shows the fluid inclusion trails (image from KBH1-346); **d)** calcite-bearing vein cuts the fault epidote-bearing vein (image from KBH1-352).

<u>Faults and fractures filled by quartz veins</u> (e.g., KBH6-72, -71, -70)

Quartz-bearing veins are only found in KBH6 (Figure 5.7). They are both sub-vertical and sub-horizontal with respect to the core axis. Faults/fractures filled by quartz (+/-chlorite) veins are organized in a dense network of conjugate fractures that cut each other (e.g., Figures 5.18a from sample KBH6-72 cutting the amphibolitic basement). In the quartz-bearing vein of sample KBH6-70 (Figure 5.18b), EDS elemental maps show that the vein boundaries are enriched in Si, while the vein centre is enriched in Mg, Fe, and Al, typical of chlorite (Figures 5.18c to i). Chlorite is also at the contact with quartz grains with lobate-cuspate boundaries (Fig. 5.18l). A possible interpretation is that the fracture, originally filled by a quartz vein, has been reactivated and filled by a chlorite vein (Figure 5.18b to i). Calcite-bearing veins cut systematically the faults and fractures filled by quartz (and chlorite) veins (Figure 5.18m).

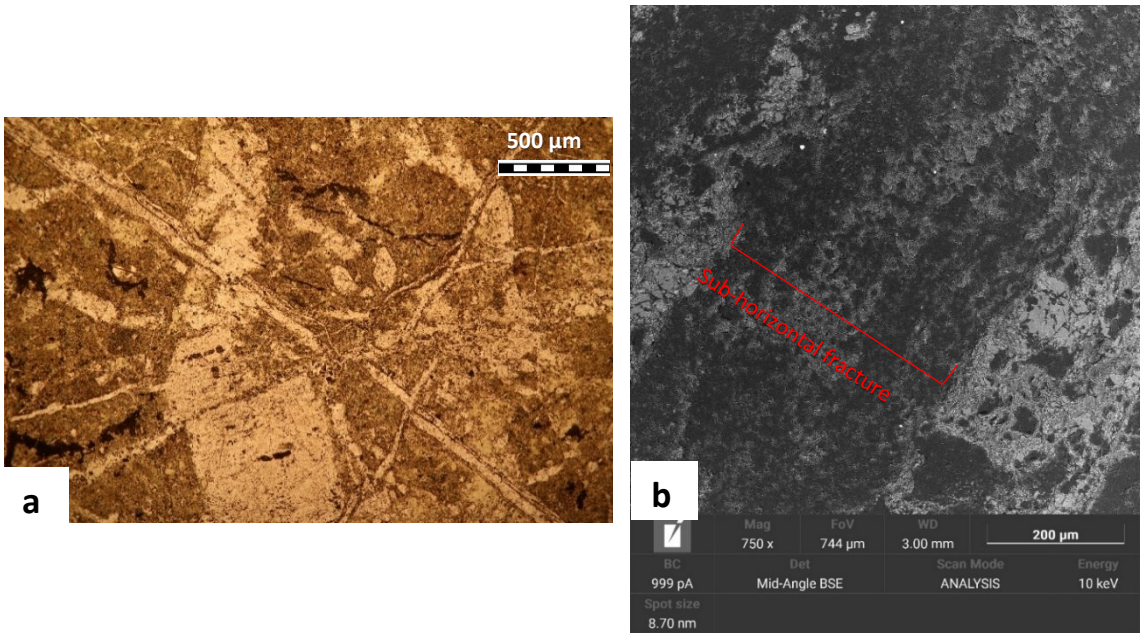

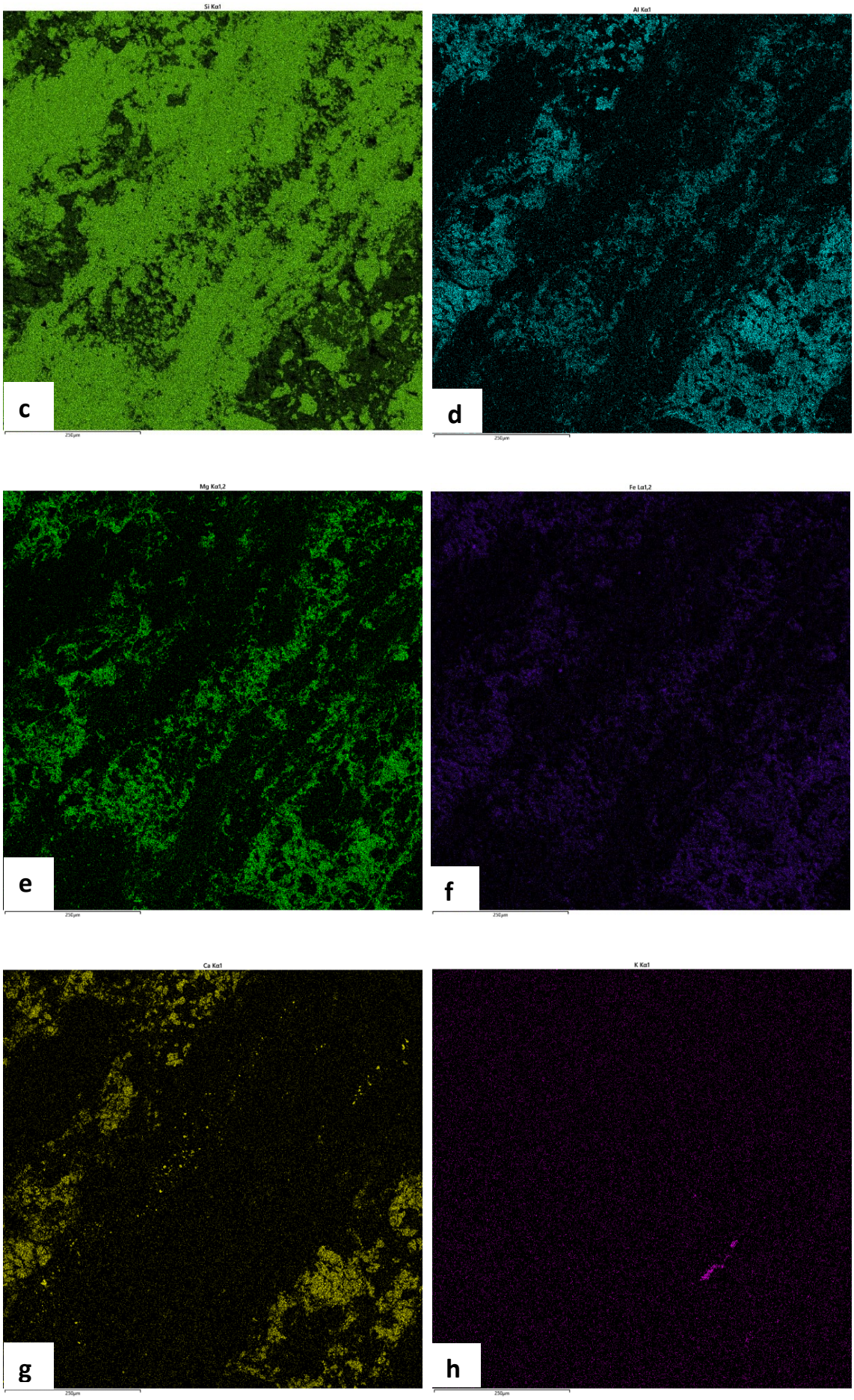
Si Kα1
c
Al Kα1
d
Mg Kα1,2
e
Fe La1,2
f
Ca Kα1
g
K Kα1
h

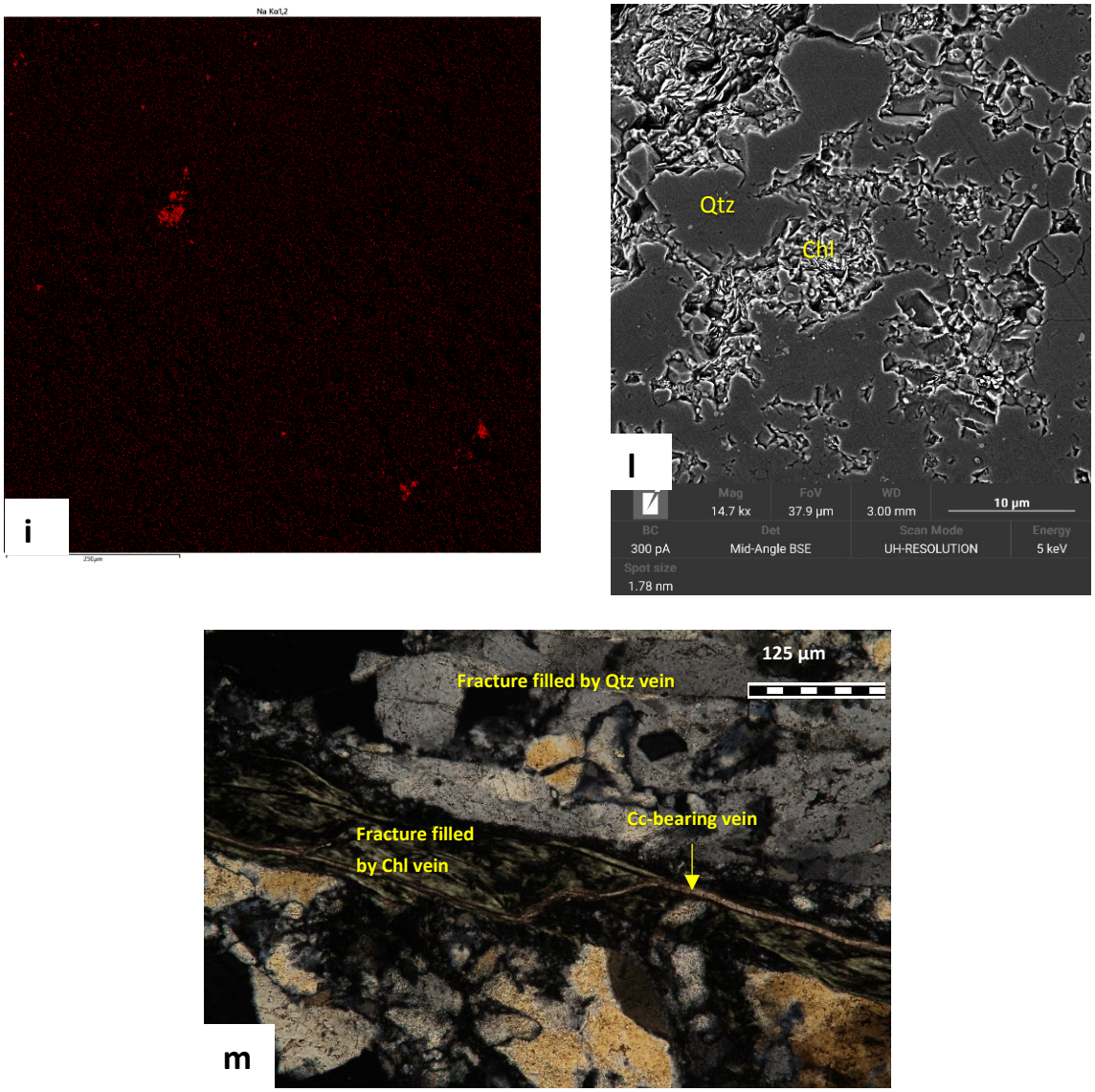

Figure 5.18. Faults and fractures filled by quartz veins. **a)** crosscutting relations between fault/fractures filled by quartz veins; **b)** SEM image of sub-horizontal fracture filled by quartz and chlorite; **c) to i).** EDS maps of Si, Al, Mg, Fe, Ca, K and Na. Chlorite is mainly found at the vein centre (Mg-, Fe- and Al-rich area). This suggests the reactivation of the fracture by chlorite (see SEM image (l)). The fracture cuts through the altered amphibolite basement which includes plagioclase, K-feldspar and quartz. **l)** fault/ fracture filled by quartz vein reactivated by the chlorite (SEM image from KBH6-70); **m)** Fault/fracture quartz-bearing vein cut by chlorite-and lastly by calcite-bearing fault/fracture vein (image from KBH6-72).

<u>Faults and fractures filled by chlorite veins</u> (e.g., KBH1-348, 350; KBH6-69; KBH7-595)

They are found in all studied samples and include:

1) sub-vertical faults/fractures with clasts of breccia/cataclasite suspended in a fine-grained chlorite matrix (e.g., KBH1-348 Figure 5.19a; KBH6-69, Figure 5.19b). They are associated with *en-echelon* arrays of thin (< 0.1 mm thick) fractures filled by chlorite (e.g., KBH1-350, Figure 5.19c-d);
2) sub-vertical to sub-horizontal chlorite-bearing pure veins (i.e., without clasts) which cut the amphibolite basement (e.g., KBH1-71, Figure 5.19e).

Chlorite crystals in the veins and in the basement rocks have different optical properties which may reflect different chemical compositions and temperatures of formation (see Chapters 5.3 and 6.1):

- *Brown Chl KBH6* or dark green in parallel and brown in crossed Nicols (KBH6-71, Figure 5.19e). This brown chlorite, though optically similar to the *Brown Chl KBH1* found in the breccia and cataclasite of KBH1 (sample KBH1-346, Fig. 5.16a, d) has a different composition (section 5.3) which is related to an estimated formation temperature of 221±25°C (see section 6.1);
- *Green Chl* or pale green in parallel and green in crossed Nicols. They cut the veins which have brown chlorite in crossed Nicols previously described (KBH1-71, Figure 5.19e). Based on its chemical composition (section 5.3), this type of chlorite has an estimated formation temperature of 211±25°C (see section 6.1);
- *Blue Chl* or pale green in parallel and blue in crossed Nicols (KBH1-348, Figure 5.19a, f). This latter vein may also include small calcite grains, which possibly precipitated together with chlorite (see discussion in Chapter 6.2). Based on its chemical composition (section 5.3), this type of chlorite has an estimated formation temperature of 197±30°C (see section 6.1).

Chlorite also fills the contact of a Deccan dyke with the crystalline basement rocks (sample KBH7-595, Figures 5.19h). Again, different optical properties were observed for chlorites:

- Rayed Chl with chlorite grains have radial structures and it is in association with quartz (KBH7-595, Figure 5.19g). Based on its chemical composition (section 5.3), this type of chlorite has an estimated formation temperature of 135±17°C (see section 6.1)
- Fibrous Chl with chlorite grains are arranged in fibers (Fig. 5.19g). Based on its chemical composition (section 5.3), this type of chlorite has an estimated formation temperature of 129±41°C (see section 6.1).

With the exception of sample KBH1-348 where calcite crystals may have precipitated from the percolating fluids together with chlorite (Figure 5.19f), chlorite-bearing veins are systematically cut by faults and fractures filled by calcite veins (Figure 5.20c).

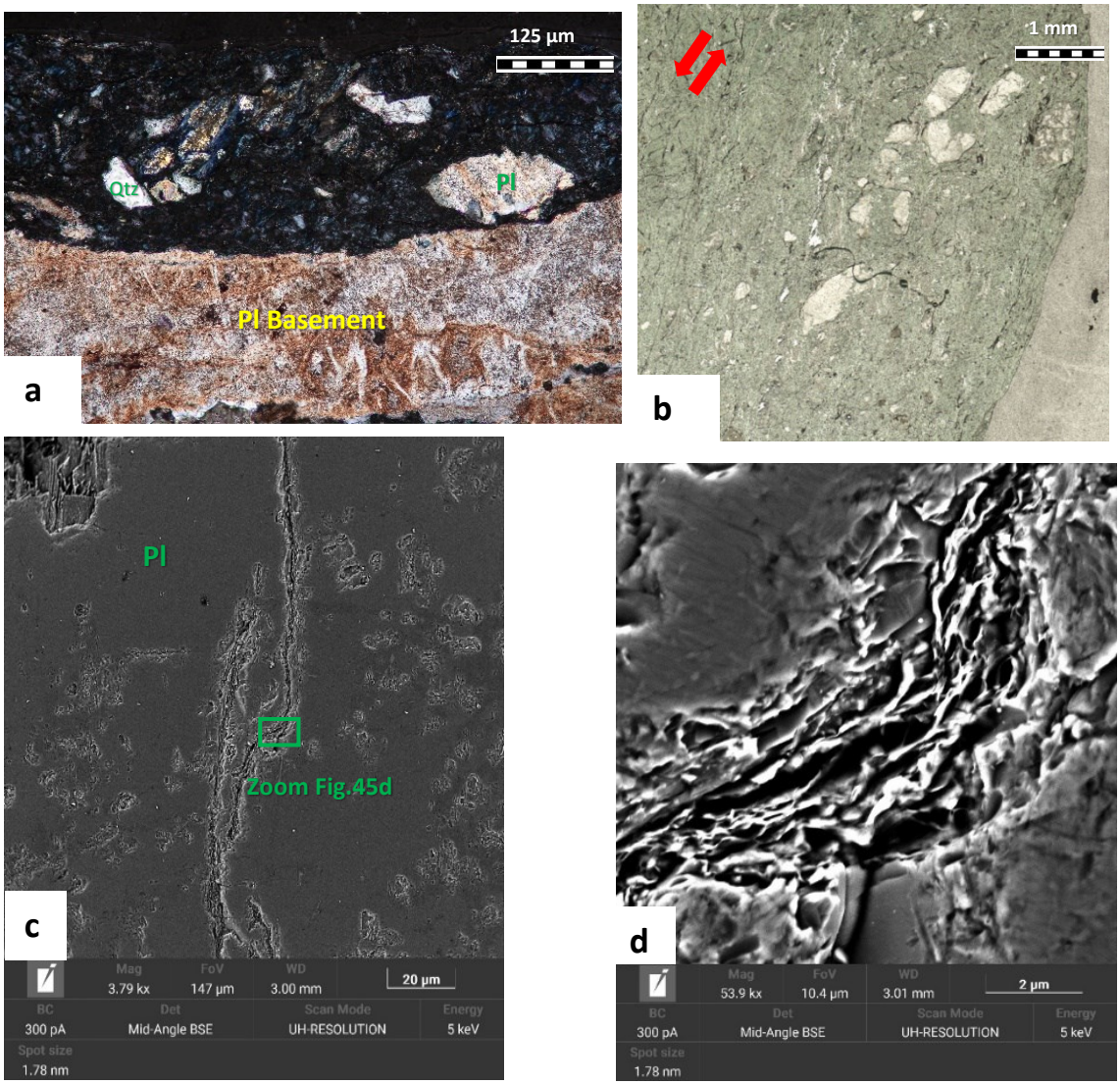

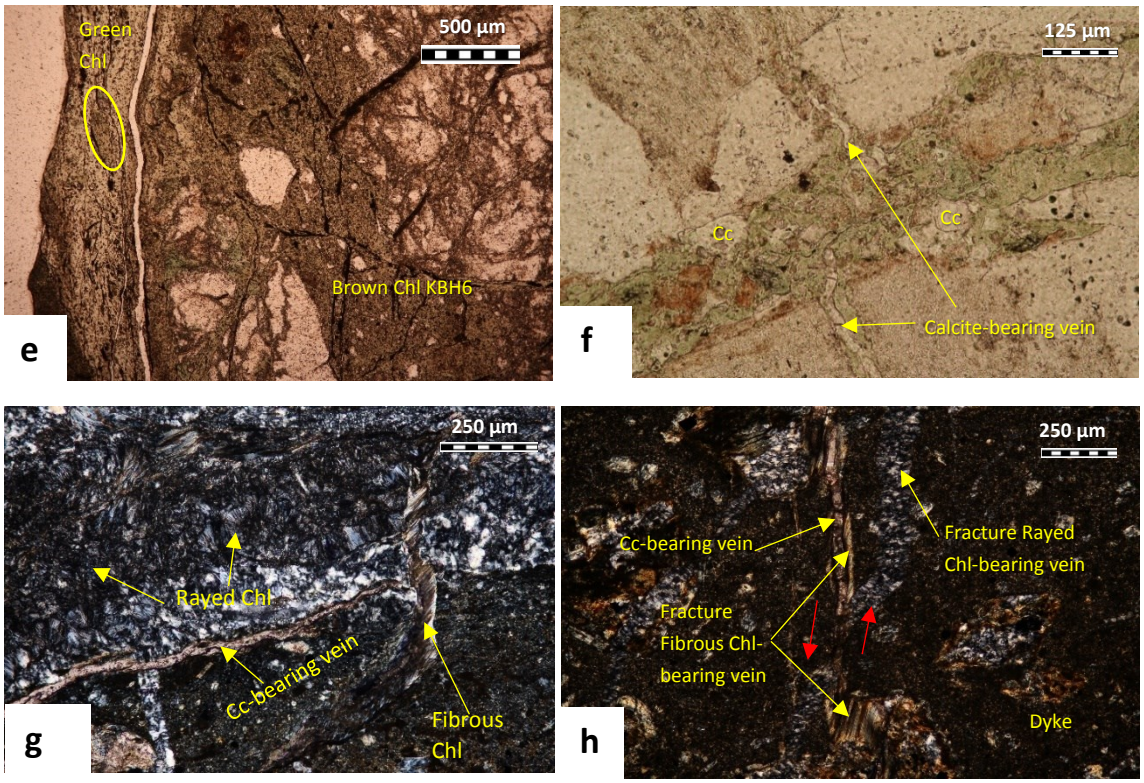

Figure 5.19. Faults and fractures filled by chlorite veins **a)** fault/ fracture filled by *Blue Chl* vein with polymineralic quartz and feldspar clasts (KBH1-348); **b)** fault/fracture chlorite-bearing vein with quartz clasts (image from KBH6-69); **c)** fault/fracture chlorite-bearing vein *in en-echelon* array cutting the basement rocks (SEM image from KBH1-350); **d)** zoom of (c) with micrometer in size chlorite crystals; **e)** fault/fracture filled by chlorite vein without quartz clasts with pale green in color chlorite under parallel Nicols (*Green Chl*, left side) cutting a fault/fracture with dark green color under parallel Nicols chlorite matrix (*Brown Chl KBH6*). In the yellow circle is visible a portion of the *Brown Chl KBH6* immersed in the fault/ fracture *Green Chl*-bearing vein (image from KBH6-71); **f)** chlorite-bearing vein with pale green color chlorite in parallel Nicols (*Blue Chl*). The vein includes calcite grains (image from KBH1-348); **g)** *Rayed* and *Fibrous Chl* with fracture filled by calcite vein cut everything (image from KBH7-595); **h)** *Fibrous* and *Rayed* chlorite-bearing fracture cutting the basaltic dyke. *Fibrous* Chlorite-bearing vein cuts the rayed Chl one and is subsequently cut by calcite-bearing veins (image from KBH7-595).

<u>Faults and fractures filled by calcite veins</u> (e.g., KBH1-350, KBH7-594)

Faults and fractures filled by calcite veins are present in all boreholes and in most of the studied samples they systematically cut the previously described fault rocks (i.e., fractures filled by epidote, quartz and chlorite veins; breccias and cataclasites with chlorite or epidote matrix, Figures 5.16a-b, 5.17d, 5.18m, 5.19h and 5.20a to d). The thickest calcite-bearing veins are filled with blocky, coarse-grained crystals to ultrafine groundmass (Figure 5.20a). In few veins, micro-crystals of chlorite are associated with calcite crystals and may have precipitated from the same fluid (e.g., KBH1-350; Figure 5.20b). Multiple generations of calcite growth fibres are found at

the basaltic dyke-basement rock contact (KBH7-594, Figure 5.20d). The calcite-bearing veins seem to disrupt the chlorite-bearing veins (circle in Figure 50d). The presence of multiple generations of calcite-growth fibers may suggest the occurrence of crack-sealing processes related to fluid percolation in the Koyna-Warna area. This is consistent with cross-cutting relations between faults and fractures calcite-bearing veins (e.g., KBH1-348, Figure 5.19f).

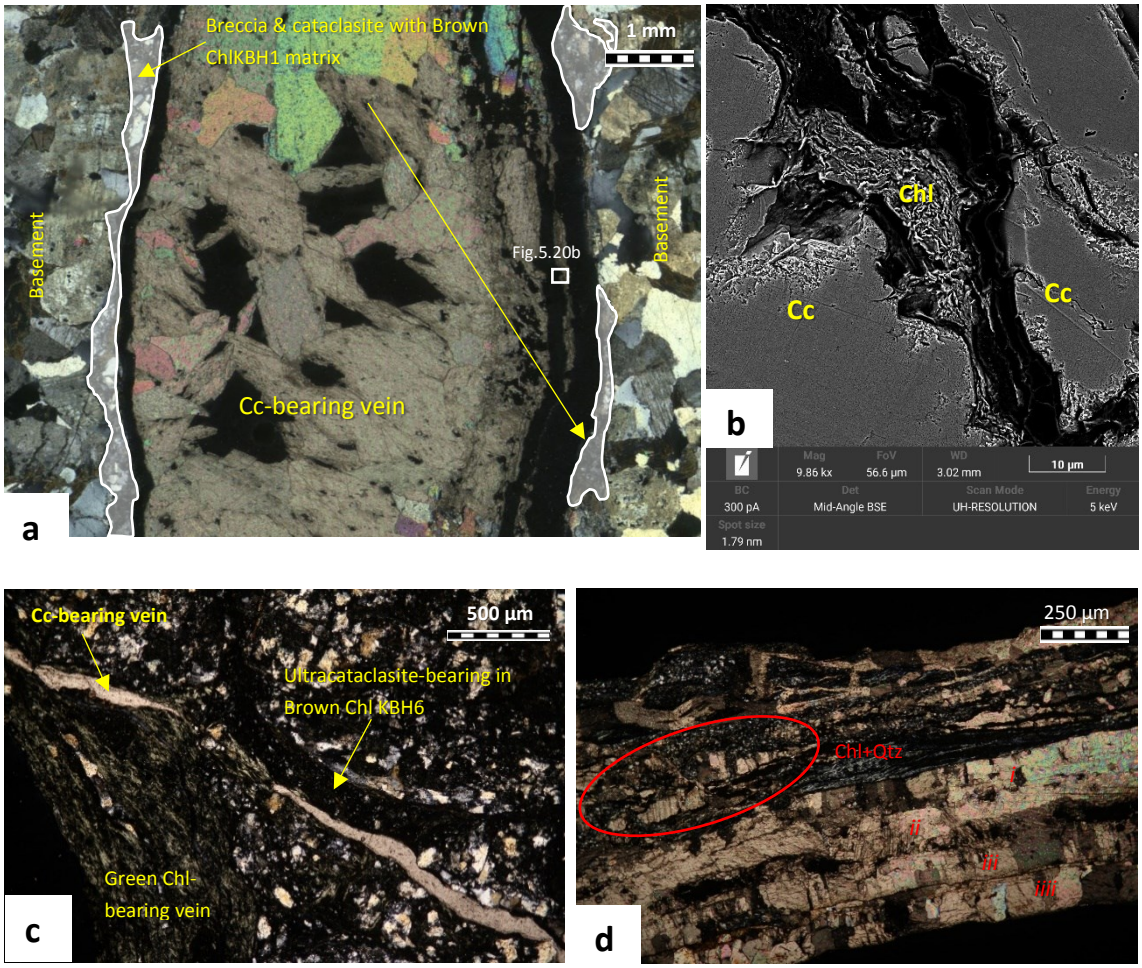

Figure 5.20. Faults and fracture filled by calcite veins. **a)** Calcite-bearing vein filling made by blocky, coarse-grained calcite crystals. The area highlighted in white color includes a chlorite-rich vein cut by the calcite vein (image from KBH1-350); **b)** Chlorite crystals in a calcite-bearing vein (SEM image from KBH1-350); **c)** Calcite-bearing vein cutting cataclasites and chlorite-bearing veins (image from KBH6-71); **d)** Multiple generations of calcite fibers (at least *i* to *iiii*, though age relations are not known) filling the contact between the basaltic dyke and the basement rocks. The calcite-bearing veins seem to disrupt the chlorite veins (circle in Fig. 50d) (sample KBH7-595).

5.3 WDS Analysis

Chlorite is abundant in most of the studied samples, though optical properties of chlorite may vary suggesting different chemical compositions (e.g., KBH1-346, 348; KBH6-71; KBH7-594, 595) which are probably be related to the temperature of formation of the chlorite. For this reason, FESEM-WDS spot analyses were carried out on the following chlorites to determine their composition in oxide weight percentage (wt.%) (Table 5.3; all the analysis are reported in the Appendix 3):

- *Brown Chl KBH1* or brown in color chlorite in crossed Nicols that fills the breccias and cataclasites (e.g., sample KBH1-346, Figure 5.16a, d);

- *Blue Chl* or blue in color chlorite in crossed Nicols that fills the veins (e.g., sample KBH1-348, Figure 5.19a,f);

- *Brown Chl KBH6* or brown in color chlorite in crossed Nicols that fills the veins (e.g., sample KBH6-71, Figure 5.19e);

- *Green Chl* or green in color chlorite in crossed Nicols (KBH6-71). The green Chl cuts *Brown Chl KBH6* in the selected sample (Figure 5.19e);

- *Rayed Chl* with chlorite grains have radial structures and it is in association with quartz (e.g., sample KBH7-595, Figure 5.19g, h);

- *Fibrous Chl* with chlorite grains are arranged in fibers (Fig. 5.19g). It cuts *Rayed Chl* in the selected sample (Figure 5.19g, h);

Other FESEM-WDS analysis were performed on the faults and fractures filled by chlorite vein of sample KBH6-69 (figure 5.19b).

Sample	Type of Chl	SiO_2	σ (SiO2)	TiO_2	σ (TiO2)	Al_2O_3	σ (Al2O3)	V_2O_3	σ (V2O3)	Cr_2O_3	σ (Cr2O3)	FeO	σ (FeO)	MnO	σ (MnO)	NiO	σ (NiO)	MgO	σ (MgO)	CaO	σ (CaO)	K_2O	σ (K2O)	Total
KBH1-346	Brown Chl	27.920	0.417	0.120	0.007	19.550	0.539	0.000	0.000	0.020	0.000	21.370	0.778	0.220	0.075	0.000	0.000	18.010	0.452	0.080	0.038	0.060	0.037	87.180
KBH1-348	Blue Chl	28.940	0.804	0.000	0.000	16.010	0.664	0.000	0.000	0.080	0.021	21.080	0.794	0.250	0.080	0.000	0.000	17.560	1.002	0.210	0.055	0.070	0.041	84.040
KBH6-69	Dark Chl	29.120	0.617	0.000	0.000	19.570	1.249	0.100	0.054	0.000	0.000	16.340	1.899	0.210	0.105	0.000	0.000	20.840	0.483	0.080	0.020	0.000	0.000	86.130
KBH6-69	Bright Chl	27.580	0.363	0.000	0.000	18.570	0.098	0.060	0.033	0.000	0.000	22.150	0.833	0.280	0.058	0.000	0.000	18.020	0.625	0.050	0.027	0.000	0.000	86.710
KBH6-71	Brown Chl	28.090	1.361	0.000	0.000	18.490	0.499	0.000	0.000	0.000	0.000	20.790	1.362	0.290	0.072	0.000	0.000	18.050	1.037	0.060	0.029	0.030	0.011	85.780
KBH6-71	Green Chl	28.870	0.917	0.000	0.000	19.750	0.471	0.000	0.000	0.000	0.000	16.090	0.751	0.110	0.056	0.000	0.000	20.590	0.811	0.050	0.028	0.000	0.000	85.460
KBH7-595	Fibrous Chl	33.320	2.010	0.000	0.000	14.060	0.582	0.000	0.000	0.140	0.040	14.690	0.273	0.180	0.066	0.000	0.090	23.680	0.836	0.290	0.194	0.040	0.018	86.390
KBH7-595	Rayed Chl	34.650	0.398	0.000	0.000	11.620	0.366	0.000	0.000	0.000	0.000	12.940	0.329	0.120	0.062	0.150	0.071	26.120	0.374	0.090	0.031	0.040	0.011	85.520

Table 5.3. Average values in wt.% of the oxides with their standard deviation for each chlorite type. SiO_2, TiO_2, Al_2O_3, FeO, MnO and MgO values were obtained with the WDS detector, while the other values with the EDS detector.

The FESEM-WDS analysis confirm the different composition of the chlorites. In detail (Table 5.3):

KBH1: large variation in Al_2O_3 content (*Brown Chl KBH1* 19.55% vs. *Blue Chl* 16.01%) and a small in SiO_2 (*Brown Chl KBH1* 27.92% vs. *Blue Chl* 28.94%);

KBH6: two types of chlorites were found in the KBH6-69 sample during FEG-SEM investigations (unfortunately, the FEG-SEM-BSE image is not available): (1) darker and therefore poorer in FeO (16.34% *Dark Chl*) and (2) lighter and therefore richer in FeO (22.15% *Bright Chl*). The *Bright Chl* has the highest FeO content of all the studied chlorites. The chlorite sample KBH6-71 have a great variation in FeO (*Brown Chl KBH6* 20.79% vs. *Green Chl* 16.09%) and a small one in Al_2O_3 (*Brown Chl KBH6* 18.49% vs. *Green Chl* 19.75%);

KBH7: the fibrous and radiated chlorites crystals have slightly different compositions with respect to each other, but also to the other samples. For example, the FeO content is lower (*Fibrous Chl* 14.69%, *Rayed Chl* 12.90%), and the SiO_2 content higher (*Fibrous Chl* 33.32% vs. *Rayed Chl* 34.65%) with respect to those measured in the other chlorites. This may be related to lower (estimated) formation temperatures of the *Fibrous Chl* and *Rayed Chl* (see Chapter 6.1).

6. Discussion

The Koyna-Warna region has been a seismically active in the last six decades due to (1) the pre-existing stress loading in this cratonic area, (2) the presence of pre-existing fractures/faults, (3) the construction of two large dams since 1962 and the impounding/emptying of the associated reservoirs that perturbed the state of stress in the area, and (4) the percolation of fluids from the reservoirs into the fault/fracture network (Chapters 1.2, 2.1.2, 3.3). This combination of factors made the Koyna-Warna area a region intensely affected by the (human-induced) reservoir-triggered seismicity (RTS) (Gupta, 2002). This stimulated the development of a large drilling project started in 2011 which included nine deep boreholes (Gupta, 2017b). The mineralogical and microstructural study of the samples collected from various depths of three (KBH1, KBH6 and KBH7) of the nine deep boreholes wells allowed me to investigate the deformation features present in the basement rocks and possibly related to the ongoing RTS. While KBH1 and KBH7 are located close to the epicentral area of the 1967 Mw 6.3 earthquake and to the Donichawadi Fault, KBH6, located south of the Warna Dam, is 30 km southeast of epicentral area (Figures 1.1, 2.13). However, the attitude of the fractures and the fault rocks in KBH1 seem to record similar deformation patterns as in the other boreholes (see Chapter 5.2). In fact, in all boreholes, most fractures are sub-vertical (Goswami et al., 2020; Misra et al, 2022) and fault rocks include breccia and cataclasites and faults and fractures filled by veins, confirming that the faults were reactivated in a brittle regime (see Chapter 5.2). Moreover, the fact that several sub-vertical faults/fractures were found in the boreholes which are vertical, suggest that the abundance of sub-vertical faults/fractures is very high.

The microstructural (FE-SEM and OM) and semi-quantitative mineralogical (XRPD) analysis performed in my thesis (Chapter 5) show that chlorite and calcite are the two main filling of the most recently activated faults and fractures (Table 5.1) and calcite-bearing veins are associated with the last deformation event in all the studied samples (Chapter 5.2). In particular, the most common brittle features are:

- Breccias and cataclasites with chlorite, epidote and calcite matrix;

- Faults and fractures filled by chlorite, epidote, quartz and calcite veins.

The microstructural study allowed me also to recognize different types of chlorites based on their optical properties (Chapter. 5.2). This was confirmed by chemical analysis performed with the WDS-FEG-SEM (Chapter 5.3) which allowed me to distinguish *Brown Chl KBH1*, *Blue Chl*, *Bright Chl*, *Dark Chl*, *Brown Chl KBH6*, *Green Chl, Rayed Chl* and *Fibrous Chl*. In some samples, systematic crosscutting relations allow me to state that *Brown Chl KBH6* and *Rayed Chl* precede *Green* and *Fibrous Chl,* respectively. Unfortunately, in several samples the crosscutting relations between *Brown Chl KBH1* and *Blue Chl* or *Dark* and *Bright Chl* remain uncertain. However, the chemical analysis allowed me to apply the low-temperature chlorite geothermometer (Bourdelle & Chatelineau, 2015) to estimate the temperature of precipitation of chlorite in the faults/fractures. Given that calcite-bearing veins cut the faults/fractures filled by chlorite veins, this analysis allowed me also to estimate the upper temperature limit of calcite precipitation and, to some extent, to reconstruct the sequence of deformation events. Furthermore, the temperature estimate of chlorite precipitation/formation in the fault rocks allows me to compare these faults (i.e., deformation mechanisms) with those currently active at hypocentral depths in the Koyna region (64-100°C < T < 160-250°C, Ray et al., 2021).

6.1 Estimate of the temperature of formation of chlorites

Chlorite is a relevant indicator of rock history because its broad spectrum of compositional variation is sensitive to formation conditions such as pressure (P), temperature (T), redox conditions, as well as rock and fluid composition (Bourdelle, 2021). The structure of chlorites can be defined as a solid solution model (Holland et al., 1998), knowing that most chlorite compositions in nature are between Fe,Mg-sudoite, Fe,Mg-amesite and Al-free chlorite end-members (Bourdelle & Chatelineau, 2015). This solid solution favours cation exchanges by allowing the combination of a multitude of chemical substitutions (Deer et al., 1994). Therefore, chlorite has a wide stability field ranging from low temperatures (LT), or ≈ 80°C for diagenetic and low-grade metamorphic chlorites, to high temperatures (HT) up to 700°C. However, much depends on the pressure involved: the higher the pressure the lower the temperature at which chlorite dehydrates, the lower the pressure the higher the dehydration temperature (Cai & Inoue, 2019).

As observed in the Koyna samples, I noticed different types of chlorites under the optical microscope, especially observing the shade and colour at parallel and crossed Nicols, respectively (Chapter 5.2). Subsequently, chemical analysis with WDS-FEG-SEM confirmed the presence of different chlorites. Due to the variety of chlorite composition in the same geological setting, the Bourdelle & Cathelineau (2015) low-temperature chlorite geothermometer was used to derive the formation temperatures of these phyllosilicates, also in support of the reconstruction of the sequence of deformation events (Table 6.1). This thermometer was used because the R^{3+} values are between 1.5 and 3 (apfu, atoms per formula unit) and because, as will be seen in Figure 6.1b, the values of the analysis points are enclosed within the range of the LT chlorites (Bourdelle & Cathelineau, 2015; Bourdelle, 2021). There are three different types of geothermometers for low-temperature chlorites: the first consists of an empirical calibration (Cathelineau & Nieva, 1985; Hillier & Velde, 1991), which directly links chlorite composition with temperature, but did not yield good results; the second approach is based on a thermodynamic database (Vidal et al., 2001, 2005), and is the most rigorous; the last, that one I used, is a semi-empirical approach, which considers chlorite + quartz equilibrium and it uses the ratio of end-member activities to link chlorite compositions to temperature via the equilibrium constant (K) (Inoue, et al.,

2009; Bourdelle et al., 2013; Lanari et al., 2014). The latter approach was found to be the best compromise between the simplicity/applicability limit on the one hand and rigour/complexity on the other by combining an empirical equation linking the equilibrium constant (K) and temperature (T), and a multi-component solid solution model (Bourdelle, 2021). The equation of the semi-empirical model is:

$$\ln \Pi_j \ (a_{ideal})_j^{v_j} = \frac{-\Delta G_r^0}{RT} = \frac{A}{T} + B, \qquad \text{Eq. 1}$$

where *A* and *B* are two constants, while a_{ideal} is calculated for each end-member value of j as follows:

$$(a_{ideal})_j = \Pi_s \Pi_m \left(\frac{ns}{r_m} X_m\right)^{r_m}, \qquad \text{Eq. 2}$$

where *ns* is the multiplicity of the s-site, r_m and X_m are the number and mole fraction of the cation m in the s-site, respectively. This model requires the calibration of the A and B constants according to the chlorite + quartz equilibrium and the definition of the end-members involved and the cation distribution at the s-site (Bourdelle, 2021). Bourdelle et al. (2013) in his geothermometer chose the magnesium and iron end-members of the Al-free chlorite, amesite and sudoite and an ordered distribution model of the cationic sites, following Vidal et al. (2001) and Bailey, (1988) for trioctahedral chlorites. The model of Bourdelle et al. (2013) is based on the following reaction:

Al-free Mg-chlorite + 3 Mg-sudoite = 3 Mg-Amesite + 7 Quartz + 4 H_2O Eq. 3

It is important that the thermometer is calibrated by assuming the activities aH_2O = $aSiO_2$ = 1. The aH_2O = 1 is assumed because we are in LT and thus in diagenetic, hydrothermal or low-grade metamorphic conditions (Inoue et al., 2009), while $aSiO_2$ = 1 because quartz-rich rocks prevail, since the model is based on chlorite + quartz equilibrium. The thermometer calibrated by Bourdelle et al. (2013), following Eq. (2) and (3), is expressed by the equation:

$$\log K = -\frac{9400}{T(K)} + 23.40 \qquad \text{Eq. 4}$$

It has been seen that this geothermometer works well for diagenetic and low-grade metamorphic contexts, especially for those T intervals where an abundance of Si is observed in chlorites (2.7<Si<3.6 apfu); the temperature must be below 350°C and the pressure below 3-4 kbar (Bourdelle & Cathelineau, 2015). Another aspect to consider is

that Bourdelle's geothermometer does not take Fe^{3+} into account because it has little influence on low-temperature chlorites; therefore, the Fe_{tot} present in the analysis points is bivalent Fe. In addition, the structure of low-temperature chlorites is heavily contaminated by clay minerals, causing an overestimation of the vacancy content; however, this is neglected by only selecting analyses with Na_2 + CaO + K_2O <1 % (Bourdelle et al., 2013). Low-T chlorites are independent of the Fe/(Fe+Mg) ratio, which mainly influences high temperature chlorites (T increases as the ratio increases), while they mainly depend on the Si and Al contents and the Mg_{M1}/Mg_{M2} ratio; the lower is the Al_2O_3 content, the lower is the formation temperature, while the higher is the SiO_2 content and the number of octahedral vacancies, the lower is the formation temperature continues to fall (McDowell & Elders, 1980).

The most useful way to see the relationship between chlorite composition and temperature is to use the isotherms in the R^{2+}-Si diagram (Wiewiora & Weiss, 1990), which is an effective plot to show R^{2+}-Si-Al vacancies-R^{3+} relationships. As can be seen in Figure 6.1b (R^{2+}-Si diagram with my samples), there are seven classes representing the different types of chlorite analysed by point chemical analysis with WDS-FEG-SEM. Before further describing this diagram, I focus more on the type of chlorites in the fault rock samples. Chlorites are solid solutions. In Figure 6.1a, it can be seen that all the chlorites in the sections belong to the trioctahedral class of clinochloro ($(Mg_5,Al)(Al,Si_3)O_{10}(OH)_8$). Two groups can be distinguished: the first, richer in Mg and with a wide Al range, consisting of the two KBH7 chlorites, and the second, with a stable, higher Al content and a lower Mg value, structured by all other chlorites (KBH1 and KBH6). Observing also the contents in Table 5.3 a big difference between the phyllosilicates of KBH1, KBH6 and KBH7 was already discernible. In the KBH7 the SiO_2 and MgO contents are much higher than the others, while Al_2O_3 and FeO are lower; this precludes an excellent distinction explaining a different geological and deformation history. Indeed, with these oxide contents, the KBH7 chlorites must have had lower formation temperatures than the others (this will be seen very clearly in Figure 6.1b). Two large groups can also be distinguished in the diagram in Figure 6.1b (the diagrams in Figure 6.1a, b were obtained using the WinCcac software and with the aid of the Gapher graphics program. The operation of the software is described in the article by Yavuz et al., 2015):

- The first, comprising the chlorites of KBH1 and KBH6, is enclosed between a range of 4.25< R^{2+}<5 (apfu) and a 2.75< Si< 3.25 (apfu) and the temperature is between 150-300°C. Each class follows a trend towards the pyrophyllite-gibbsite/Al-free chlorite line. In general, this deviation, parallel to the lines of constant R^{3+} values, indicates a contribution of di-trioctahedral exchange in addition to Tschermak substitution (Bourdelle et al, 2013, 2015). This in turn underlines the impact of the exchange vector $Si_{-1}\square_{-1}R^{2+}$. The whole group, however, does not show this trend towards the pyrophyllite-gibbsite/Al-free chlorite line, as individually each chlorite class follows a trend more or less parallel to the R^{3+} constants. This means that the chlorites were possibly formed at different times and geological contexts, as partly already guessed from the different compositions of the oxides. Within this cluster there are five different chlorites: those belonging to KBH1 and KBH6. The one that deviates the most is the *Blue Chl* from KBH1 (blue square in Fig. 6.1b), which has a temperature $T_{Blue\ Chl}$ =197±30°C; it follows a trend parallel to the R^{3+} line, in this case with a value of ≈2. The *Blue Chl* belongs to the fault and fracture with breccia/cataclasite clasts (e.g., KBH1-348, Fig. 5.19a) and is different from the *Brown Chl KBH1* (brown circle in Fig. 6.1b), of the breccias and cataclasites of sample KBH1-346, Fig. 5.16a); the latter chlorite formed at a higher temperature ($T_{Brown\ Chl\ KBH1}$=252±20°C), and is possibly associated with higher temperature fluids and a different geological event. The main difference between the two chlorites is the wt. % content of Al_2O_3 (*Brown Chl KBH1* 19.55 vs *Blue Chl* 16.01) and SiO_2 (*Brown Chl KBH1* 27.92 vs *Blue Chl* 28.94). Unfortunately, there are no samples with both chlorites, so the crosscutting relations between the two are uncertain; however, one could assume that the higher-temperature *Brown Chl KBH1* predates the lower-temperature *Blue Chl*. With regard to the sample KBH6-69, there are only the data of the *Dark Chl* (purple triangle in Fig. 6.1b), while those of *Bright Chl*, i.e., the chlorite with the highest FeO content ($FeO_{Bright\ Chl}$ =22.15±0.83 wt. %), are missing. The temperature of *Dark Chl* is 223±39°C. The fact that the geothermometer failed to calculate the *Bright Chl* analysis points could lead to the conclusion that it is a high-temperature chlorite and therefore it precedes the *Dark Chl*, which was reported in the diagram instead. Thus, *Bright Chl* is the

possibly the first type of chlorite associated with the alteration of the amphibolite basement. Finally, the last two classes belong to sample KBH6-72, that contains two types of chlorites: *Brown Chl KBH6* (red cross in Fig. 6.1b) and *Green Chl* (green rhombus in Fig. 6.1b). While they were quite different under the optical microscope because *Green Chl* has a lighter shade of green at parallel Nicols and therefore has a lower FeO content, looking at Figure 6.1b the two classes formed approximately at the same temperatures: $T_{\text{Brown Chl }KBH6}$=221±25°C and $T_{GreenChl}$=211±25°C. Again, the main difference between the two lies in the contents of Mg and Fe oxides, while in Si and Al the contents change by a maximum of one percentage point. However, a compositional distinction between the two chlorites can be seen in the diagram (different Si and R^{2+} values). In both KBH6-71 and KBH6-72 the *Green Chl* (lower in temperature) cuts the *Brown Chl KBH6* (higher in temperature) (Figure 5.19e). This suggest that in the studied are hotter deformation events precede the coldest ones. Finally, the temperatures of the *Brown Chl KBH6* and those of the *Dark Chl* are very similar.

- The second group comprises two classes both belonging to KBH7. The yellow in color squares in Fig. 6.1b correspond to *Fibrous Chl*, while the turquoise rhombuses in Fig. 6.1b correspond to *Rayed Chl*. Thanks to the microstructural study, it was observed that the *Fibrous Chl* cuts the *Rayed Chl*. In this case, too, the lines directed towards the pyrophyllite-gibbsite/Al-free chlorite line are observed. The two chlorites reflect the differences that were observed in Table 5.3: high MgO content, probably due to the proximity of the basaltic dyke, and low FeO lead to lower colour tones and no pleochroisms, low Al_2O_3 content and high SiO_2 allow for much lower temperatures than all the other chlorites. In the diagram, the two chlorites of KBH7 appear well separated because there is a clear compositional and temperature difference. The temperature of the *Rayed Chl* is 135±17°C, while for the *Fibrous Chl* it is 129°C±41°C. The large standard deviation of the latter chlorite is because some point analysis yielded very different temperature values. However, most of the analysis points yield an average temperature of 107°C. The fact that these chlorites, considering the

standard deviations, are the “coldest” in the studied area and were found in samples cored from similar depths (ca. 1400 m) support the hypothesis that the KBH7 chlorites formed at lower temperatures and possibly record the very recent deformation history in the area.

In Figure 6.2, I show the location of the wells in the Koyna region and the chlorites there are for each well with their calculated average temperatures and depths. In the caption, I show the figures in Chapter 5 that distinguish the various chlorites.

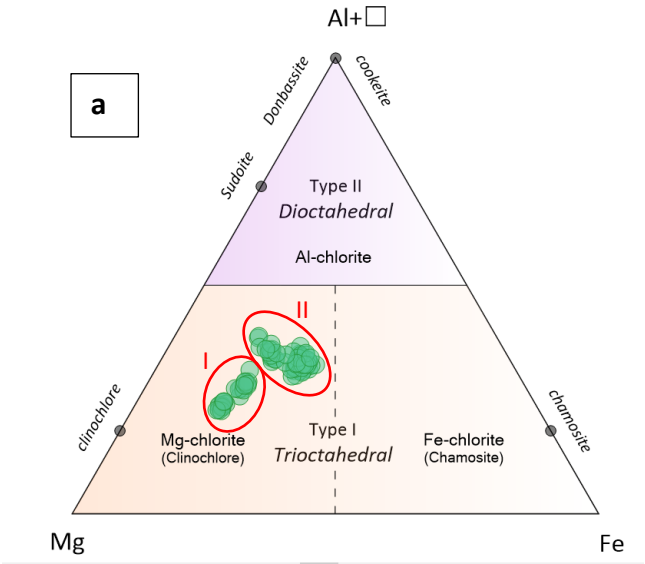

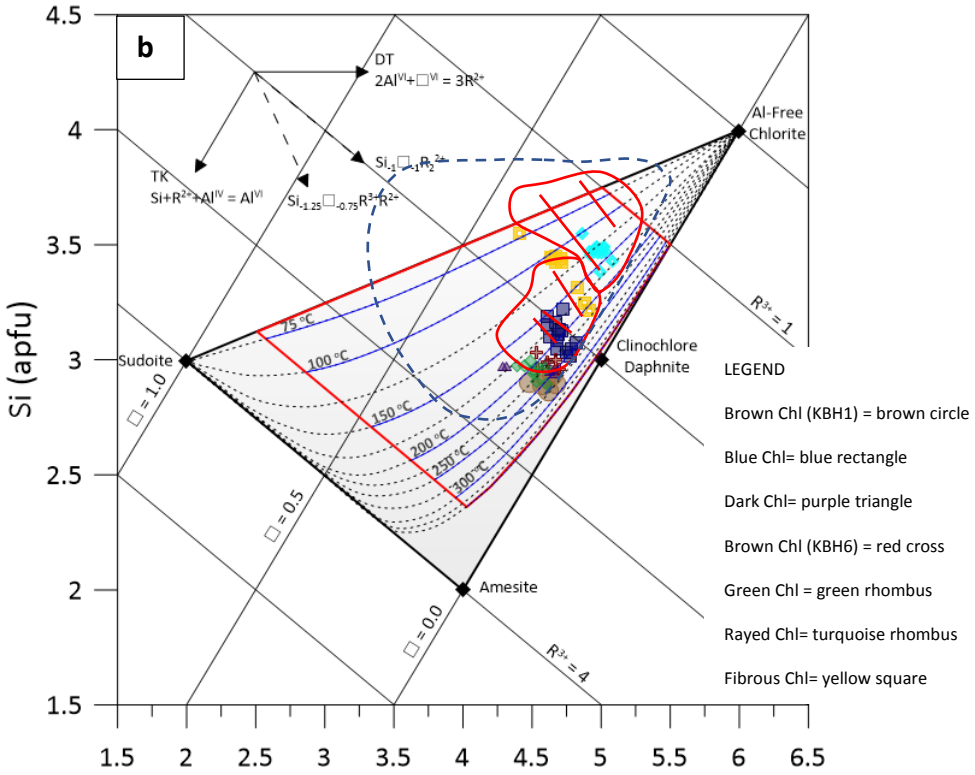

Figure. 6.1 a). diagram depicting chlorite end-members. All phyllosilicates in the samples belong to the Mg-chlorite class (clinochloro). Group I is less rich in Al, vice versa for group II; **b)** Representation of isotherms calculated with the thermometer of Bourdelle et al (2013), using the equation seen above, in the R^{2+}-Si diagram of Wiewióra and Weiss (1990). Seven different classes are observed, corresponding to the different chlorites. It is very noticeable that the two chlorites of KBH7, red circle in top left, have lower temperature than those of KBH1 and KBH6. The blue dashed area indicates the range of LT's chlorites and the red lines indicate the performance of each class. R^{2+} is refers to divalent cations (Fe^{2+} and Mg^{2+}), R^{3+} to trivalent cations (Al^{3+} and Fe^{3+}) and □ to vacancies. apfu= atoms per formula units.

SAMPLE	TYPE OF CHLORITE	TEMPERATURE (°C)	STANDARD DEVIATION
KBH1-346	Brown Chl KBH1	252	20
KBH1-348	Blue Chl	197	30
KBH6-69	Dark Chl	223	39
KBH6-71	Brown Chl KBH6	221	25
KBH6-71	Green Chl	211	25
KBH7-595	Rayed Chl	135	17
KBH7-595	Fibrous Chl	129	41

Table 6.1. Temperature and standard deviation of each chlorite type

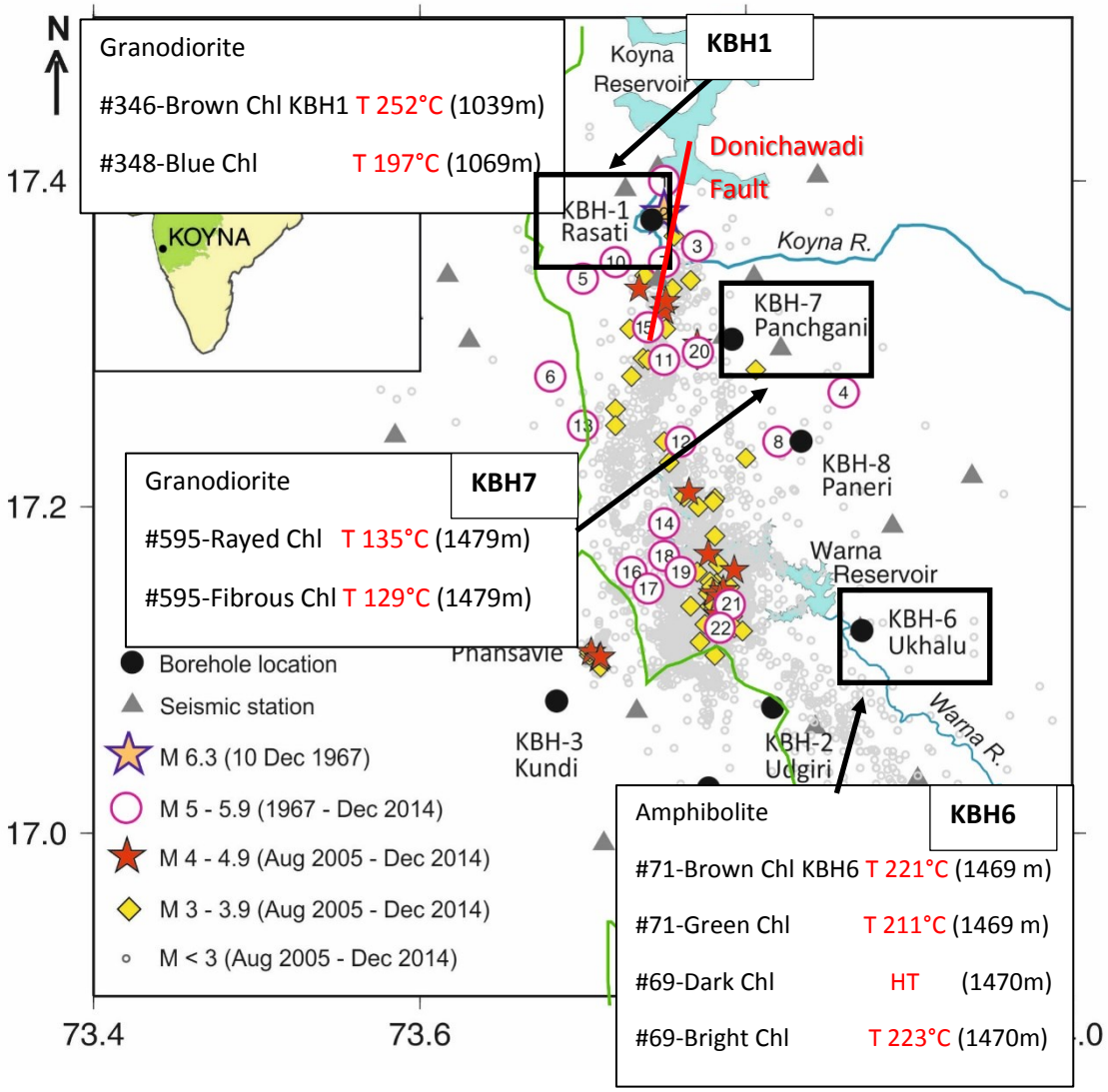

Figure 6.2. Koyna-Warna region where I list the types of chlorites with their respective temperatures and depths. Attached are pictures that best show the differences between the various chlorites: KBH1→Brown Chl KBH1 (Figure 5.16a), Blue Chl (Figure 5.19a); KBH6→Brown Chl KBH6 (Figure 5.19e), Green Chl (Figure 5.19e); KBH7→Rayed Chl (Figure 5.19g-h), Fibrous Chl (Figure 5.19g-h)

6.2. Sequence of deformation events

Thanks to the microstructural study, which made it possible to determine the cross-cutting relations between the various deformation structures (chapter 5.2), and the LT-chlorite geothermometer (chapter 6.1), which calculated the formation temperatures of the chlorites that composed the matrix of the breccia and cataclasites and of the veins that fill faults and fractures, it was possible to recognize the following sequence of deformation events:

1. Emplacement (ca. 2.71 ± 0.63 Ga) and alteration of the granodioritic and amphibolitic basement beneath Koyna-Warna region under green-schists to amphibolite facies conditions (Bhaskar Rao et al., 2017; Misra et al., 2022) (Figure 5.13a). Misra et al. (2022) recognizes a first ductile deformation phase (D_1) under amphibolite facies conditions;

2. "Ductile" deformation event occurred in green-schists facies possibly associated with the *Bright Chl* (e.g., KBH6 Figure 5.15). This event (D_2 in Misra et al., 2022) follows and overprints the primary foliation/deformation (D_1);

3. Emplacement of the Deccan magmatic province (68-60 Ma), that covered the Archaean basement. The magmatic underplating was associated with the initial rift flank uplift in the Western Ghat escarpment (Radhakrishna et al., 2019). As the main faults and fractures that cut the crystalline basement in the Koyna-Warna area are parallel to the WG, they may have formed at this stage;

4. "Brittle" deformation events characterised by the deformation structures described in Chapter 5.2.2. All of them cut the structural features associated with events 1 and 2. Instead, the relations of breccias and cataclasites, and faults and fractures filled by epidote and some types of chlorite-bearing veins with the emplacement of the Deccan traps (event 3) remains uncertain because of the lack in the studies samples of neat crosscutting relations between them. However, (1) the *Rayed* and *Fibrous Chl* cut a basaltic dyke of the Deccan Traps (Figure 5.19h), and (2) the calcite-bearing faults and fractures systematically cut

all the chlorite veins and the basaltic dykes (Figures 5.16a-b, 5.18m, 5.19h and 5.20) and therefore these deformation events (respectively 4.7 and 4.8 in the list below) are successive to the emplacement of the Deccan Traps.

The most common vein filling of "event 4" is chlorite. Other fillings include epidote, quartz and calcite. I report these late stage deformation events from the oldest to the most recent, assuming they occurred at decreasing temperatures, which is constrained by the temperature of formation/precipitation of the different types of chlorite (Figure 6.2):

4.1. Sub-vertical breccias and cataclasites with chlorite (*Brown Chl KBH1* type) matrix cutting the granodioritic basement of KBH1 ($T_{Brown\ Chl\ KBH1}$ =252±20°C) (Figures 5.9, 5.16a). The faults and fractures filled by chlorite-bearing veins that are sub-parallel to the breccias and cataclasites were possibly formed at the same time (Figure 5.19c, d). The breccias and cataclasites are cut by calcite-bearing veins (Figure 5.16a, see also Figure 6.3a for the proposed sequence of deformation events). Samples that record this deformation event were found at 1039-1153 m depth in KBH1 (samples -346, -347, -350, Figure 6.3b);

4.2. Breccias and cataclasites with epidote matrix probably formed before or at the same time of *Brown Chl KBH1* (Figure 5.16b, c). In these samples there are no veins filled with chlorite and so no relations can be made between the two deformation events. The breccias with epidote matrix is found at a greater depth (KBH1-353 → 1483 m depth) than those with a chlorite matrix. Breccias and veins with epidote matrix are cut by calcite-bearing veins (Figure 5.16b).

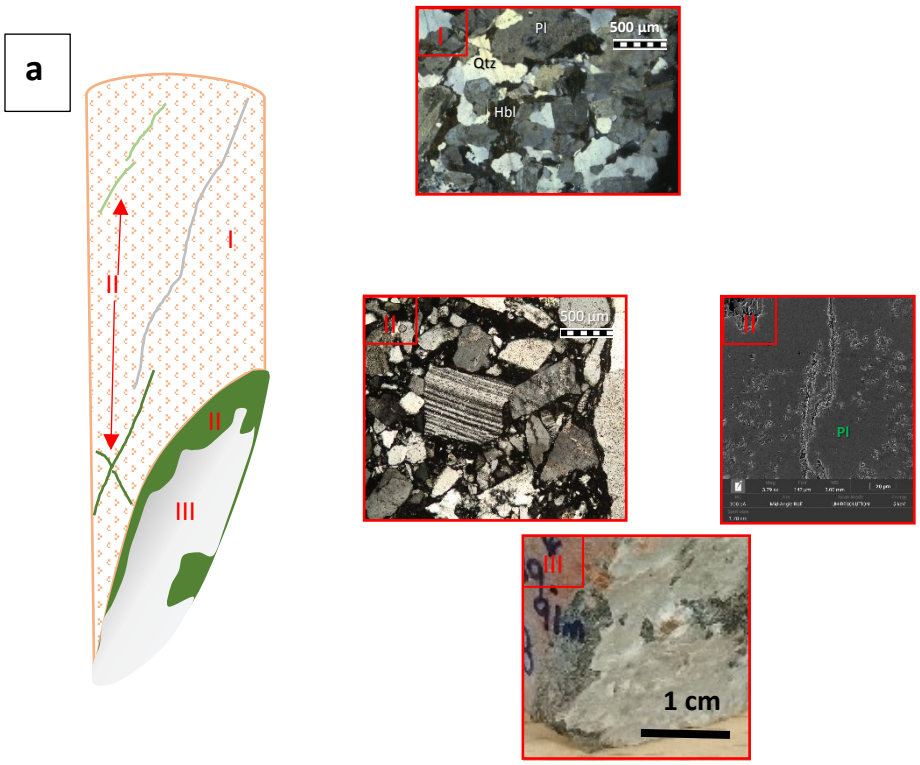
a
I
II
III
Pl
Qtz
Hbl
500 µm
1 cm

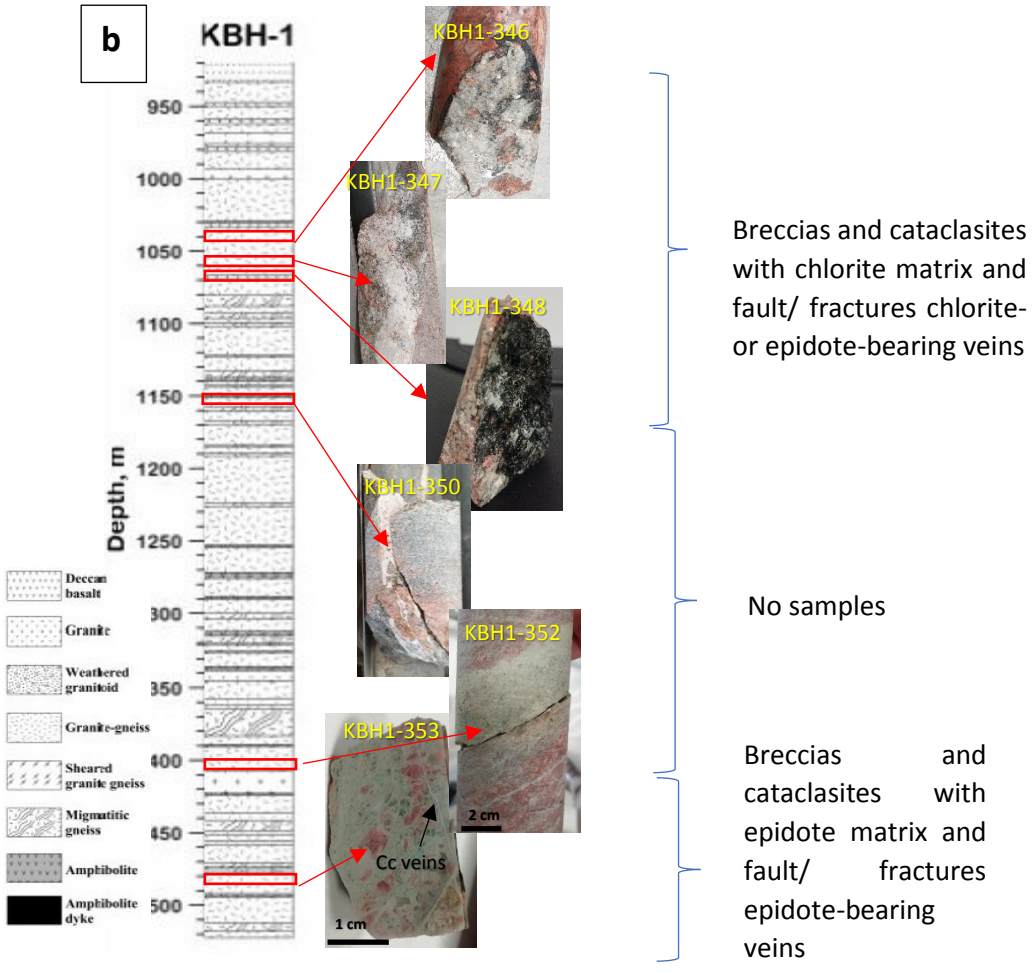
b
KBH-1
Depth, m
950
1000
1050
1100
1150
1200
1250
300
350
400
450
500
Deccan basalt
Granite
Weathered granitoid
Granite-gneiss
Sheared granite gneiss
Migmatitic gneiss
Amphibolite
Amphibolite dyke
KBH1-346
KBH1-347
KBH1-348
KBH1-350
KBH1-352
KBH1-353
Cc veins
2 cm
1 cm
Breccias and cataclasites with chlorite matrix and fault/ fractures chlorite- or epidote-bearing veins
No samples
Breccias and cataclasites with epidote matrix and fault/ fractures epidote-bearing veins

Figure 6.3 Possible sequence of deformation events (sample KBH1-346). **a)** (I) granodioritic basement; (II) breccias and cataclasites with *Brown Chl KBH1* and fault/ fractures chlorite-and epidote-bearing veins; (III) fault/ fractures calcite-bearing veins cut and the sub-vertical breccia; **b)** KBH1 well log with depth location of selected samples. From 1404 m borehole depth there are only breccias or epidote fault/fractures.

4.3. Breccias and cataclasites, and faults and fractures with *Brown/Dark Chl*-bearing veins cut the amphibolitic basement and overprint the ductile deformation (Figures 5.16f, 5.19b). The *Brown/Dark Chl* temperature of formation is 223±39°C;

4.4. Network of fault and fractures filled by quartz-bearing veins (Figure 5.18a) which cut the breccias and cataclasites, and the faults and fractures filled by *Brown/Dark Chl* veins. The *Brown/Dark Chl*-bearing veins (223±39°C) are cut by *Green Chl*-bearing veins (211±25°C) (Figure 5.18m);

4.5. Faults and fractures filled by *Green Chl* veins cut all the previous deformation events (Figures 5.18m, 5.19e). The *Green Chl* formation temperature is 211±25°C;

The succession of deformation events 4.3 to 4.5 is depicted in Figure 6.4.

Figure 6.4 Interpretation of the sequence of deformation events from sample KBH6-69 (Fig. 3.5f) **a)** mylonite formed in ductile event D_2 with the precipitation of *Bright Chl* (HT). Blue lines mark the foliation D_2; **b)** fault/fracture filled by *Dark/Brown Chl KBH6* veins overprint the mylonite. Quartz clasts are dissolved and associated with chlorite-titanite precipitation (dark green area and black lines respectively). **c)** same fault rock as in b cut by a fault/fracture filled by *Green Chl* vein (light green in color, see photo Fig. 5.19e). This latter includes fragments of the fault/fracture filled by *Brown Chl KBH6 vein*.

4.6. Sub-vertical fault/fractures filled by *Blue Chl* veins cutting the granodioritic basement of KBH1 with chlorite formation T=197±30°C (Figures 5.19a; 6.3b: samples stem from about 1070 m depth and include KBH1-348 and 349). The fractures filled by *Blue Chl* veins include small calcite grains (Figure 5.19f). This suggests that first (I) there was either a cementation of the calcite vein, which was reopened by a flow of fluid that shattered the calcite vein and then transported the small clasts, or the calcite grains precipitated along with the *Blue Chl* from the same fluid, and this was followed by (II) a second calcite vein which cut the *Blue Chl* vein (Figure 6.5). In addition, as in the case of breccias and cataclasites with *Brown Chl KBH1* matrix that are reactivated by faults/fractures filled by calcite veins (KBH1-346), the same applies to *Blue Chl*-bearing veins (Figure 6.3b, see the Appendix 1). This means that there were at least two calcite-bearing phases;

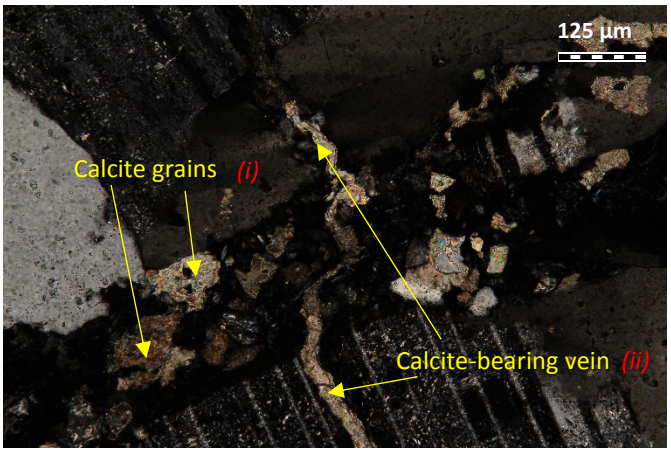

Figure 6.5. Same figure 5.19f but at crossed Nicols. (i) Calcite grains preceding or precipitated together with the *Blue Chl,* (ii) calcite-bearing vein cut the Blue Chl.

Brittle events 4.1 to 4.6 are associated with chlorite precipitation/formation temperatures ranging 197°C<T<252°C. Unfortunately, the relations between these chlorite-bearing faults/fractures with the emplacement of the Deccan Traps are unknown. However, the chlorite-bearing veins cut each other (Figure 6.4), indicating an abundance of percolation of fluids probably related to the emplacement of the Deccan Traps (Late Cretaceous) or successive. In the core samples, the breccias and cataclasites with *Brown Chl KBH1* or with epidote matrix are cohesive and more compact than the faults and fractures filled with the other type of chlorites (samples KBH1-346, 347, 350 Appendix 1). Thus, the *Brown Chl KBH1*, and the epidote precipitation, may pertain to deformation events that occurred before the emplacement of the Deccan Traps (event 3). Instead, the *Rayed* and *Fibrous Chl* have lower temperatures than the other chlorites and cut a basaltic dyke and are therefore syn- to post-emplacement of the Deccan Traps:

4.7. Very lower-temperature deformation events have been found only in the core KBH7 at a depth of 1476-1479 m. They are associated with breccias and cataclasites with *Rayed Chl* matrix (T=135±17°C) or *Fibrous Chl*-bearing veins (T=129±41°C). These two chlorites could have precipitated with calcite (Figure 5.19h);

4.8. The last deformation event concerns the fault and fracture filled by calcite veins which cut the other deformation structures described so far (Figures 5.16a-b, 5.17d, 5.18m, 5.19h and 5.20a to d). Some calcite-bearing veins cut and possibly are cut by *fibrous Chl-bearing veins* or the chlorites with the lowest formation temperature (T=129±41°C estimated so far in the cored samples).

In conclusion, most faults and fractures in the Koyna-Warna region are filled by chlorite- and calcite- bearing veins. Chlorite formed over a temperature range spanning from 252±20°C to 129±41°C, while calcite-bearing veins cut all the other deformation features.

6.3. Faults and fractures reactivated by Human-Induced Seismicity

A summary of the seismicity and geological setting in the Koyna-Warna region can be found in Chapters 1 to 3. The most relevant characteristics are:

1. The hypocentres of earthquakes are at a minimum depth of 3-4 km, especially in the Warna region, and a maximum of 13 km in the Koyna region (Rao & Shashidhar, 2016). Focal mechanisms and hypocentral relocation are consistent with normal and strike-slip faulting along sub-vertical faults (Figures 2.4 and 2.5);

2. The magnitude and frequency of seismic events is related to the variations of the water level in the reservoir with two responses: rapid, due to the increase in vertical stress associated with the impounding of the reservoir during the monsoon season and delayed due to the diffusion of fluid from the surface towards the hypocentral depths (Figure 2.8). Both rapid and delayed response are capable of reactivating pre-existing faults/fractures, although the delayed response is capable of generating larger in magnitude earthquakes (e.g., the 1967 Mw 6.3 earthquake, Gupta, 1992);

3. According to the geothermal model proposed by Ray et al. (2021), the thermal gradient ranges from 16 or 25 °C/km. Since earthquakes in the area usually nucleate between 4 and 10 km depth, the temperature at hypocentral depth ranges between 64-100°C and 160-250 °C.

After the mineralogical, microstructural and geochemical (including the geothermometer) studies, I came to the following conclusions:

1. The studied faults and fractures from the three wells (KBH1, KBH6 and KBH7) are sub-vertical. In addition, the abundance of the fractures in the vertical cores suggests that the Koyna-Warna region is heavily fractured;

2. The abundance of faults/fractures filled by chlorite and calcite precipitated by percolating fluids indicates the presence of a quite permeable basement. The fluids from the reservoirs pass through the joints that cut the Deccan and then through

the fractures in the basement, reaching the hypocentral depths. The presence of multiple episodes of calcite precipitation (Figure 5.20d) implies a fluid-valve behavior with possible relevant pore fluid transients (e.g., Sibson, 1990);

3. Breccias and cataclasites with chlorite matrix and fault/fractures are filled by chlorite-bearing veins with formation/precipitation temperature ranging from 129°C to 252°C (excluding *Bright Chl* which formed at higher temperature and is associated with a much older, possibly pre-Cretaceous, deformation stage). These chlorite-bearing veins are cut or reactivated by calcite-bearing veins. The 129°C to 252°C range fits within that of the estimated temperatures at hypocentral depths in the Koyna-Warna area.

I conclude that breccias and cataclasites with chlorite matrix and especially, because open and less cohesive, the faults and fractures filled by chlorite- and calcite-bearing veins are probably the structures reactivated by the human-triggered reservoir earthquakes in the area.

7. Conclusions and future studies

7.1 Conclusions

The Koyna-Warna region (20 x 30 km^2), about 300 km south of Bombay (India) is the world's best-known area of reservoir-triggered seismicity (RTS) (Figure 1.7). Since the first artificial reservoir impounding in 1962, the region, with very low natural seismicity, has been hit by 22 earthquakes above M 5, including the Koyna 1967 Mw 6.3 earthquake, probably the largest earthquake ever triggered by human activities, and by more than 100,000 recorded earthquakes. Seismicity is modulated by the monsoon rains which determine the reservoir impounding (rapid seismic response, from August to September) and emptying (delayed seismic response, from December to May) operations (Chapters 1 and 2, Figures 1.4 and 2.8). However, the information regarding the seismo-tectonic, structural and geological setting is poor and the mineralogical-petrological properties of the fault rocks unknown because the hypocenters (3-10 km depth) are all located within the inaccessible Proterozoic Indian crystalline basement buried 1-2 km beneath the late Cretaceous Deccan Traps (Figure 3.1). Because of this, the Koyna-Warna region has been the target of the largest International Continental (scientific) Drilling Project (ICDP) ever performed (Gupta, 2017b). The ICDP project included the drilling of nine deep boreholes, down to 1.5 km depth, used to install deep seismometers, strainmeters, temperature gages and other instrumentation to monitor the seismicity in the area, and to recover rock cores from almost hypocentral depths (Figure 2.14). Though this extraordinary scientific and technological effort, the mechanism of earthquake nucleation in the area remains unclear. Certainly the factors predisposing to the seismicity in the area include (1) the elastic strain storage cumulated in the intracratonic basement, (2) the pervasive network of pre-existing fractures/faults, (3) the presence of fluids percolating from the surface along the fault/fracture network, and (4) the stress variations induced by human activities in the reservoirs (Chapters 1.2, 2.1.2, 3.3). The deep drilling project provided the rock samples to address some of the main questions regarding the human-induced seismicity in the area. Seventeen samples of faults and fractures were selected by Prof. Giulio Di Toro and Dr. Elena Spagnuolo (INGV) during a visit in 2019 at the Scientific Core Repository of the ICDP project in Karad

(India). These samples from wells KBH1, KBH6 and KBH7 were subjected to mineralogical, geochemical and microstructural investigations in my thesis to obtain the following conclusions:

1. The Archean basement, topped by the Deccan Traps, is cut by sub-vertical faults/fractures. They have been divided into two groups:

(i) **Breccias and cataclasites** where clasts are in contact and the matrix/cement is made of chlorite, epidote or calcite;
(ii) **Faults and fractures filled by veins**: where the clasts are usually not in contact because of the high percentage of cement made by epidote, quartz, chlorite and calcite.

The widespread presence of late-stage faults/fractures filled by low-temperature (< 250°C) fluid-precipitated minerals highlights the relevance of fluid percolation in controlling the style of deformation in the area, including fault reactivation and human-induced seismicity.

2. The main mineralogical phases that fill the faults/fractures and veins are chlorite and calcite. There are at least seven types of chlorite based on chemical composition (WDS-FEG-SEM analysis, Ch. 5.3). The utilization of the chlorite geothermometer proposed by Bourdelle & Chatelineau (2015) allowed me to determine their formation temperatures (with the exception of the *Bright Chl* that probably formed at higher temperature: in fact, because of its composition, the LT geothermometer could not be applied). LT chlorites formed/precipitated in a temperature range spanning from 252°C to 129°C. Therefore, with the exception of *Brown Chl KBH1* which might be older (typical of the very cohesive breccias and cataclasites, see discussion in Chapter 6.2), the LT chlorite veining episode is syn- (197°C< T < 252°C) to post-emplacement (129°C <T <135°C) of the Deccan Traps. Faults and fractures filled by calcite-bearing veins cut all other deformation features and, as a consequence, are associated with the last and coldest brittle deformation events in the Koyna-Warna area.

3. Thanks to microstructural (crosscutting relations, Chapter 5.2), mineralogical and geochemical data (Chapter 5.1 & 5.3) and temperatures estimates (Chapter 6.1) I reconstructed the following sequence of deformation events:

(i) Archaean granodioritic and amphibolite basement (2.71±0.63 Ga, Bhaskar Rao et al., 2017), not discussed in the thesis;

(ii) Ductile deformation event with amphibolitic to greenschists facies mylonites (Misra eta al., 2022), not discussed in the thesis;

(iii) formation of the N-S striking fault/fractures, emplacement of the 1-2 km thick Deccan Traps (68-60 Ma, Hooper et al., 2010; Baksi, 2014; Schoene, et al., 2015), not discussed in the thesis;

(iv) Formation and reactivation of sub-vertical faults and fractures (68-0 Ma, discussed in this thesis). Their filling includes veins made of chlorite and calcite. In this late to post-Cretaceous evolution, there are at least two main events associated with chlorite precipitation, the first at 197°C< T< 252°C and the second at 129°C< T< 135°C. Both are cut by calcite-bearing fault/fractures veins.

4. Breccias and cataclasites and late-stage chlorite-, calcite-bearing veins formed in a temperature range of 129-252°C. The lower limit is based on chlorite composition, but these low temperature chlorite-bearing veins are cut by calcite veins. As a consequence, the lower temperature limit for fault reactivation could be lower. This temperature range overlaps with the one estimated at hypocentral depth (64-100°C < T< 160-250°C). Moreover, the hypocenters locations highlight the activation of sub-vertical structures, similar to those that were intercepted in the boreholes. We conclude that the current human-induced seismicity is taking place in similar faults/fractures filled by chlorite and calcite minerals precipitated by percolating and pressurized fluids.

7.2 Future studies

The samples I studied in this thesis belong to the wells drilled around the perimeter of the Koyna-Warna seismic area. The boreholes reached a maximum depth of 1.5 km and are therefore not suitable for studying earthquake hypocentral zones directly. The rock samples taken from the pilot borehole (KFD1) located near the Donichawadi fault, the one that caused the 1967 earthquake, should be analysed more closely because it reaches depths where the shallowest earthquakes originate (3 km). Clearly, it would be useful to carry out rock deformation experiments with the machines installed at Rock Mechanics Laboratory of the Department of Geosciences and at HP-HT laboratories at INGV-Rome to study the frictional properties, also in the presence of pressurized fluids, of the fault rock materials stem from these boreholes. Another interesting aspect would be to date the different growth phases of calcite and, thanks fluid inclusions and isotope studies, the fluid temperature and pressure of precipitation of the calcite-bearing veins. These studies would support any poroelastic model (e.g., delayed seismicity) of the human-induced earthquakes in the area.

References

Anderson, E. (1905). The dynamics of faulting. *Transactions of the Edinburgh Geological Society, 8*, 387-402.

Anuradha, M., & Malika, K. (2017). Reservoir Loading Parameters at Koyna and their Correspondence with Reservoir Triggered Seismicity. *JOURNAL GEOLOGICAL SOCIETY OF INDIA, 90*, 802-804.

Arora, K., Chadha, R., Srinu, Y., Selles, A., Davuluri, S., Smirnov, V., Mikhailov, V. (2017). Lineament Fabric from Airborne LiDAR and its Influence on Triggered Earthquakes in the Koyna-Warna Region, Western India. *JOURNAL GEOLOGICAL SOCIETY OF INDIA, 90*, 670-677.

Auden, J. B. (1949). Dykes in Western India. A discussion of their relationship with Deccan Traps. *Transactions of the Natural Institute of Science, India,, 3*, 123–137.

Bailey, S. (1988). Chlorites: structures and crystal chemistry. in ‘‘Hydrous Phyllosilicates (Exclusive of Micas)’’. *Rev. Mineral.*, 347–403.

Baksi, A. (2014). The Deccan Trap – Cretaceous–Paleogene boundary connection; new 40Ar/39Ar ages and critical assessment of existing argon data pertinent to this hypothesis. *Jour. Asian Earth Sci.,, 84*, 9–23.

Barbar, M., Kaplay, R., Mukherjee, S., & Kulkarni, P. (2017). *Evidence of the deformation of dykes from the Central Deccan Volcanic Province, Aurangabad, Maharashtra, India.* Retrieved from https://www.lyellcollection.org/.

Beane, J., Turner, C., Hooper, P., Subbarao, K., & Walsh, J. (1986). Stratigraphy, composition and form of the Deccan Basalts, Western Ghats, India. *Bull Volcanol, 48*, 61-83.

Bhaskar Rao, Y., Sreenivas, B., Vijaya Kumar, T., Khadke, N., Kesava Krishna, A., & Badu, E. (2017). Evidence for Neoarchean Basement for the Deccan Volcanic Flows around Koyna-Warna Region, Western India: Zircon U-Pb Age and Hf-isotopic Results. *JOURNAL GEOLOGICAL SOCIETY OF INDIA, 90*, 752-760.

Bilham, R., & Gaur, V. (2000). Geodetic contributions to the study of seismotectonics in India. *Curr. Sci., 79*, 1259-1269.

Bilham, R., Bendick, R., & Wallace, K. (2003). Flexure of the Indian plate and intraplate earthquakes. *Proc. Indian Acad. Sci. (Earth Planet. Sci.), 112*, 315-329.

Bodvarsson, G. (1970). Confined fluids as strain meters. *Jour. Geophys. Res., 75*, 2711-2718.

Bourdelle, F. (2021). Low-Temperature Chlorite Geothermometry and Related Recent Analytical Advances: A Review. *Minerals, 11, 130*.

Bourdelle, F., & Chatelineau, M. (2015). Low-temperature chlorite geothermometry: a graphical representation based on a T–R^{2+}–Si diagram. *Eur. J. Mineral., 27*, 617–626.

Bourdelle, F., Parra, T., Chopin, C., & Beyssac, O. (2013). A new chlorite geothermometer for diagenetic to low-grade metamorphic conditions. *Contrib. Mineral. Petrol., 165*, 723–735.

Brudy, M., Zoback, M., Fuchs, K., Rummel, F., & Baumgartner, J. (1997). Estimation of the complete stress tensor to 8 km depth in the KTB scientific drill holes: implications for crustal strength. *J. Geophys. Res., 102*, 18453–18475.

Cai, N., & Inoue, T. (2019). High-pressure and high-temperature stability of chlorite and 23-Å phase in the natural chlorite and synthetic MASH system. *Comptes Rendus Geoscience, 351*, 104-112.

Cathelineau, M., & Nieva, D. (1985). A chlorite solid solution geothermometer. The Los Azufres (Mexico) geothermal system. *Contrib. Mineral. Petrol., 91*, 235–244.

Chadha, R., Kuempel, H., & Shekar, M. (2008). Reservoir Triggered Seismicity (RTS) and well water level response in the Koyna–Warna region, India. *Tectonophysics, 456*, 94–102.

Chadha, R., Srivastava, K., & Kuempel, H. (2005). Earthquake related changes in well water level and their relation to a static deformation model for the seismically active Koyna–Warna region, India. *Oxford & IBH Publishing*, 135-150.

Deer, W., Howie, R., & Zussman, J. (1994). *Introduzione ai minerali che costituiscono le rocce.* Bologna: Zanichelli.

Deere, D. U. (1963). Technical description of rock cores for engineering purposes. In Rock mechanics and engineering geology. *Felsmechanik und Ingenieurgeologie (Rock Mechanics and Engineering Geology), 1*, 16-22.

Deshmukh, S., & Sehgal, M. (1988). Mafic dyke swarms in Deccan volcanic province of Madhya Pradesh and Maharashtra. *Geological Society of India, Memoirs, 10*, 323–340.

Deshpande, A., & Mohan, G. (2016). Seismic evidence of crustal heterogeneity beneath the northwestern Deccan volcanic province of India from joint inversion of Rayleigh wavedispersion measurements and P receiver functions. *Jour. Asian Earth Sci., 128*, 54–63.

Dessai, A., Markwick, A., Vaselli, O., & Downes, H. (2004). Granulite and pyroxenite xenoliths from the Deccan Trap: insight into the nature and composition of the lower lithosphere beneath cratonic India. *Lithos, 78*, 263–290.

Dessert, C., Dupré, B., François, L., Schott, J., Gaillardet, J., Chakrapani, G., & Bajpai, S. (2001). Erosion of Deccan Traps determined by river geochemistry: impact on the global climate and the 87Sr/86Sr ratio of seawater. *Earth Planet. Sci. Lett., 188*, 459–474.

Durà-Goméz, I., & Talwani, P. (2009). Hydromechanics of the Koyna–Warna Region, India. *Pure Appl. Geophys.*

Duraiswami, R., & Karmalkar, N. (1996). Unusual xenolithic dyke at Mandaleshwar and its episodic nature. *Gondwana Geol. Magz., 11*, 1-10.

Foulger, G., Wilson, M., Gluyas, J., Julian, B., & Davies, R. (2018). Global review of human-induced earthquakes. *Earth-Science Reviews, 178*, 438–514.

Gaina, C., Muller, R., Brown, B., & Ishihara, T. (2003). Microcontinent formation around Australia, in Evolution and Dynamics of the Australian Plate. *Spec. Pap. Geol. Soc. Am.*, 405–416.

Gaina, C., Muller, R., Brown, B., Ishihara, T., & Ivanov, S. (2007). Breakup and early seafloor spreading between India and Antarctica. *Geophys. J. Int., 170*, 151–169.

Goswami, D., Akkiraju, V., Misra, S., Roy, S., Singh, S., Sinha, A., Nayak, S. (2017). Rock strength measurements on Archaean basement granitoids recovered from scientific drilling in the active Koyna seismogenic zone, western India. *Tectonophysics, 712-713*, 182–192.

Goswami, D., Hazarika, P., & Roy, S. (2020). In Situ Stress Orientation From 3 km Borehole Image Logs in the Koyna Seismogenic Zone, Western India: Implications for Transitional Faulting Environment. *Tectonics, 39*.

Gowd, T., Srirama Rao, S., & Gaur, V. (1992). Tectonic stress filed in the India subcontinent. *J. Geophys. Res., 97*, 11879-11888.

Gravilenko, P., Singh, C., & Chadha, R. (2010). Modelling the hydromechanical response in the vicinity of the Koyna reservoir (India): results for the initial filling period. *Geophys. J. Int., 183*, 461–477.

Guha, S., Gosavi, P., Varma, M., Agrawal, S., Padale, J., & Marwadi, S. (1968). Recent seismic disturbances in the Koyna Hydroelectric Project. Central Water and Power Research Station, Maharashtra.

Gupta. H.K., (1992). *Reservoir Induced Earthquakes.* Amsterdam: Elseveir.

Gupta, H.K., (2002). A review of recent studies of triggered earthquakes by artificial water reservoirs with special emphasis on earthquakes in Koyna, India. *Earth Science Reviews, 58*, 279-310.

Gupta HK, et al. (2014). Probing reservoir-triggered earthquakes in Koyna, India, through scientific deep drilling. *Sci. Dril., 18*, 5-9.

Gupta, H.K., (2017b). Koyna, India, an Ideal site for Near Field Earthquake Observations. *JOURNAL GEOLOGICAL SOCIETY OF INDIA, 90*, 645-652.

Gupta, H.K., & Nayak, S. a. (2011). Deep Scientific Drilling to Study Resevoir-Triggered Earthquake in Koyna, Western India. *Scientific Drilling*, 1-2.

Gupta, H.K., & Rastogi, B. (1976). *Dams and Earthquakes.* Amsterdam: Elsevier.

Gupta, H.K., Narain, H., Rastogi, B., & Mohan, I. (1969). A study of the Koyna earthquak of December 10, 1967. *Bulletin of the Seismological Society of America, 59*, 1149-1162.

Gupta, H.K., Rama Krishna Rao, C., Rastogi, B., & Bhatia, S. (1980). An investigation of earthquakes in Koyna region, Maharashtra, for the period October 1973 through December 1976. *Bulletin of the Seismological Society of America, 70*, 1833-1847.

Gupta, H.K., RAO, R., Srinivasan, R., Rao, G., & Reddy, G. (1999). Anatomy of surface rupture zones of two stable continental regione arthquakes1, 967K oyna and 1993L atur, India. *GEOPHYSICAL RESEARCH LETTERS, 26*, 1985-1988.

Gupta, H.K., Shashidhar, D., Mahato, C., Satyanarayana, H., Mallika, K., RAO, N., Navitha, K. (2017a). Location of the pilot borehole for investigations of reservoir triggered seismicity at Koyna, India. *Gondwana Research, 42*, 133-139.

Gupta H.K., Rastogi, B., & Narain, H. (1972b). Some discriminatory characteristics of earthquakes near the Kariba, Kremasta and Koyna artificial lakes. *Bull. Seismol. Soc. Am.*, 493-507.

Gupta H.K., Ratogi, B., & Narain, H. (1972a). Common features of the reservoir associated seismic activities. *Bull. Seismol. Soc. Am., 62*, 481-492.

Gupta H.K., N. Purnachandra Rao, Sukanta Roy · Kusumita Arora · V. M. Tiwari · Prasanta K. Patro · H. V. S. Satyanarayana · D. Shashidhar · K. Mallika · Vyasulu V. Akkiraju · Deepjyoti Goswami et al. (2015). Investigations related to scientific deep drilling to study reservoir-triggered earthquakes at Koyna, India. *Int J Earth Sci, 104*, 1511–1522.

Harpster, R., Cluff, L., & Lovegreen, J. (1979). Active faulting in the Deccan Plateau near Koyna Nagar, India. *Geol. Soc. Am., Abstr. Prog., 11 (7)*, 438-439.

Hazarika, P., Yadav, A., & Roy, S. (2017). Influence of Permeability in Modeling of Reservoir Triggered Seismicity in Koyna Region, Western India. *JOURNAL GEOLOGICAL SOCIETY OF INDIA, 90*, 728-732.

Hillier, S., & Velde, B. (1991). Octahedral occupancy and the chemical-composition of diagenetic (low-temperature) chlorites. *Clay Miner., 26*, 149–168.

Holland, T., Baker, J., & Powell, R. (1998). Mixing Properties and Activity-Composition Relationships of Chlorites in the System MgO-FeOFeOAl2O3-. *Eur. J. Mineral., 10*, 395–406.

Hooper, P., Widdowson, M., & Kelley, S. (2010). Tectonic setting and timing of the final Deccan flood basalt eruptions. *Geology, 38*, 839–842.

Inoue, A., Meunier, A., Patrier-Mas, P., Rigault, C., Beaufort, D., & Vieillard, P. (2009). Application of chemical geothermometry to low-temperature trioctahedral chlorites. *Clays Clay Miner., 57*, 371–382.

Jadhav, P., & Lalitkumar, K. (2017). Tectonic Geomorphology in Parts of Koyna Region, Maharashtra. *JOURNAL GEOLOGICAL SOCIETY OF INDIA, 90*, 738-741.

Kaila, K., Murthy, P., Rao, V., & Kharetchko, G. (1981). Crustal structure from deep seismic soundings along the Koyna II (KELSI KELSILoni) profile in the Deccan trap area, India. *Tectonophysics, 73*, 365-384.

Kaila, K., Murthy, P., Rao, V., & Kharetchko, G. (1981). Crustal structure from deep seismic soundings along the Koyna II (KELSILoni) profile in the Deccan trap area, India. *Tectonophysics, 73*, 365-384.

Kalpna, R., & Chander, R. (2000). Green's function based stress diffusion diffusion solutions in the porous elastic half space for time varying finite reservoir loads. *Phys. Earth Planet. Inter., 120*, 93-101.

Keranen, K., Weingarten, M., Abers, G., Bekins, B., & Ge, S. (2014). Sharp increase in central Oklahoma seismicity since 2008 induced by massive wastewater injection. *Science, 345*, 448-451.

King, G., & Bilham, R. (1973). Strain measurement instrumentation and technique. *Philosophical transactions of the Royal Society of London,, 274*, 209-217.

Krishna, V., Kaila, K., & Reddy, P. (1989). Synthetic seismogrammodeling of crustal seismic record sections from the Koyna DSS profiles in the western India, in properties and processes of Earth's lower crust. *Am. Geophys. Union Monogr, 51*, 143-157.

Kruhl, J. (1996). Prism- and basal-plane subgrain boundaries in quartz; a microstructural geotehermobarometer. *J Metam Geol, 14*, 581-589.

Kuempel, H. (1992). About the potential of wells to reflect stress variations within inhomogeneous crust. *Tectonophysics, 211*, 317–336.

Kuempel, H., Chadha, R., Ramana, D., & Ravi, M. (2017). In-situ Pore Pressure Variations in Koyna-Warna – A Promising Key to Understand Triggered Earthquakes. *JOURNAL GEOLOGICAL SOCIETY OF INDIA, 90*, 678-683.

Kuamr Shukla, M., Vishnu, C., & Roy, S. (2022). Petrographic and geochemical characteristics of the granitic basement rocks below Deccan Traps obtained from scientiBc drilling to 3014 m depth in the Koyna region, western India. *J. Earth Syst. Sci.*

Lanari, P., Wagner, T., & Vidal, O. (2014). A thermodynamic model for di-trioctahedral chlorite from experimental and natural data in the system MgO–FeO–Al_2O_3–SiO_2–H_2O: applications to P–T sections and geothermometry. *Contrib. Mineral. Petrol., 167*, 968–xxx.

Langston, C. (1981). Source inversion of seismic wave form: The Koyna India earthquake of 13, September 1967. *Bull. Seismol. Soc. Am., 71*, 1-24.

Mainprace, D., & Nicolas, A. (1989). Development of shape and lattice preferred orientations: application to the seismic anisotropyof the lower crust. *J. Struct Geol, 11*, 175-190.

McDowell, S., & Elders, W. (1980). Authigenic layer silicate minerals in borehole Elmore 1, Salton Sea geothermal field, California, USA. *Contrib. Mineral. Petrol., 74*, 293–310.

McGarr, A., & Simpson, D. (1997). *Keynote lecture: A broad look at induced and triggered seismicity, ‘‘Rockbursts and seismicity in mines’’.* (S. L. In: Gibowicz, Ed.) Balkema, Rotterdam: Proc. of 4th Int. Symp.

Melluso, L., Sethna, S., Morra, V., Khateeb, A., & Javeri, P. (1999). Petrology of the mafic dyke swarm of the Tapti River in the Nandurbar area (Deccanvolcanic province). *Geological Society of India, Memoirs, 43*, 735–755.

Mishra, S., Misra, S., Vyas, D., Nikalje, D., Warhade, A., & Roy, S. (2017). A 1251m-thick Deccan Flood Basalt Pile Recovered by Scientific Drilling in the Koyna Region, Western India. *JOURNAL GEOLOGICAL SOCIETY OF INDIA, 90*, 788-794.

Misra, S., Bartakke, V., Athavale, G., Akkiraju, V., Goswami, D., & Roy, S. (2017). Granite-gneiss Basement below Deccan Traps in the Koyna Region, Western India: Outcome from Scientific Drilling. *JOURNAL GEOLOGICAL SOCIETY OF INDIA, 90*.

Misra, S., Goswami, D., & Roy, S. (2022). Mineralogy and structures below Deccan Traps: Evidences from scientiBc drilling in the Koyna seismogenic zone, India. *J. Earth Syst. Sci.*, 131:149.

Mogi, K. (1963). Experimental study on the mechanism of the earthquake occurebces of volcanic origin. *Eartquake Research Institute, University of Tokyo*.

Muir-Wood, R., & King, G. (1993). Hydrological signatures of earthquake strain. *Jour. Geophys. Res., 98*, 22,035–22,068.

Pandey, O., Vedanti, N., Srivastava, R., & Uma, V. (2013). Was Archean Dharwar Craton Ever Stable? A Seismic Perspective. *JOURNAL GEOLOGICAL SOCIETY OF INDIA, 81*, 774-780.

Pascoe, E. (1964). *A Manual of the Geology of India and Burma* (Vol. vol. 3). Calcutta: Government of India Press.

Passchier, C. (1892). Mylonitic deformation in the Saint-Barthelemy Massif, French Pyrenees, with emphasisob the genetic relationship between ultramylonite and pseudotachylyte. *GUA Pap Geol Ser, 1 16*, 1-173.

Passchier, C., & Trouw, R. (2005). *Microtectonics* (Vol. 2). Springer Science & Business Media.

Paul, J., Burgmann, R., Gaur, V., Bilham, R., Larson, K., Ananda, M., . . . Kumar, D. (2001). The motion and active deformation of India. *Geophys. Res. Lett., 28*, 647-651.

Praveen Kumar, K., & Mohan, G. (2014). Crustal velocity structure beneath Saurashtra, NW India, through waveform modeling: Implications for magmatic underplating. *Jour. Asian Earth Sci., 79*, 173–181.

Radhakrishna, T., Asanulla, R., Venkateshwarlu, M., Soumya, G., & Prachiti, P. (2019). Mechanism of rift flank uplift and escarpment formation evidenced by Western Ghats, India. *Scientific Reports*.

Rai, S. (1999). What triggers Koyna region earthquakes? Preliminary results from seismic tomography digital array. *Earth Planet. Sci., 108*, 1-14.

Rajendran, K., Harish, C., & Kumaraswamy, S. (1996). Re-evaluation of earthquake data from Koyna–Warna region: Phase I. *Report to the Department of Science and Technology*, 94.

Rao, K., Ravi Kumar, M., & Rastogi, B. (2015). Crust beneath the northwestern Deccan Volcanic Province, India: evidence for uplift and magmatic underplating. *Jour. Geophys. Res., 120*, 3385–3405.

Rao, N., & Shashidhar, D. (2016). Periodic variation of stress field in the Koyna–Warna reservoir triggered seismic zone inferred from focal mechanism studies. *Tectonophysics, 679*, 29-40.

Rao, N., & Shashidhar, D. (2017). Earthquake Focal Mechanism Studies in Koyna-Warna Region in the Last Five Decades – Current Understanding on Tectonics and Seismogenesis. *JOURNAL GEOLOGICAL SOCIETY OF INDIA, 90*, 684-691.

Rao, N., Roy, S., & Arora, K. (2013). Deep scientific drilling in Koyna, India – brainstorming workshop on geological investigations 19–20 March 2013. *Jour. Geol. Soc. India, 81*, 722–723.

Rastogi, B. (2017). Migration of Seismicity and Pore Pressure Diffusion for Five Decades Long Koyna–Warna Sequence and Precursory Nucleation Process for Earthquake Forecasting. *JOURNAL GEOLOGICAL SOCIETY OF INDIA, 90*, 698-703.

Rastogi, B., Chadha, R., Sarma, C., Mandal, P., Satyanarayana, H., Raju, I., . . . Nageswara Rao, A. (1997). Seismicity at Warna reservoir (near Koyna) through 1995. *BSSA, 87*, 1484–1494.

Rastogi, Chadha, R., & Sarma, C. (1995). Investigations of June 7, 1988 earthquake of Magnitude 4.5 near Idukki dam in southern India. *PAGEOPH, 145*, 109-122.

Ray, L., Kumar Gupta, R., Chopra, N., Gopinadh, D., & Kumar Dwivedi, S. (2021). Thermal and Physical Properties of Deccan Basalt and Neoarchean Basement Cores From a Deep Scientific Borehole in the Koyna−Warna Seismogenic Region, Deccan Volcanic Province, Western India: Implications on Thermal Modeling and Seismogenesis. *Earth and Space Science*.

Ray, R., Sheth, H., & Jyotirmoy, M. (2007). Structure and emplacement of the Nandurbar-Dhule mafic dyke and emplacement of the Nandurbar-Dhule mafic dyke of fluid basalts. *Bulletin of Volcanology, 69*, 537–551.

Reddy, D., Kumar, D., & Rao, N. (2017). Long-term Hydrochemical Earthquake Precursor Studies at the Koyna-Warna Reservoir Site in Western India. *JOURNAL GEOLOGICAL SOCIETY OF INDIA, 90*, 720-727.

Roeloffs, E. (1988). Fault stability changes induced beneath a reservoir with cyclic variations in water level. *J. Geophys. Res., 83*, 2107–2124.

Roy, S., Rao, N., Akkiraju, V., Goswami, D., Sen, M., Gupta, H., . . . Nayak, S. (2013). Granitic basement below Deccan Traps unearthed by drilling in the Koyna Seismic Zone, western India. *Jour. Geol. Soc. India, 81*, 289-290.

Sain, K., Zelt, C., & Reddy, P. (2002). Imaging of subvolcanic mesozoics in the Saurashtra peninsula of India using travel time inversion of wideangle seismic data. *Geophys. Jour. Internat, 150*, 820–826.

Sakar, D., & Sain, K. (2017). Deep Seismic Sounding Experiments in the Koyna RTS Region: An Overview of the Results. *JOURNAL GEOLOGICAL SOCIETY OF INDIA, 90*, 663-669.

Sano T. et al. (2001). Differentiayion Proceses of Deccan Traps Basalts: Contribution from Geochemistry and Experimental Petrology. *Journal of Petrology, 42*, 2175-2195.

Sarma, P., & Srinagesh, D. (2007). Improved earthquake locations in the Koyna-Warna seismic zone. *Nat. Hazards, 40*, 563-571.

Schoene, B., SampertonK. Y., Eddy, M., Keller, G., Adatte, T., & Bowring, S. (2015). U-Pb geochronology of the Deccan traps and relation to the end-Cretaceous mass extension. *Science, 347*, 182–184.

Scholz, C. (2019). *The Mechanics of Earthquakes and Faulting* (Third Edition ed.). New York: Cambridge University press.

Schultz, R., Ellsworth, W., & Beroza, G. (2022). Statistical bounds on how induced seismicity stops. *Scientific Reports*.

Sen, G., & Chandrasekharam, D. (2011). *Deccan Traps Flood Basalt Province: An Evaluation of the Thermochemical Plume Model.* Dordrecht: Springer.

Shashidhar, D., Mallika, K., Rao, N., Satyanarayana, H., & Gupta, H. (2014). Detection of quarry blasts in the Koyna–Warna region, western India. *Open J. Earthquake Res., 3*, 162–169.

Shashidhar, D., Rao, N., & Gupta, H. (2011). Waveform inversion of local earthquakes using broad band data of Koyna–Warna region,western India. *Geophys. J. Int., 185*, 292–304.

Sheth, H., & Cañón-Tapia, E. (2015). Are flood basalt eruptionsmonogenetic or polygenetic? *Int. J. Earth Sci., 104*, 2147–2162.

Sibson, R. (1990). Conditions for fault-valve behaviour. *Geology, 54*, 15-28.

Simpson, D., Leith, W., & Scholz, C. (1988). TWO TYPES OF RESERVOIR-INDUCED SEISMICITY. *Bulletin of the Seismological Society of America, 78*, 2025-2040.

Sinha, D., Som, A., & Roy, S. (2017). The Subsurface Megascopic Characteristics of Basalt and Basement Rocks from Koyna-Warna Area of Maharashtra, India. *JOURNAL GEOLOGICAL SOCIETY OF INDIA, 90*, 761-768.

Snow, D. (1972). *Geodynamics of seismic reservoirs.* Stuttgart: Proc. Symp.Percolation through Fissured Rocks.

Stripp, M., Stunitz, H., Heilbronner, R., & Schmid, S. (2002). The eastern Tonale fault zone: a "natural laboratory" for crystal plastic deformation of quartz over a temperature range from 250 to 700°C. *J Struct Geol, 24*, 1861-1884.

Subbarao, K., & Courtillot, V. (2017). Deccan Basalts in and around Koyna – Warna Region, Maharashtra: Some Reflections. *JOURNAL GEOLOGICAL SOCIETY OF INDIA, 90*, 653-662.

Subrahmanya, K. (1998). Tectono-magmatic evolution of the western coast of India. *Gondwana Research, 1*, 319-327.

Talwani. (1997a). Seismotectonics of the Koyna–Warna area, India. *Pure Appl. Geophys., 150*, 511-550.

Talwani. (1997b). On the nature of reservoir-induced seismicity. *Pure Appl. Geophys., 150*, 473-492.

Talwani, P. (1995). Speculation on the causes of continuing seismicity near Koyna Reservoir, India. *PAGEOPH, 145*, 167–174.

Talwani, P., & Acree, S. (1985). Pore pressure diffusion and the mechanism of reservoir induced seismicity. *Pure Appld. Geophys., 122*, 947-965.

Talwani, P., Kumara Swamy, S., & Sawalwade, C. (1996). Koyna Revisited: The Reevaluation of Seismicity Data in the Koyna-Warna Area. *Univ. South Carolina Tech. Report (Columbia, South Carolina)*, 343.

Townend, J., & Zoback, M. (2000). How faulting keeps the crust strong. *Geology, 28*, 399-402.

Tripathi, P., Pandey, O., Rao, M., & Reddy, G. (2012). Elastic properties of amphibolite and granulite facies mid-crustal basement rocks of the Deccan volcanic covered 1993 Latur-Killari earthquake region, Maharashtra (India) and mantle metasomatism. *Tectonophysics, 554-557*, 159–168.

Upadhyay, D., Koojiman, E., Singh, A., Mezger, K., & Berndt, J. (2015). The Basement of the Deccan Traps and Its Madagascar Connection: Constraints from Xenoliths. *Jour. Geol., 123*, 295-307.

Vaidyanadhan, R., & Ramakrishnan, M. (2010). *Geology of India.* Bangalore: Geol. Soc. India.

Valdiya, K. (1984). *Aspects of Tectonics: Focus on South-Central Asia.* New Delhi: McGraw-Hills.

Valdiya, K. (2010). *The making of India - Geodynamic evolution.* Macmillan.

van Hinsbergen, D., Steinberger, B., Doubrovine, P., & Gassmöller, R. (2011). Acceleration and deceleration of India-Asia convergence Acceleration and deceleration of India-Asia convergence since the Cretaceous: Roles of mantle plumes. *JOURNAL OF GEOPHYSICAL RESEARCH,, 116*.

Vanderkluysen, L., Mahoney, J., Hooper, P., Sheth, H., & Ray, R. (2011). The feeder system of the Deccan Traps (India): insights from dyke geochemistry. *Journal of Petrology, 52*, 315–343.

Vidal, O., Parra, T., & Trotet, F. (2001). *Am. J. Sci., 301*, 557–592.

Vidal, O., Parra, T., & Vieillard, P. (2005). Thermodynamic properties of the Tschermak solid solution in Fe-chlorite: Application to natural examples and possible role of oxidation. *Am. Mineral., 90*, 347–358.

Walker, G. (1972). Compound and Simple Lava Flows and Flood Basalts. *Imperial College. London, SW7 2BP*.

White, L., & Lister, G. (2012). The collision of India with Asia. *Journal of Geodynamics, 56-57*, 7-17.

Wiewiora, A., & Weiss, Z. (1990). Crystallochemical classifications of phyllosilicates based on the unified system of projection of chemical composition: II The chlorite group. *Clay Miner., 25*, 83–92.

Wilson, M. P. (2017). HiQuake: the Human-Induced Earthquake Database. *Bull. Seismol. Soc. Am. (submitted)*.

Woodcock, N., & Mort, K. (2008). Classification of fault breccias and related fault rocks. *Geol. Mag., 145*, 435-440.

Yavuz, F., Kumral, M., Karakaya, N., Karakaya, M., & Yıldırım, D. (2015). A Windows program for chlorite calculation and classification. *Computers & Geosciences, 81*, 101-113.

Zoback, M., & Healy, J. (1984). Friction, faulting, and insitu stress. *Ann. Geophys., 2*, 689-698.

Appendixes

Appendix 0. Techniques

Techniques applied the samples studied in the thesis.

Sample	Thin section	XRPD	UH Resolution and Analysis Image (FEG-SEM)	WDS Analysis
KBH1_346	x	x		x
KBH1_347	x	x		
KBH1_348	x			x
KBH1_349	x	x		
KBH1_350	x	x	x	
KBH1_351	x	x	x	
KBH1_352	x	x	x	
KBH1_353	x			
KBH6_67	x	x	x	
KBH6_68	x	x		
KBH6_69	x	x		x
KBH6_70	x	x	x	
KBH6_71	x	x		x
KBH6_72	x	x		
KBH6_73	x	x		
KBH7_594	x	x	x	
KBH7_595	x	x	x	x

Appendix 1: Rock samples

Photo of the studied samples of my thesis.


KBH1-349


KBH1-350
2 cm


KBH1-351
2 cm


KBH1-352
2 cm


2 cm
KBH1-353


2 cm
KBH6-69

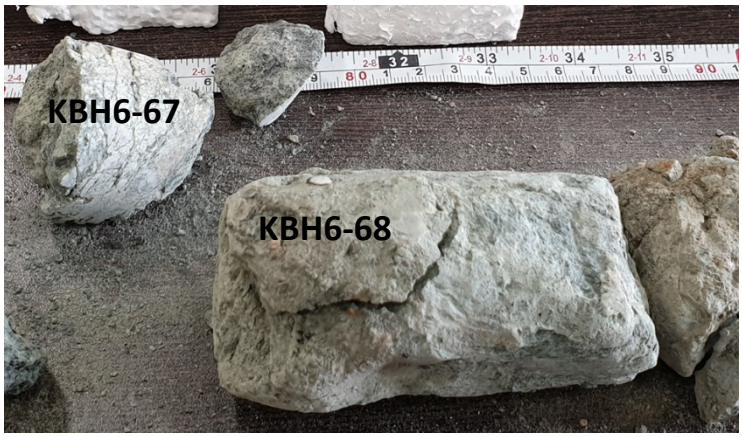
KBH6-67
KBH6-68

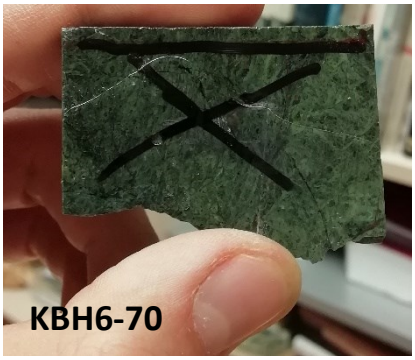
KBH6-70

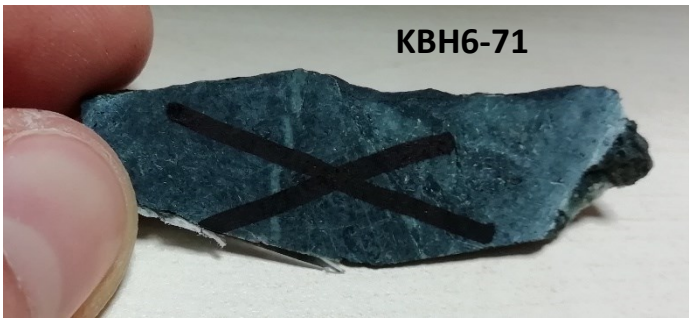
KBH6-71


KBH6-72


2 cm
KBH6-73


KBH7-594
2 cm


KBH7-595
2 cm

Appendix 2. XRPD spectra

X-Ray powder diffraction spectra of all the samples.

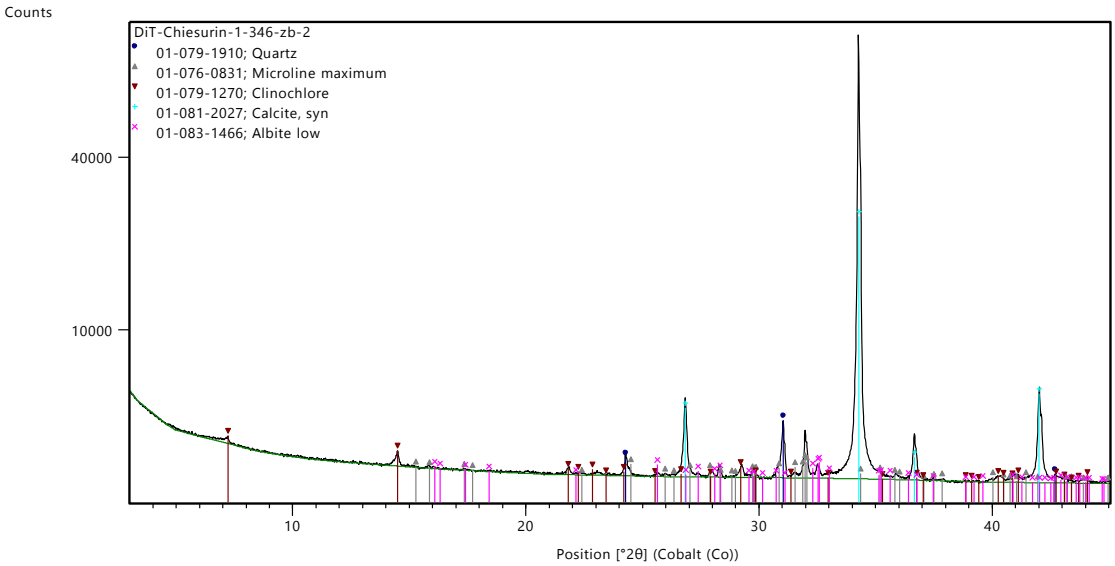

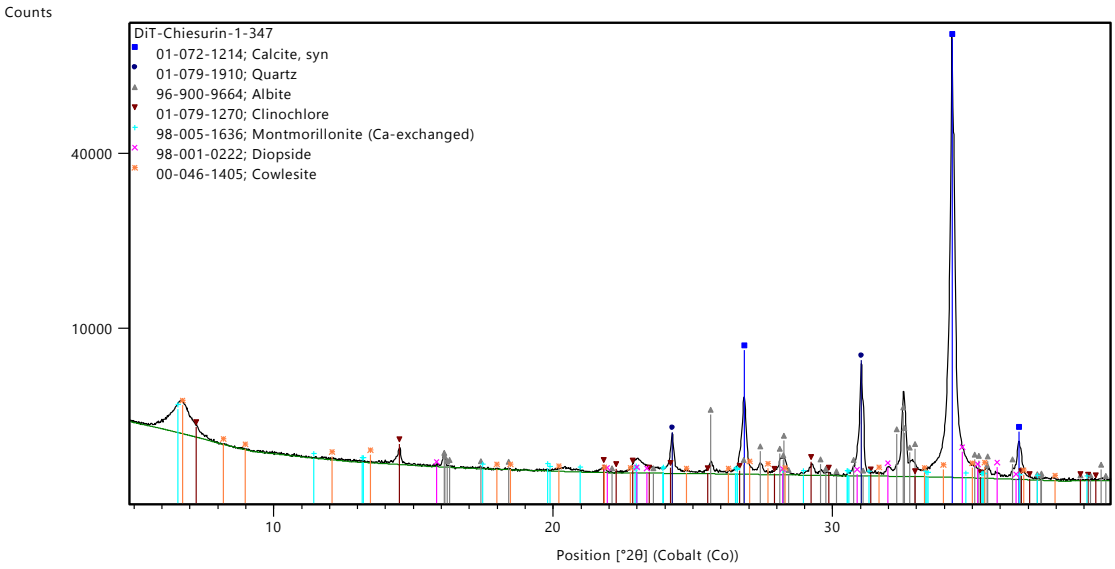

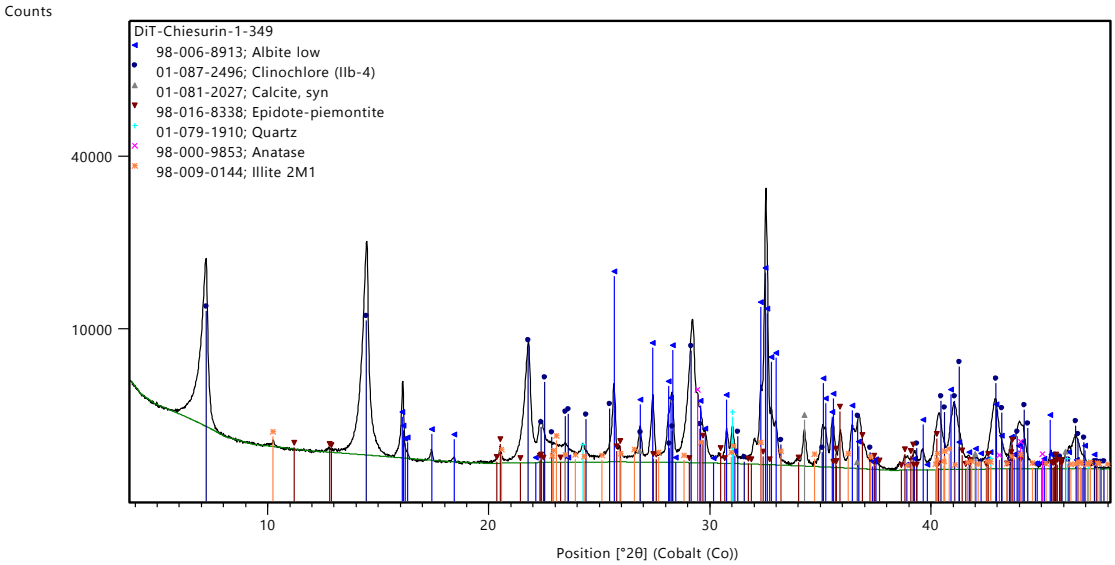
Counts
DiT-Chiesurin-1-349
98-006-8913; Albite low
01-087-2496; Clinochlore (IIb-4)
01-081-2027; Calcite, syn
98-016-8338; Epidote-piemontite
01-079-1910; Quartz
98-000-9853; Anatase
98-009-0144; Illite 2M1
40000
10000
10
20
30
40
Position [°2θ] (Cobalt (Co))

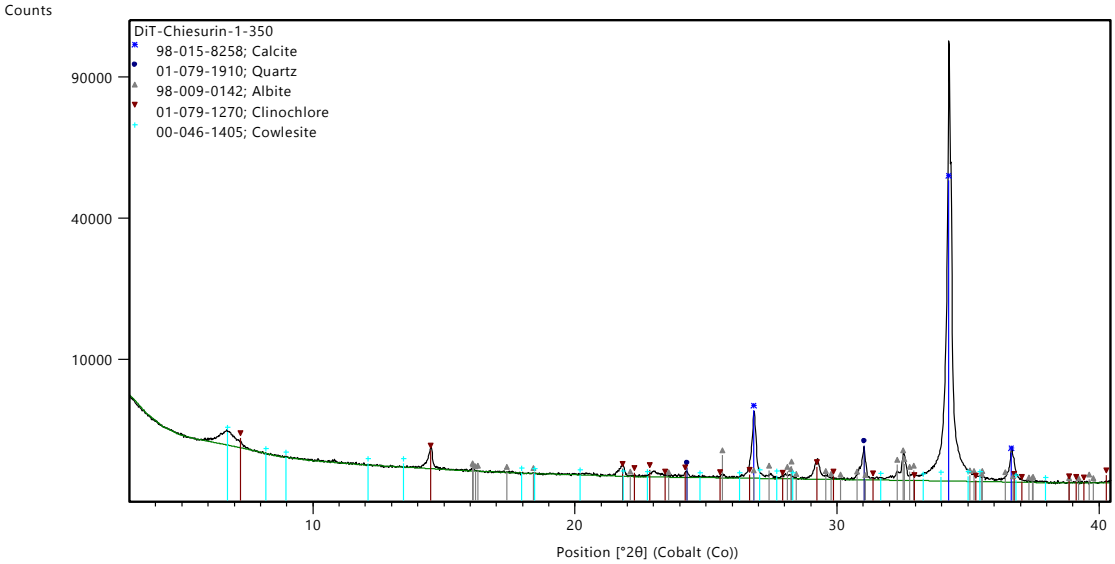
Counts
DiT-Chiesurin-1-350
98-015-8258; Calcite
01-079-1910; Quartz
98-009-0142; Albite
01-079-1270; Clinochlore
00-046-1405; Cowlesite
90000
40000
10000
10
20
30
40
Position [°2θ] (Cobalt (Co))

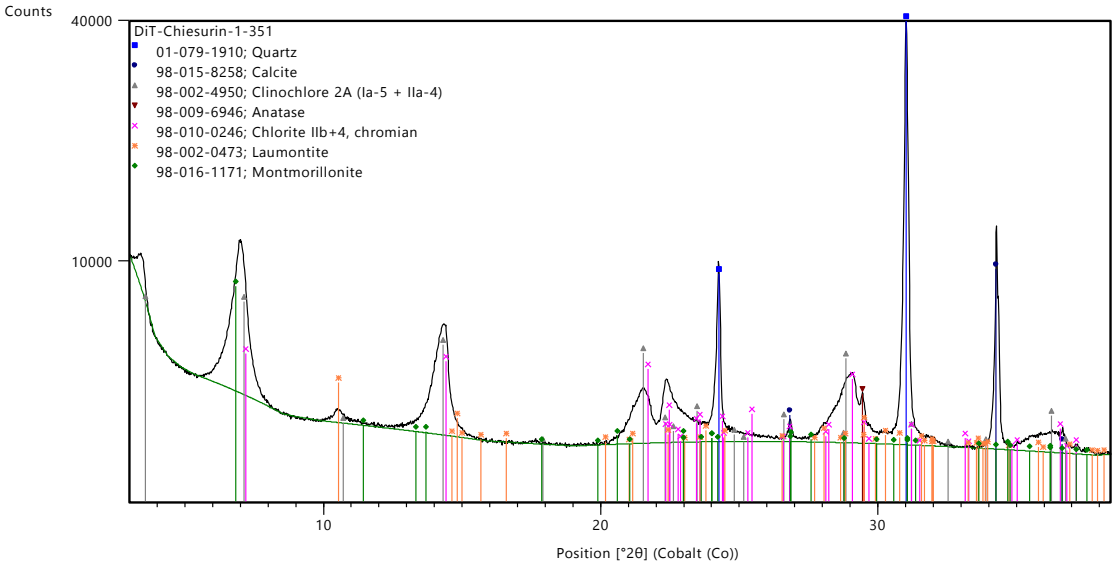
Counts
40000
10000
DiT-Chiesurin-1-351
01-079-1910; Quartz
98-015-8258; Calcite
98-002-4950; Clinochlore 2A (Ia-5 + IIa-4)
98-009-6946; Anatase
98-010-0246; Chlorite IIb+4, chromian
98-002-0473; Laumontite
98-016-1171; Montmorillonite
10
20
30
Position [°2θ] (Cobalt (Co))

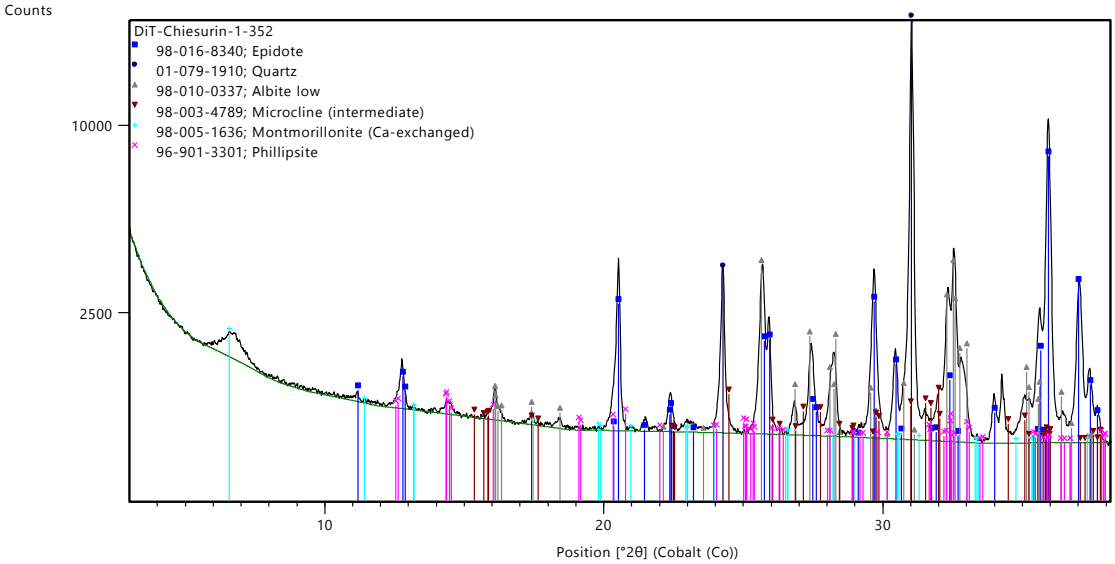
Counts
10000
2500
DiT-Chiesurin-1-352
98-016-8340; Epidote
01-079-1910; Quartz
98-010-0337; Albite low
98-003-4789; Microcline (intermediate)
98-005-1636; Montmorillonite (Ca-exchanged)
96-901-3301; Phillipsite
10
20
30
Position [°2θ] (Cobalt (Co))

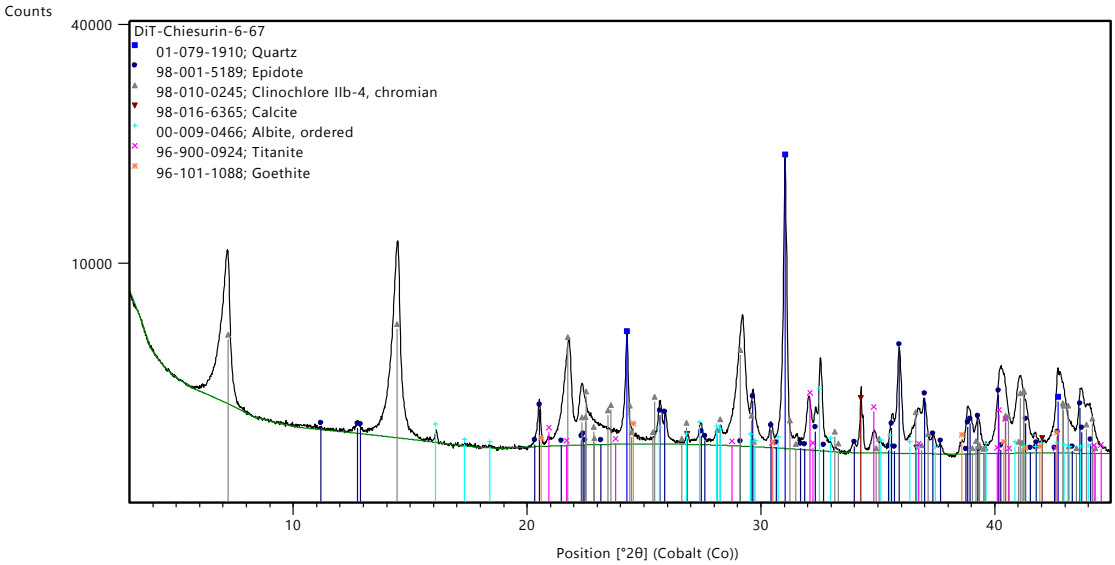
Counts
40000
10000
DiT-Chiesurin-6-67
01-079-1910; Quartz
98-001-5189; Epidote
98-010-0245; Clinochlore IIb-4, chromian
98-016-6365; Calcite
00-009-0466; Albite, ordered
96-900-0924; Titanite
96-101-1088; Goethite
10
20
30
40
Position [°2θ] (Cobalt (Co))

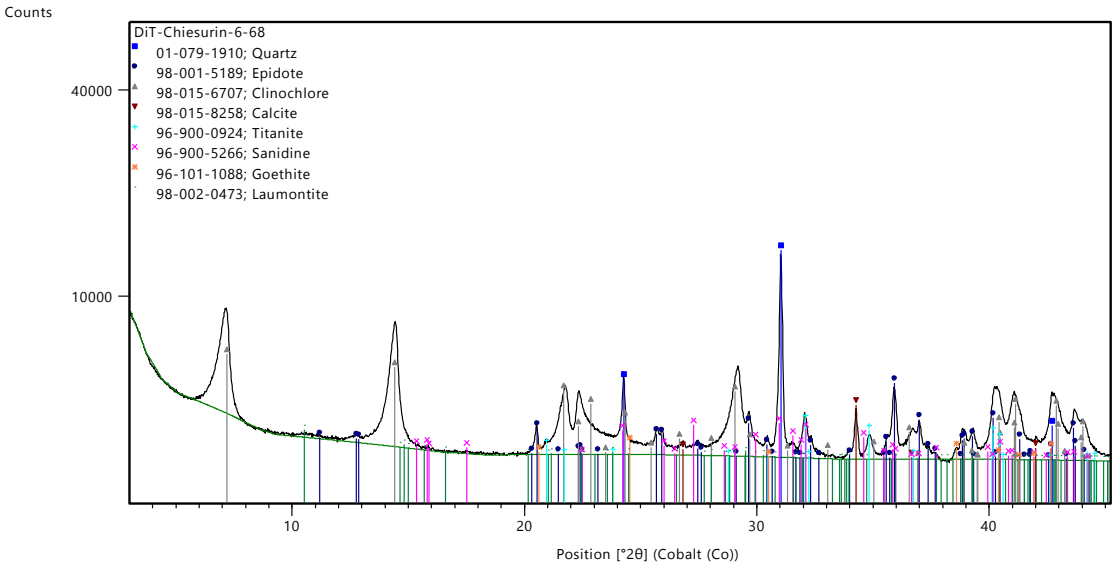
Counts
40000
10000
DiT-Chiesurin-6-68
01-079-1910; Quartz
98-001-5189; Epidote
98-015-6707; Clinochlore
98-015-8258; Calcite
96-900-0924; Titanite
96-900-5266; Sanidine
96-101-1088; Goethite
98-002-0473; Laumontite
10
20
30
40
Position [°2θ] (Cobalt (Co))

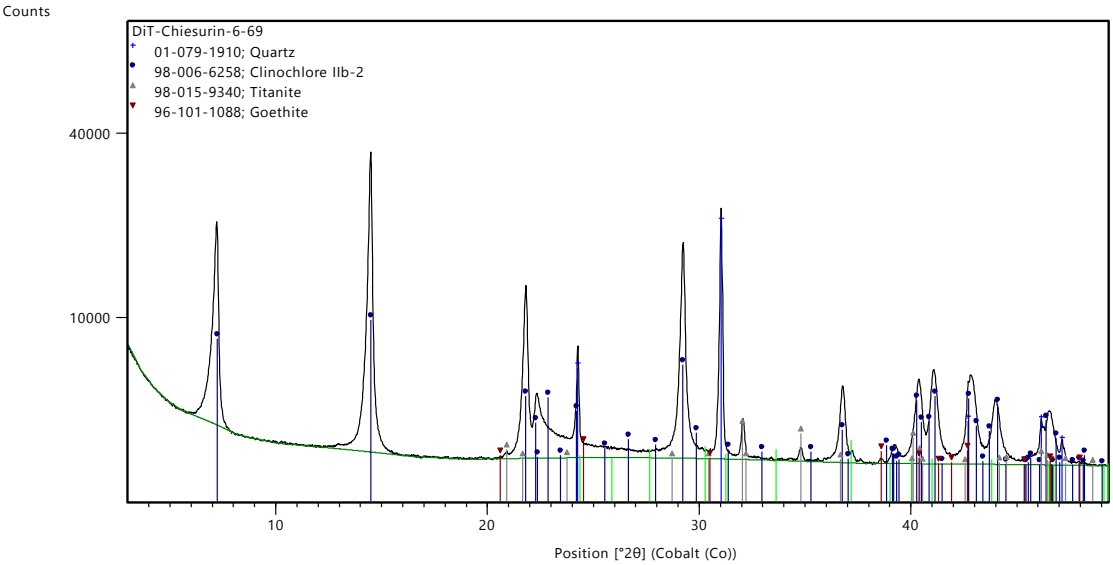
Counts
DiT-Chiesurin-6-69
01-079-1910; Quartz
98-006-6258; Clinochlore IIb-2
98-015-9340; Titanite
96-101-1088; Goethite
40000
10000
10
20
30
40
Position [°2θ] (Cobalt (Co))

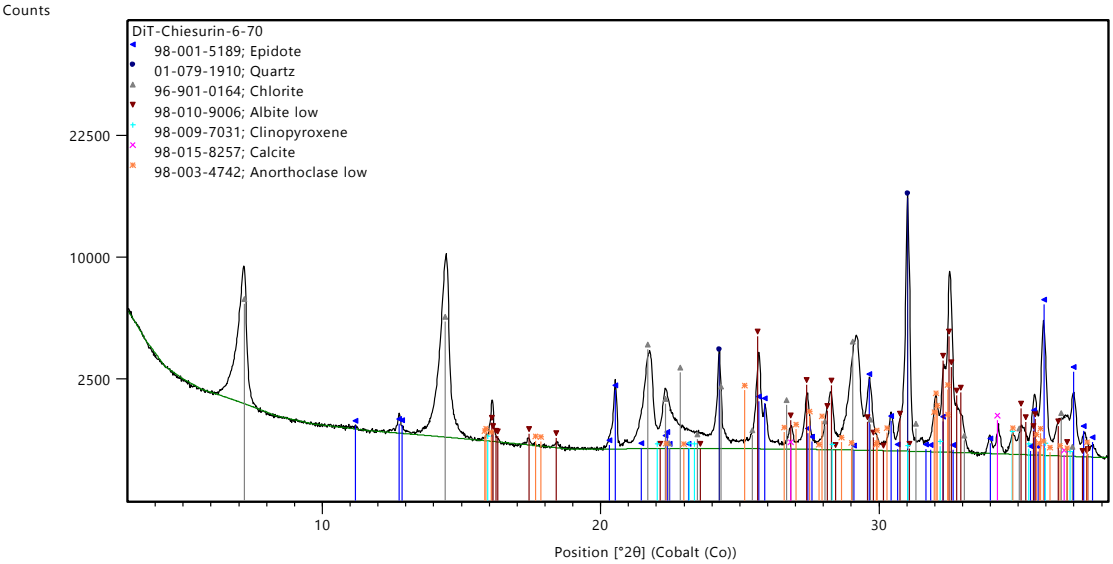
Counts
DiT-Chiesurin-6-70
98-001-5189; Epidote
01-079-1910; Quartz
96-901-0164; Chlorite
98-010-9006; Albite low
98-009-7031; Clinopyroxene
98-015-8257; Calcite
98-003-4742; Anorthoclase low
22500
10000
2500
10
20
30
Position [°2θ] (Cobalt (Co))

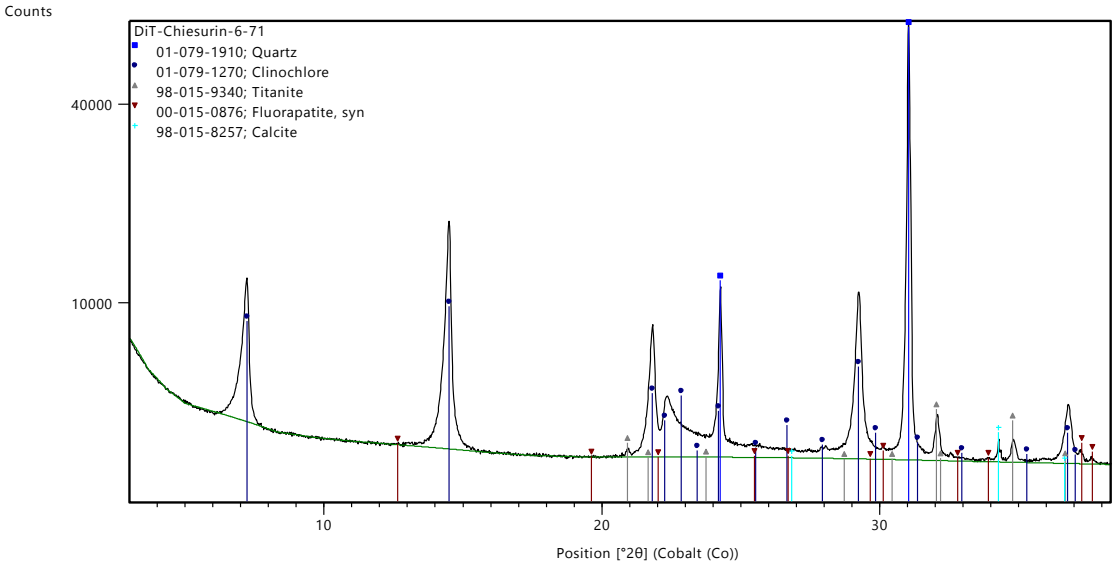
Counts
DiT-Chiesurin-6-71
01-079-1910; Quartz
01-079-1270; Clinochlore
98-015-9340; Titanite
00-015-0876; Fluorapatite, syn
98-015-8257; Calcite
40000
10000
10
20
30
Position [°2θ] (Cobalt (Co))

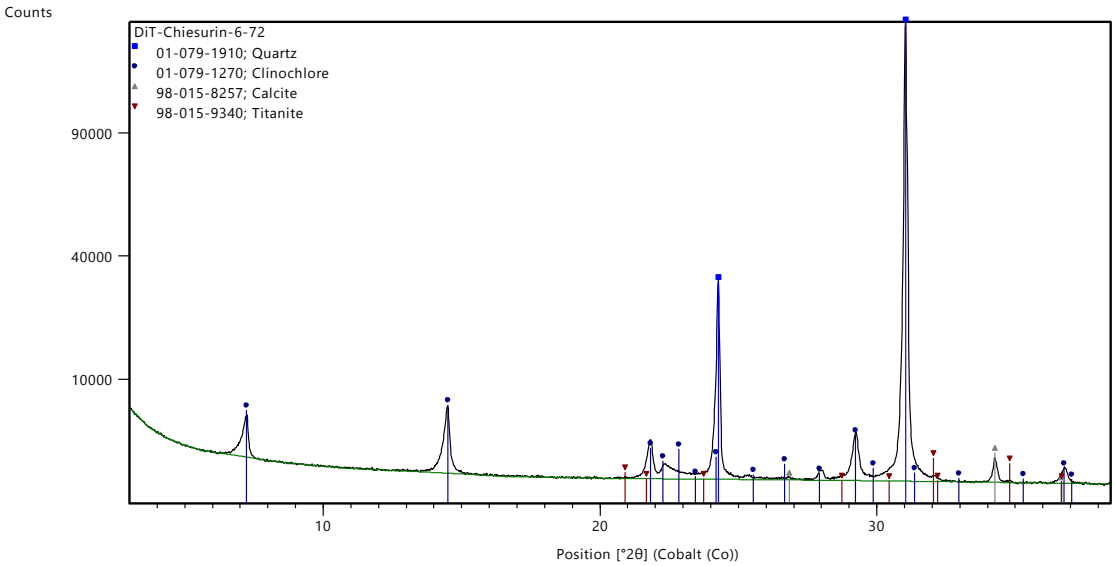
Counts
DiT-Chiesurin-6-72
01-079-1910; Quartz
01-079-1270; Clinochlore
98-015-8257; Calcite
98-015-9340; Titanite
90000
40000
10000
10
20
30
Position [°2θ] (Cobalt (Co))

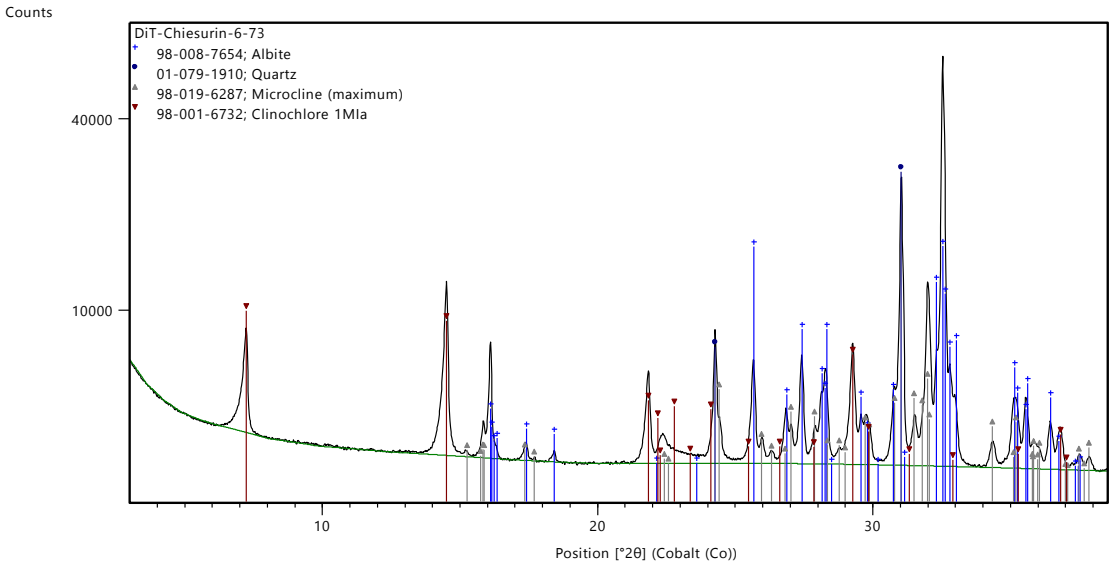
Counts
DiT-Chiesurin-6-73
98-008-7654; Albite
01-079-1910; Quartz
98-019-6287; Microcline (maximum)
98-001-6732; Clinochlore 1MIa
40000
10000
10
20
30
Position [°2θ] (Cobalt (Co))

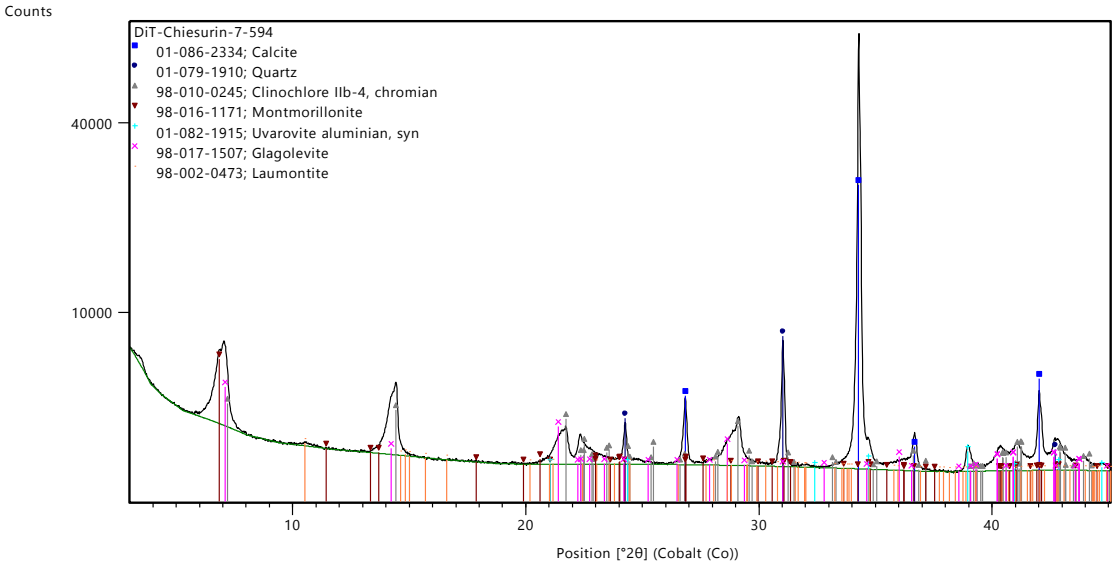
Counts
DiT-Chiesurin-7-594
01-086-2334; Calcite
01-079-1910; Quartz
98-010-0245; Clinochlore IIb-4, chromian
98-016-1171; Montmorillonite
01-082-1915; Uvarovite aluminian, syn
98-017-1507; Glagolevite
98-002-0473; Laumontite
40000
10000
10
20
30
40
Position [°2θ] (Cobalt (Co))

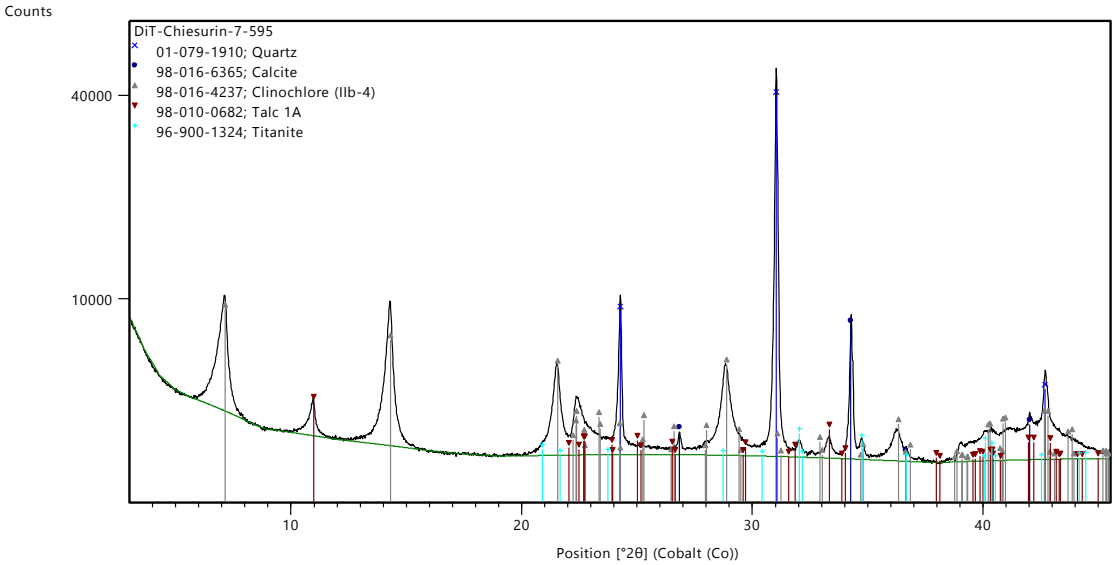
Counts
DiT-Chiesurin-7-595
01-079-1910; Quartz
98-016-6365; Calcite
98-016-4237; Clinochlore (IIb-4)
98-010-0682; Talc 1A
96-900-1324; Titanite
40000
10000
10
20
30
40
Position [°2θ] (Cobalt (Co))

Appendix 3. WDS-FEG-SEM analysis

Table of the WDS point analysis of the chlorites.

Row No	Sample	Type of Chl	Point No	SiO_2	TiO_2	Al_2O_3	V_2O_3	Cr_2O_3	FeO	MnO	NiO	MgO	CaO	K_2O	Total
1	KBH1-346	Brown Chl	Point85	27.390	0.012	18.820	0.000	0.000	21.000	0.130	0.000	17.860	0.100	0.090	85.397
2	KBH1-346	Brown Chl	Point86	27.610	0.000	19.710	0.000	0.000	21.000	0.330	0.000	18.070	0.070	0.000	86.840
3	KBH1-346	Brown Chl	Point2	28.080	0.020	20.180	0.000	0.000	20.530	0.280	0.000	17.580	0.070	0.040	86.786
4	KBH1-346	Brown Chl	Point3	28.700	0.000	19.150	0.000	0.000	22.010	0.300	0.000	18.190	0.070	0.050	88.473
5	KBH1-346	Brown Chl	Point4	28.170	0.000	19.680	0.000	0.000	22.720	0.190	0.000	18.150	0.060	0.050	89.011
6	KBH1-346	Brown Chl	Point5	27.680	0.000	18.850	0.000	0.000	21.570	0.240	0.000	17.120	0.050	0.100	85.621
7	KBH1-346	Brown Chl	Point6	27.790	0.000	19.340	0.000	0.000	21.530	0.140	0.000	18.080	0.000	0.000	86.873
8	KBH1-346	Brown Chl	Point9	28.270	0.000	19.980	0.000	0.000	20.180	0.140	0.000	18.670	0.110	0.050	87.404
9	KBH1-346	Brown Chl	Point12	27.570	0.000	20.240	0.000	0.000	21.760	0.250	0.000	18.380	0.000	0.000	88.195
10	KBH1-348	Blue Chl	Point16	29.570	0.000	16.030	0.000	0.000	20.650	0.210	0.000	18.330	0.190	0.000	84.972
11	KBH1-348	Blue Chl	Point17	28.770	0.000	15.850	0.000	0.000	21.180	0.180	0.000	18.370	0.220	0.000	84.578
12	KBH1-348	Blue Chl	Point18	27.630	0.000	16.260	0.000	0.000	22.020	0.210	0.000	16.690	0.160	0.000	82.973
13	KBH1-348	Blue Chl	Point19	28.610	0.000	16.300	0.000	0.000	21.660	0.310	0.000	16.960	0.170	0.000	84.015
14	KBH1-348	Blue Chl	Point20	29.620	0.000	15.570	0.000	0.000	19.750	0.250	0.000	17.610	0.220	0.000	83.017
15	KBH1-348	Blue Chl	Point21	28.180	0.000	16.100	0.000	0.000	22.340	0.290	0.000	15.670	0.150	0.000	82.715
16	KBH1-348	Blue Chl	Point22	28.770	0.000	15.570	0.000	0.000	21.140	0.230	0.000	17.140	0.230	0.040	83.119
17	KBH1-348	Blue Chl	Point23	28.410	0.000	15.460	0.000	0.000	21.490	0.240	0.000	15.800	0.250	0.050	81.692
18	KBH1-348	Blue Chl	Point25	27.980	0.000	16.430	0.000	0.000	21.290	0.260	0.000	17.760	0.230	0.060	84.021
19	KBH1-348	Blue Chl	Point26	28.500	0.000	16.190	0.000	0.000	21.850	0.370	0.000	17.760	0.300	0.040	86.023
20	KBH1-348	Blue Chl	Point27	30.040	0.000	17.660	0.000	0.000	21.280	0.440	0.000	19.010	0.100	0.000	88.543
21	KBH1-348	Blue Chl	Point28	29.810	0.000	14.620	0.000	0.000	19.990	0.190	0.000	18.150	0.260	0.000	83.019
22	KBH1-348	Blue Chl	Point29	28.960	0.000	16.010	0.000	0.000	20.270	0.230	0.000	17.920	0.280	0.090	83.756
23	KBH1-348	Blue Chl	Point30	30.250	0.000	16.060	0.000	0.080	20.220	0.130	0.000	18.640	0.240	0.130	85.739
24	KBH6-69	Dark Chl	Point15	29.060	0.000	18.700	0.000	0.000	16.890	0.280	0.000	20.550	0.080	0.000	85.571
25	KBH6-69	Dark Chl	Point17	28.370	0.000	18.860	0.000	0.000	16.930	0.220	0.000	20.460	0.110	0.000	84.943
26	KBH6-69	Dark Chl	Point22	28.780	0.000	18.700	0.000	0.000	17.420	0.270	0.000	20.900	0.110	0.000	86.176
27	KBH6-69	Dark Chl	Point23	28.490	0.000	18.930	0.000	0.000	17.830	0.240	0.000	20.350	0.070	0.000	85.904
28	KBH6-69	Dark Chl	Point29	28.990	0.000	19.050	0.090	0.000	17.900	0.170	0.000	20.650	0.080	0.000	86.938
29	KBH6-69	Dark Chl	Point30	29.940	0.000	21.380	0.120	0.000	13.560	0.000	0.000	21.620	0.060	0.000	86.670
30	KBH6-69	Dark Chl	Point34	29.850	0.000	21.410	0.090	0.000	13.610	0.080	0.000	21.370	0.070	0.000	86.476
31	KBH6-69	Bright Chl	Point21	27.570	0.000	18.530	0.000	0.000	22.710	0.290	0.000	17.310	0.000	0.000	86.409
32	KBH6-69	Bright Chl	Point24	27.520	0.000	18.570	0.050	0.000	22.320	0.280	0.000	17.180	0.040	0.000	85.962
33	KBH6-69	Bright Chl	Point26	27.780	0.000	18.400	0.070	0.000	20.810	0.380	0.000	18.320	0.080	0.000	85.836
34	KBH6-69	Bright Chl	Point28	27.770	0.000	18.540	0.050	0.000	22.750	0.210	0.000	18.600	0.020	0.000	87.928
35	KBH6-69	Bright Chl	Point31	27.920	0.000	18.700	0.080	0.000	21.280	0.220	0.000	18.850	0.050	0.000	87.080
36	KBH6-69	Bright Chl	Point32	27.710	0.000	18.660	0.000	0.000	23.100	0.320	0.000	17.890	0.020	0.000	87.703
37	KBH6-69	Bright Chl	Point33	26.820	0.000	18.610	0.070	0.000	22.090	0.270	0.000	18.020	0.060	0.000	85.960
38	KBH6-71	Brown Chl	Point42	29.230	0.000	18.810	0.000	0.000	21.110	0.190	0.000	18.400	0.000	0.000	87.736
39	KBH6-71	Brown Chl	Point43	27.790	0.000	18.500	0.000	0.000	21.070	0.300	0.000	16.750	0.090	0.000	84.500
40	KBH6-71	Brown Chl	Point44	26.540	0.000	18.090	0.000	0.000	21.870	0.350	0.000	17.400	0.060	0.000	84.303
41	KBH6-71	Brown Chl	Point45	27.840	0.000	17.910	0.000	0.000	18.860	0.230	0.000	19.110	0.070	0.000	84.011
42	KBH6-71	Brown Chl	Point46	28.970	0.000	18.030	0.000	0.000	21.110	0.340	0.000	18.440	0.050	0.000	86.941
43	KBH6-71	Brown Chl	Point47	29.940	0.000	18.900	0.000	0.000	19.050	0.250	0.000	19.330	0.070	0.030	87.567
44	KBH6-71	Brown Chl	Point48	26.340	0.000	19.210	0.000	0.000	22.500	0.390	0.000	16.910	0.040	0.000	85.395
45	KBH6-71	Green Chl	Point31	28.650	0.000	19.880	0.000	0.000	15.940	0.070	0.000	20.600	0.000	0.000	85.219
46	KBH6-71	Green Chl	Point32	30.670	0.000	20.880	0.000	0.000	15.030	0.160	0.000	22.330	0.060	0.000	89.214
47	KBH6-71	Green Chl	Point33	27.550	0.000	19.570	0.000	0.000	16.010	0.110	0.000	19.880	0.000	0.000	83.219
48	KBH6-71	Green Chl	Point34	29.040	0.000	19.220	0.000	0.000	16.850	0.100	0.000	20.760	0.060	0.000	86.021
49	KBH6-71	Green Chl	Point35	29.520	0.000	19.770	0.000	0.000	16.500	0.040	0.000	21.110	0.050	0.000	86.979
50	KBH6-71	Green Chl	Point36	29.250	0.000	19.410	0.000	0.000	16.200	0.060	0.000	20.360	0.040	0.000	85.298
51	KBH6-71	Green Chl	Point37	27.870	0.000	19.520	0.000	0.000	17.420	0.090	0.000	19.920	0.050	0.000	84.870
52	KBH6-71	Green Chl	Point38	28.580	0.000	19.740	0.000	0.000	15.460	0.220	0.000	19.640	0.000	0.000	83.637
53	KBH6-71	Green Chl	Point39	28.720	0.000	19.710	0.000	0.000	15.430	0.070	0.000	20.750	0.000	0.000	84.686
54	KBH7-595	Fibrous Chl	Point52	33.100	0.000	14.010	0.000	0.100	14.570	0.250	0.000	24.180	0.300	0.000	86.511
55	KBH7-595	Fibrous Chl	Point53	31.770	0.000	14.210	0.000	0.090	14.870	0.150	0.150	23.720	0.310	0.040	85.299
56	KBH7-595	Fibrous Chl	Point54	31.390	0.000	14.050	0.000	0.110	15.050	0.120	0.000	24.750	0.260	0.000	85.718
57	KBH7-595	Fibrous Chl	Point55	32.250	0.000	14.830	0.000	0.000	14.590	0.190	0.000	24.880	0.200	0.000	86.944
58	KBH7-595	Fibrous Chl	Point60	30.240	0.000	14.340	0.000	0.120	14.740	0.310	0.200	23.470	0.210	0.000	83.629
59	KBH7-595	Fibrous Chl	Point63	30.600	0.000	15.420	0.000	0.100	14.040	0.190	0.190	25.130	0.240	0.000	85.898
60	KBH7-595	Fibrous Chl	Point73	33.440	0.000	13.170	0.000	0.120	14.790	0.210	0.000	22.570	0.300	0.000	84.591
61	KBH7-595	Fibrous Chl	Point74	35.210	0.000	13.940	0.000	0.110	15.100	0.170	0.140	23.310	0.290	0.000	88.265
62	KBH7-595	Fibrous Chl	Point75	37.160	0.000	14.090	0.000	0.000	14.520	0.070	0.160	22.810	0.920	0.040	89.778
63	KBH7-595	Fibrous Chl	Point76	34.750	0.000	13.820	0.000	0.070	14.580	0.210	0.180	23.310	0.200	0.040	87.169
64	KBH7-595	Fibrous Chl	Point77	34.180	0.000	13.820	0.000	0.070	14.500	0.160	0.000	23.140	0.250	0.030	86.158
65	KBH7-595	Fibrous Chl	Point78	34.180	0.000	13.370	0.000	0.090	14.820	0.210	0.000	22.760	0.200	0.000	85.621
66	KBH7-595	Fibrous Chl	Point79	34.880	0.000	13.720	0.000	0.090	14.780	0.080	0.000	23.770	0.160	0.000	87.484
67	KBH7-595	Rayed Chl	Point83	35.330	0.000	11.360	0.000	0.000	12.630	0.080	0.000	25.420	0.090	0.000	84.911
68	KBH7-595	Rayed Chl	Point37	34.710	0.000	11.600	0.000	0.000	13.150	0.150	0.000	26.240	0.060	0.000	85.909
69	KBH7-595	Rayed Chl	Point38	34.610	0.000	11.450	0.000	0.000	12.810	0.000	0.000	25.800	0.050	0.000	84.714
70	KBH7-595	Rayed Chl	Point39	34.900	0.000	11.640	0.000	0.000	12.580	0.130	0.000	26.290	0.060	0.000	85.603
71	KBH7-595	Rayed Chl	Point40	34.610	0.000	11.460	0.000	0.000	12.440	0.080	0.000	26.050	0.100	0.000	84.736
72	KBH7-595	Rayed Chl	Point41	34.450	0.000	11.080	0.000	0.000	12.670	0.120	0.000	26.140	0.060	0.000	84.515
73	KBH7-595	Rayed Chl	Point42	34.730	0.000	11.320	0.000	0.000	12.880	0.060	0.140	26.530	0.080	0.000	85.746
74	KBH7-595	Rayed Chl	Point43	33.600	0.000	12.280	0.000	0.000	13.470	0.270	0.160	25.710	0.120	0.040	85.656
75	KBH7-595	Rayed Chl	Point44	34.720	0.000	11.640	0.000	0.000	13.100	0.140	0.160	26.110	0.080	0.000	85.938
76	KBH7-595	Rayed Chl	Point45	34.410	0.000	11.620	0.000	0.000	13.400	0.100	0.000	26.700	0.070	0.000	86.289
77	KBH7-595	Rayed Chl	Point46	34.620	0.000	12.110	0.000	0.000	13.010	0.090	0.130	25.770	0.130	0.000	85.869
78	KBH7-595	Rayed Chl	Point48	34.820	0.000	11.150	0.000	0.000	12.500	0.130	0.000	26.600	0.070	0.000	85.259
79	KBH7-595	Rayed Chl	Point49	35.010	0.000	12.080	0.000	0.000	12.920	0.080	0.000	26.020	0.150	0.000	86.254